6-9-2021 12:30 PM

3D Printed Polypyrrole Scaffolds for pH Dependent Drug Delivery with Applications in Bone Regeneration

Matthew T. Lawrence, *The University of Western Ontario*

Supervisor: Price, Aaron D., *The University of Western Ontario*
Co-Supervisor: Séguin, Cheryle A., *The University of Western Ontario*
A thesis submitted in partial fulfillment of the requirements for the Master of Engineering Science degree in Biomedical Engineering

Abstract

Areas of large bone loss are typically healed using autologous bone grafts, seen as the gold standard of care. These materials have a complication rate of 10–40% during harvesting and are limited by the quantity available; therefore the use of 3D printed polymer scaffolds as bone graft alternatives are proposed. Polypyrrole (PPy) is a biocompatible electroactive polymer that has metal-like electrical properties that can be harnessed to hold and release charged drug molecules, triggered by a change in pH. pH fluctuations are seen inside the human body in areas of bone regrowth, which would act as the triggering mechanism for drug release from PPy. PPy nanoparticles were incorporated into hydrogel resins, capable of being 3D printed using stereolithography techniques using riboflavin as a natural photoinitiator. Polymers were tested for drug delivery capabilities, cell adhesion, and biocompatibility to ensure proper function. These composite polymers were successful as a potential material for synthetic bone grafts.

Keywords: 3D printing, smart polymers, polypyrrole, drug delivery, bone regeneration.

Summary for Lay Audience

3D Printing is revolutionizing the manufacturing of medical devices, allowing the production of patient-customized devices with unique shapes. Bioprinting refers to the application of 3D printing alongside the incorporation of cells, growth factors, drug molecules, and biologics to create materials that mimic real tissues. One common bioprinting material is hydrogels, classified as polymers that have a high affinity for water. Hydrogels have been shown they are capable of supporting cell growth but are not perfect and can have improved functionality by pairing them with a second polymer. Polypyrrole was chosen as a copolymer because of its electrical properties as a conjugated polymer, meaning it offers metal-like conductivity in a polymer. These properties give polypyrrole the ability to store and release drug molecules, triggered by surrounding pH changes. Interestingly, there are pH changes seen naturally in areas of bone regrowth or regeneration due to the bone healing cycle. Using polypyrrole in areas on bone regeneration could act as the triggering method for drug release from 3D printed scaffolds. In this study, we used 3D printing to create a hydrogel-polypyrrole scaffold capable of pH-triggered drug delivery while supporting cell growth. The scaffold was tested for drug delivery capabilities, cell adhesion, and biocompatibility to ensure proper function inside the human body. These studies show the success of a 3D printed biocompatible hydrogel-polypyrrole scaffold and could be further investigated as an alternative to bone grafts.

So often in life, things that you regard as an impediment turn out to be great, good fortune.

–Justice Ruth Bader Ginsburg

Dedication

Dedicated to all, as science is meant to be shared.

Acknowledgements

Financial support for my studies was generously provided by NSERC Canada, the Government of Ontario: Ministry of Research and Innovation, the Western Bone and Joint Institute, and Western University.

Thank you to the members of my Advisory Committee, Drs. Elizabeth Gillies and Jeffrey Dixon, for their valuable insight and guidance throughout my project.

Special thanks to my thesis supervisors Drs. Aaron Price and Cheryle Séguin. To Dr. Price for his unwavering support in my research abilities and trusting nature that allowed me the freedom to follow my research passions. To Dr. Séguin for her patience, thoughtful feedback, and demonstrating the constant joy of problem-solving in research that has always made me feel hopeful when stepping into the lab. Invaluable guidance and advice from both supervisors allowed me to bridge my engineering and biology research interests into one thoughtful project.

Thank you to all my colleagues that shaped my Graduate School experience. Everyone in the Organic Mechatronics and Smart Materials Laboratory has had an impact on this project. Special thanks to Ben Holness who offered countless hours of assistance and camaraderie over the past two years that were vital to my success in all aspects of Graduate School. Thank you to all the members of the Séguin lab who shared their wisdom and offered support during my experiments, especially Courtney Brooks who answered all my questions and offered continuous guidance throughout my project.

Thank you to my friends and family, especially Georgi Bailey, Alejandra Calva, Hailey Holmes, Meghan Vissers and Elizabeth Blokker. Finally, thank you to my parents; your encouragement in my journey through Graduate School has been vital to my success and I am eternally grateful.

Equity, Diversity & Inclusion (EDI)

As a commitment to research be accessible to everyone, I have chosen to include a section on Equity, Diversity, and Inclusion (EDI) and my commitments to EDI in research. EDI in research should work to remove barriers to success for equity-deserving groups, which include but are not limited to women, Indigenous peoples (First Nations, Inuit, and Métis), members of racialized groups, persons with disabilities, and members of the LGBTQ2S+ community. This responsibility falls upon students, trainees, postdoctoral fellows, collaborators, and principal investigators to instigate and sustain change. I, as a student, have worked to increase the EDI of my faculty, and Western as a whole for future student success. As my research does not focus on any population, demographic or health data, the EDI commitments that I have made include personal learning and accountability. During my time as a graduate student I have completed sessions such as the BrainsCAN EDI in Research training webinar, KAIROS Blanket Exercise, and Indigenous Land Acknowledgement workshop, all of which have increased my awareness of other's perspectives outside my own lived experiences. From these sessions, I have learned how the research community that I am a part of and the research I produce needs to serve Canada's diverse population. My personal accountability motivated me to advocate for increased EDI training within the Biomedical Engineering department for such items as yearly EDI training modules, grant writing sessions covering EDI, and confidential reporting tools for students. I currently sit as Co-Chair of the Schulich Council on Reforming Equity, Diversity and Inclusion for Trainees (CREDIT) which serves to work alongside the Schulich School of Medicine & Dentistry in regards to equity for trainees. These leadership roles and learning opportunities highlighted the need to increase my advocacy for all underrepresented groups in academia. I will take these values into future endeavours as I work to create equitable spaces for all.

Contents

List of Tables

List of Figures

List of Acronyms and Symbols

Acronyms

AM	additive manufacturing
α-mem	Minimum Essential Medium α
ANOVA	analysis of variance
BMP	bone morphogenic protein
BMP	bone morphogenic proteins
BSA	bovine serum albumin
CAD	computer-assisted design
CP	conjugated polymer
DPBS	Dulbecco's phosphate-buffered saline
ECM	extra-cellular matrix
EDI	equity diversity and inclusion
FBS	fetal bovine serum
FL	fluorescein
H_2O_2	hydrogen peroxide
HCl	hydrochloric acid
ICP	intrinsically conducting polymers
ISO	International Organization for Standardization
OMASML	Organic Mechatronics and Smart Materials Laboratory
PBS	phosphate-buffered saline

PEGDA	polyethylene glycol diacrylate
PEG	polyethylene glycol
PFA	paraformaldehyde
PPy	polypyrrole
SDS	sodium dodecyl sulfate
SEM	scanning electron microscopy
SE	Standard Error
TEA	triethanolamine
TE	tissue engineering
UV	ultra-violet

Greek symbols

χ	Flory-Huggin's interaction parameter
ρ	density
σ	conductivity

Latin symbols

$\bar{v}$	specific volume
I	current
M_C	average molecular weight between crosslinks
M_N	average molecular weight
m	mass
Q_m	mass swollen ratio
t	thickness
V_1	molar volume
$v_{2,r}$	polymer fraction, relaxed
$v_{2,s}$	polymer fraction, swollen
V	voltage

Chapter 1

Introduction

The 3D printing of polymers has revolutionized the rapid production of customized objects with complex microstructures. Applications of 3D printing are vast, but one of the most promising areas of growth is the medical device industry. 3D printing allows the creation of patient customized devices with a wide variety of properties, depending heavily on the material chosen. Conjugated polymers (CP) have been investigated for use in 3D printing applications due to their electrical properties created through a backbone of alternating single- and double-bonds. This conjugated bonding structure allows electrical conductivity, not typically seen in conventional polymers. Combining electrically conductive polymers with the benefits of 3D printing would be optimal for the creation of novel biomedical devices.

Polypyrrole (PPy) is an organic CP that has specific properties that can be modulated due to physical, electrical, and chemical stimuli. Given its electrical properties, PPy has been utilized in medical research in neural devices, bone regeneration, and tissue engineering (Vijayavenkataraman et al., 2019; Sajesh et al., 2013; Ateh et al., 2006). One of the most promising applications has been as a drug delivery and biosensing material (Geetha et al., 2006). Previous studies have used PPy to store dopant molecules based off redox reactions caused by voltage changes along the polymer

backbone (Hosseini-Nassab et al., 2016). PPy also has the capability to respond to changes in localized pH to release stored dopant molecules (Samanta et al., 2015). These pH changes occur naturally inside the human body in areas of infections, chronic wounds, and bone healing (Schneider et al., 2007; Chakkalakal et al., 1994). Harnessing this pH change would allow PPy to "switch" on in areas of bone regeneration, triggering the delivery of molecules inside the human body. Concurrently, research into bone graft alternatives is increasing due to the relatively high complication rate during graft harvest and limited supply of real bone tissue (Zeng et al., 2018). Given this previous research, PPy would be an optimal candidate for synthetic bone grafts.

So far, few studies have combined the useful properties of PPy with the benefits of bio-printing for bone regeneration applications. The poor processability of PPy has limited the use of novel creation methods, thus curbing the biological applications that this smart polymer can be used for. Although drug delivery with PPy has been researched previously, these studies focused on the electrical stimulation of PPy, a stimuli not normally seen within the human body (Hosseini-Nassab et al., 2016; Svirskis et al., 2010; Wadhwa et al., 2006). Research on pH-dependent drug release of PPy is sparse and requires further work to elucidate its full capability as a drug delivery vehicle.

1.1 Objectives

This thesis work aims to investigate the 3D printing of drug-doped PPy/hydrogel scaffolds for applications in bone regeneration. To achieve this goal, the following research objectives are purposed:

- *Development of a biocompatible PPy resin.* The first objective is to develop a biocompatible resin with incorporated drug-doped PPy nanoparticles (NP) that is capable of being printed using a novel stereolithography 3D printer in the Organic Mechatronics and Smart Materials Laboratory (OMASML). Characterization of the

printing parameters will be performed to offer optimized print resolution, allowing the creation of complex micro-featured scaffolds for biomedical applications.

- *Investigate PPy NP drug release conditions and characteristics.* The second objective is to elucidate PPy drug entrapment and release properties from this drug delivery vehicle, focusing on biologically relevant pH values. PPy polymer release data will be collected over an extended period to examine the timeline of molecule release.

- *Test the cytotoxicity and cell-interactions of the PPy/PEGDA resin for use as an implant material.* The final objective aims to demonstrate that osteoblast cells have minimal cytotoxicity when exposed to this polymer as part of an initial safety assessment. The second part of the biocompatibility tests include cell adhesion tests to ensure viability inside the human body to act as a scaffold for rapid bone regeneration.

1.2 Major contributions

This thesis communicates the following contributions to the scientific community:

- *Novel PPy NP/Hydrogel photoactive resin.* The first study of PPy NPs encapsulated in poly(ethylene) glycol diacrylate (PEGDA) created using additive manufacturing methods. The two-step creation method combines the advantageous properties of PPy NPs into a photoactive resin blend, capable of being 3D printed. The relationships between print parameters, print resolution and PPy concentration were investigated. This research led to the creation of complex, high-resolution PPy/PEGDA scaffolds with flexible microarchitectures for bone regeneration applications.

- *Polypyrrole drug delivery of biologically relevant dopant molecules at physiological*

pH values. Dopant entrapment and release characteristics from PPy NPs in PEGDA hydrogel scaffolds were successfully tested over a range of physiological pH values. The release capabilities of the PPy/PEGDA scaffolds have shown the pH-triggered switching parameters, optimal for *in-vivo* drug delivery applications.

- *Biocompatibility and cell adhesion testing of the PPy/PEGDA formula.* Testing of the novel PPy/PEGDA resin with MC3E3-E1 pre-osteoblast cells allowed both the cytotoxicity and cell adhesion interactions to be investigated. There were no cytotoxic effects from the PPy/PEGDA scaffold leachate over a 14 d period. Additionally, the addition of PPy NPs improved the PEGDA cell adhesion. Given these biological results, it has been shown that this novel resin blend and creation methodology offers a flexible biomaterial for future studies.

1.3 Organization of the thesis

The following Chapter 2: *Background* outlines influential knowledge that has proceeded this thesis, including relevant topics on bone physiology, hydrogels, CPs and additive manufacturing. In accordance with the previously mentioned objectives, this thesis is organized as follows: Chapter 3: *PPy/PEGDA Composite Resin Creation* explores the creation and characterization of a PPy/PEGDA resin, using a natural photoinitiator, riboflavin. Chapter 4: *PPy/PEGDA Composite Resin Application*, explores the applications of the previously described resins, including the 3D print resolution and drug delivery capability in response to pH stimuli. Specifically outlining the dopant entrapment and release characteristics, showing the vast biomedical applications with the use of PPy. Chapter 5: *Resin Biocompatibility Testing* outlines the biological studies used to ensure that the printed resin is capable of being used as a biomaterial. This is shown through cytotoxicity and cell adhesion studies that explore the cell response to this PPy/PEGDA polymer. Finally, Chapter 6 *Concluding remarks* summarizes the overall

conclusions of this work, restating the major contributions to the scientific community, and provides recommendations for exciting future work in the biomedical field for PPy.

List of references

Ateh, D., Navsaria, H. and Vadgama, P. (2006), 'Polypyrrole-based conducting polymers and interactions with biological tissues', *Journal of The Royal Society Interface* **3**(11), 741–752.

Chakkalakal, D. A., Mashoof, A. A., Novak, J., Strates, B. S. and McGuire, M. H. (1994), 'Mineralization and ph relationships in healing skeletal defects grafted with demineralized bone matrix', *Journal of Biomedical Materials Research* **28**(12), 1439–1443.

Geetha, S., Rao, C., Vijayan, M. and Trivedi, D. (2006), 'Biosensing and drug delivery by polypyrrole', *Analytica Chimica Acta* **568**(1-2), 119–125.

Hosseini-Nassab, N., Samanta, D., Abdolazimi, Y., Annes, J. P. and Zare, R. N. (2016), 'Electrically controlled release of insulin using polypyrrole nanoparticles.', *Nanoscale* **9**(1), 143–149.

Sajesh, K., Jayakumar, R., Nair, S. V. and Chennazhi, K. (2013), 'Biocompatible conducting chitosan/polypyrrole–alginate composite scaffold for bone tissue engineering', *International Journal of Biological Macromolecules* **62**, 465 – 471.

Samanta, D., Meiser, J. L. and Zare, R. N. (2015), 'Polypyrrole nanoparticles for tunable, pH-sensitive and sustained drug release', *Nanoscale* **7**(21), 9497–9504.

Schneider, L. A., Korber, A., Grabbe, S. and Dissemond, J. (2007), 'Influence of pH on wound-healing: a new perspective for wound-therapy?', *Archives of Dermatological Research* **298**(9), 413–420.

Svirskis, D., Travas-Sejdic, J., Rodgers, A. and Garg, S. (2010), 'Electrochemically controlled drug delivery based on intrinsically conducting polymers', *Journal of Controlled Release* **146**(1), 6–15.

Vijayavenkataraman, S., Kannan, S., Cao, T., Fuh, J. Y. H., Sriram, G. and Lu, W. F. (2019), '3d-printed pcl/ppy conductive scaffolds as three-dimensional porous nerve guide conduits (ngcs) for peripheral nerve injury repair', *Frontiers in Bioengineering and Biotechnology* **7**, 266.

Wadhwa, R., Lagenaur, C. F. and Cui, X. T. (2006), 'Electrochemically controlled release of dexamethasone from conducting polymer polypyrrole coated electrode', *Journal of Controlled Release* **110**(3), 531–541.

Zeng, J.-H., Liu, S.-W., Xiong, L., Qiu, P., Ding, L.-H., Xiong, S.-L., Li, J.-T., Liao, X.-G. and Tang, Z.-M. (2018), 'Scaffolds for the repair of bone defects in clinical studies: a systematic review', *Journal of Orthopaedic Surgery and Research* **13**(1).

Chapter 2

Background

As outlined in Chapter 1: *Introduction*, this project aims to use additive manufacturing techniques to create a PPy/PEGDA hydrogel scaffold, capable of drug delivery inside the human body in areas of bone regeneration. This chapter outlines the necessary information to understand this thesis. An introduction into the bone structure and bone grafts is outlined and provides background into the over-arching application for this work. Polymers, including both hydrogels and CPs, provides the groundwork for understanding the biomedical applications of these materials. The current applications of PPy in the medical field as a biomaterial are outlined, focusing on osteogenic studies. Finally, research in bioprinting of hydrogels and PPy is presented and defines the current problems of each type of material. The background chapter connects the topics of bone, polymers, and additive manufacturing and how they relate to the following work.

2.1 Bone

2.1.1 Physiological Bone

Bone is one of the most interesting organs in the human body, stiff yet porous, rigid yet constantly being remodelled. Bones are key in our day-to-day lives, necessary

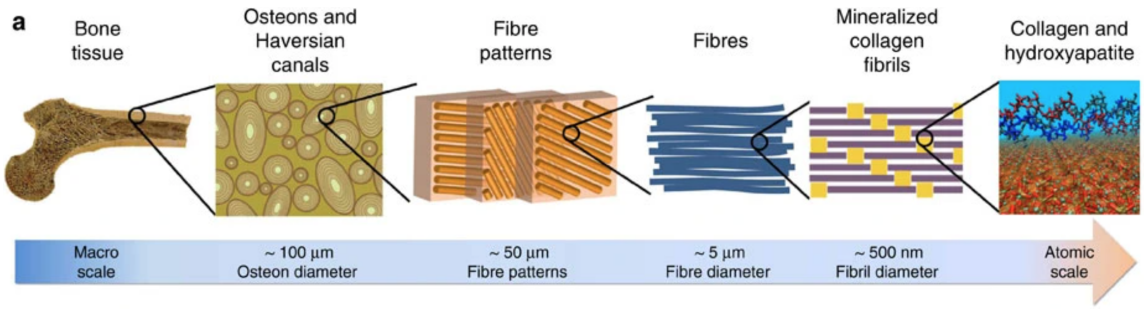

Figure 2.1: Schematic of bone architecture moving from the macro to the atomic scale, highlighting the complex nature of bone tissue (© Nair et al. (2013), included with permission).

for mobility, protecting vital organs, and providing calcium and phosphate homeostasis (Wang and Yeung, 2017). Bone has two distinct types: cortical and cancellous. Cortical bone, otherwise known as compact bone, is the hard outer shell of bones that provides rigidity and has a very low porosity value of 3–12% (Karageorgiou and Kaplan, 2005). Cancellous bone, also know as trabecular and spongy, is the inner portion of the bone that is has a porosity between 50–90% (Karageorgiou and Kaplan, 2005). Bone is highly vascularized with blood vessels, referred to as Haversian canals, with rings of calcified bone encircling them called osteons, seen in Figure 2.1. The porosity of trabecular bone allows for the delivery of cells and vascularization that are vital to bone growth. It has been seen that the minimum pore diameter for bone vascularization is 100 μm (Karageorgiou and Kaplan, 2005). The porosity values of bone impact the electrical conductivity; cortical bone has a conductivity of 9.1 mS/m compared to bone marrow region with a conductivity of 230 mS/m (Balmer et al., 2018).

Bone is comprised of extra-cellular matrix (ECM) and three main types of cells: osteoblasts, osteoclasts, and osteocytes. The ECM contains both an inorganic matrix in the form of hydroxyapatite, which provides compressive strength, and an organic matrix component made up of 90% type 1 collagen and 10% non-collagenous regulatory proteins (Clarke, 2008). Osteoblasts are responsible for the creation of bone, they

synthesize new layers of ECM over the surface of the bone, encasing osteocytes into the bone. Osteocytes are osteoblasts that have been fully surrounded by bone and facilitate communication through cell signalling. Osteoclasts resorb bone through the excretion of acidic H+ ions and cathepsin K enzyme, which break down the mineral and protein components of bone (Clarke, 2008). These cells cause the localized pH environment to fluctuate around areas of bone regeneration. The body has a natural buffer system that maintains a blood pH of 7.4, anything less is referred to as acidosis and anything above, alkalosis (Schneider et al., 2007). Chakkalakal et al. (1994) used a rat model to show the acid/base switching seen in areas of large skeletal defects. In the first week after injury, there was an acidic environment around the tissue, moving towards an alkaline environment in the following three weeks, seen in Figure 2.2. These changes in pH are due to which cells are prominent at each time point. The acidic environment is key to osteoclast bone resorption of older ECM that may be damaged. Osteoclast activity peaks at pH 7 (Galow et al., 2017). Conversely, osteoblasts have been shown to have optimal activity when the pH is between $8.0 - 8.4$ (Galow et al., 2017). The outlined pH change is an important aspect of the chemical activity of bone grafts and it can be harnessed as a natural stimulus to facilitate drug delivery from synthetic polymers.

2.1.2 Bone Grafts

Bone grafts are often used in areas of large bone loss, commonly seen in dentistry (Kumar et al., 2013). With little material left to support cell growth, there is room for bacterial proliferation and slow bone healing. Trauma, infection, surgery or genetic conditions can all cause bone defects, leading to bone being the second most common type of tissue transplant, after blood (Kumar et al., 2013; Wang and Yeung, 2017). There is a large area of research into the creation and testing of natural, artificial or synthetic bone grafts to accommodate the tremendous demand. The goal of bone grafts is to eliminate dead space and reduce the risk of infection post-operatively (Kumar et al., 2013). Laurencin

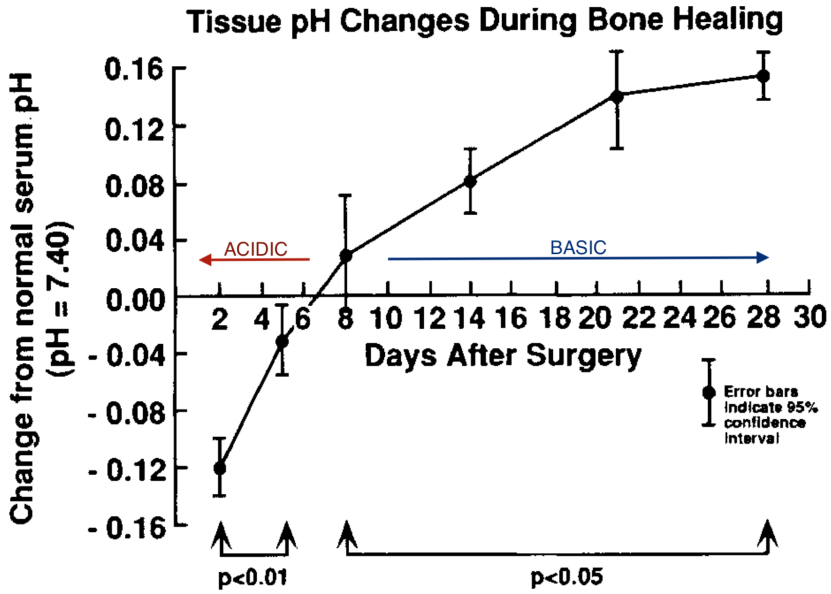

Figure 2.2: A graph outlining the pH changes in the surrounding bone area after large skeletal defects using a rat model. The change in pH is due to the bone resorption and deposition cycle that is seen after trauma (© Chakkalakal et al. (1994), included with permission).

et al. (2014) classified bone grafts into 5 main groups: Allograft-, cell-, factor-, ceramic- or polymer-based, each with certain advantages. Successful bone grafts have three main qualities that ensure successful osteoconduction (the ability for osteoblast cells to attach and grow onto the surface of a material), osteogenesis (the ability to bridge bone growth between the scaffold and surrounding cells), and osteoinductivity (the ability for the material/scaffold to dictate differentiation of stem cells) (Laurencin et al., 2014). One type of graft that meets all three osteogenic properties is the autograft or allograft, bone harvested from the patient or donor/cadaver, respectively. Natural bone is commonly used as a bone graft because it achieves optimal osteoconduction, osteogenesis, and osteoinductivity and is seen as the gold standard for bone regeneration. This material is not collected without risk, between 10–40% of the harvesting procedures reported complications such as nerve damage or hemorrhage (Zeng et al., 2018). Depending on the size of the defect, there are drawbacks to using natural

bone because of the limited material amount that can be collected (Zeng et al., 2018). Another obstacle of using natural bone as an osteo-scaffold is the chronic shortage of this valuable material (Beswick and Blom, 2011). Given these findings, there is the need to investigate the use of alternative materials for bone grafts. Cell-based bone grafts are either cell suspensions or cells seeded onto a scaffold that can be used to create new bone, such as the differentiation of mesenchymal stem cells into osteoblastic cells (Jaiswal et al., 1997). Factor-based bone grafts utilize growth factors, either natural or recombinant, that increase the formation of new bone. Common growth factors are bone-morphogenic proteins (BMP), proteins known for their osteoinductivity, especially BMP-2 and BMP-7 (Laurencin et al., 2014; Bialy et al., 2017). BMPs are classified as a transforming growth factor -β growth that can be used to modulate bone growth (Bialy et al., 2017). Both cell- and factor-based bone grafts are commonly paired with solid materials, such as ceramics or polymers, to allow both structural support with the benefits of the cell- or factor-based therapy. Ceramics are often used as bone grafts due to their similar compressive loading properties and can include bioactive glass, calcium sulphate, and calcium phosphate (Laurencin et al., 2014). These materials are optimal due to the incorporation of calcium being similar to that of the inorganic component of bone calcium, hydroxyapatite. Finally, there are polymer bone scaffolds that offer the largest customizability of both natural and synthetic polymer materials. Polymers can be designed with specific mechanical and chemical properties. Common bone graft polymers include poly(lactic) acid, poly(methyl methacrylate), poly(glycolic acid), and poly(ethylene) glycol (PEG) (Haugen et al., 2019; Kaito et al., 2005).

2.2 Polymers

2.2.1 Hydrogels

Hydrogels are defined as networks of hydrophilic polymers that are comprised of either natural or synthetic chains that can be polymerized to form 3D structures (Unagolla and Jayasuriya, 2020). Two types of cross-linking can be utilized in hydrogel creation. Chemically cross-linked hydrogels have been modified to connect monomers permanently at junctions, whereas physical cross-linking relies on entanglement of polymer chains, hydrophobic/hydrophilic interactions, and hydrogen bonds (Ahmed, 2015). Polymerization of these monomers can be achieved using heat, light, or chemical polymerization methods depending on the given application (Ahmed, 2015). PEG is one type of hydrogel comprised of repeating ethylene glycol monomers with various types of end groups that functionalize the monomer (D'souza and Shegokar, 2016). PEG is a bio-inert hydrogel, used for its ease of polymerization with Ultra-Violet (UV) light and low cytotoxicity (Unagolla and Jayasuriya, 2020). PEG is commonly used in drug delivery applications due to its ability to allow the steady diffusion of drug molecules inside the human body (D'souza and Shegokar, 2016; Hokugo et al., 2014). *In-vivo*, PEG has been shown to have low cell-adhesion and activation with little interaction with surrounding tissues, leading to a negligible immune response (D'souza and Shegokar, 2016). It should be noted that there have been extreme hypersensitivities to PEG, leading to this material being unusable in this portion of the population (Stone et al., 2019). To improve the success of PEG hydrogels as a tissue scaffold, recent studies have used ECM-elements, copolymers and NPs to increase the bioactivity of PEG (Zhu, 2010). These types of composite hydrogels overcome the previously outlined limitations of conventional materials. Post-grafting of peptides or proteins provides cell-adhesion cites (Drumheller and Hubbell, 1994; Lee et al., 2007). Copolymers, such as peptide-monoacrylates and -diacrylates, integrate into the hydrogel bulk, creating molecules that

cells can attach to more efficiently than coatings (Zhu, 2010). NPs incorporated into hydrogels offer increased cell-binding sites, modified mechanical properties, and secondary functionality depending on the NP chosen (Abalymov et al., 2020). For example, Carles-Carner et al. (2018) added hydroxyapatite NPs to PEG-based hydrogels capable of osteogenesis. A significant body of research has supported the use of hydrogels in bone regeneration applications, commonly for cell or growth factor delivery (Gibbs et al., 2016). For bone regeneration applications, researchers have incorporated biphasic calcium-phosphate NPs into Gelatin-PEG hydrogels that were shown to have optimal cell-adhesion and bio-mineralization, key for bone growth (Van et al., 2016). Kaito et al. (2005) used poly-lactic acid and PEG co-block polymer with the addition of hydroxyapatite for a biodegradable scaffold used for bone regeneration. This study showed the improved efficiency of BMP through diffusion but lacked a “smart” delivery system that responded to physiological conditions. Fu et al. (2012) used a triblock co-polymer of PEG-poly(ϵ-caprolactone)-PEG in conjunction with hydroxyapatite and collagen to show that these hydrogels had good bone regeneration when compared against the self-repair process. Although there is previous research into hydrogels for bone regeneration, there is significant applicability for these materials when paired with CPs.

2.2.2 PEG Photoinitiators

One type of chemical cross-linking of PEG is through the use of light. The UV light is used to excite photoinitiator molecules, classified as either cationic or free-radical (Zeng et al., 2021). Cationic, the less studied of the two methods, uses onium salts to produce acids when light is applied, causing polymerization (Sangermano, 2012). Type 1 radical photoinitiation works through hemolytic cleavage from a UV-excited triplet state, whereas type 2 radical photoinitiators work in conjunction with a co-initiator to produce radicals (Zeng et al., 2021). Common commercially available photoinitiators are often cytotoxic (Nguyen et al., 2013; Zeng et al., 2021). Zeng et al.

(2021) tested 7 common photoinitiators showing that phenylbis(acyl) phosphine oxides had the largest cytotoxicity while Diphenyl (2,4,6-trimethylbenzoyl) phosphine oxide, 4,4'-Bis(diethylamino) benzophenone, and 2-Isopropylthioxanthone and 2-Benzyl-2-(dimethylamino)-4'-morpholinobu tyrophenone, also known as Irgacure 369, all showed cytotoxic effects that increased at higher concentrations, leading to a limitation in the concentration used. Irgacure 2959, also known as hydroxy-1-[4-(hydroxyethoxy)phenyl]-2-methyl-1-propanone, is widely regarded as a biocompatible commercially available photoinitiator but has been demonstrated to be cytotoxic at concentrations over 0.015% w/v (Sabnis et al., 2009). Additionally, the type of cell line used influenced these results, Williams et al. (2005) showed that fetal human osteoblasts were extremely sensitive to Irgacure 2959. Naturally derived photoinitiation methods utilize molecules such as L-arginine (an amino acid), curcumin (turmeric root) and riboflavin (vitamin B2) (Kim and Chu, 2009; Zhao et al., 2015; Mishra and Daswal, 2005; Nguyen et al., 2013). Most interesting is riboflavin, a naturally occurring, non-toxic vitamin that has an absorption spectrum between 300 and 500 nm with peaks at 365 and 448 nm (Nguyen et al., 2013). The excitation of this molecule leads to the formation of a superoxide radicals, capable of initiating several reactions (Batchelor et al., 2016). Riboflavin alone cannot trigger PEG polymerization, a second co-initiator is needed. Kim and Chu (2009) utilized L-Arginine as an electron donor in conjunction with riboflavin in the polymerization of dextran methacrylate for biodegradable hydrogels. Dithiothreitol combined with riboflavin initiated thiol-ene polymerization of PEG hydrogels (Batchelor et al., 2016). Nguyen et al. (2013) used triethanolamine (TEA) as a co-initiator to riboflavin with a two-photon 3D printing method (described below in the Additive Manufacturing Section) to cure 3D PEG polymers with no cytotoxicity seen with the LIVE/DEAD assay. Given this, there is the need to investigate the use of riboflavin as a photoinitiator for the custom-designed OMASML 3D printer.

2.2.3 Conjugated Polymers

Conjugated polymers (CP), also know as Intrinsically Conducting Polymers (ICP), are a special classification of polymer with unique optoelectrical properties that offer a broad range of applications in the field of biomedical engineering (Bendrea et al., 2011). Polymers are typically excellent insulators however, these types of CPs have properties more similar to metals or semiconductors making them a distinct focus for research (Hamzah et al., 2007). The field of CP research has experienced significant growth after the awarding of the Nobel Prize in 2000 to Alan G. MacDiarmid, Alan J. Heeger, and Hideki Shirakawa and their work on CPs (Shirakawa et al., 1977). CPs are characterized by a backbone of alternating single and double bonds with delocalized π electrons (Hamzah et al., 2007). This arrangement leads to overlapping p-orbitals, with π electrons that are allowed to move between two nuclei, otherwise known as delocalized electrons (LibreTexts, 2020). The free π electron movement gives CPs their conductivity due to their ability to move between nuclei, transferring electrical charge along the polymer, unachievable in conventional polymers (Nezakati et al., 2018). There are many types of CPs that have been researched and offer varying mechanoelectrical properties and processability. They include polyaniline, polyphenylene, polythiophene, and PPy, seen in Figure 2.3 showing the conjugated bonding structure (Nezakati et al., 2018). One of the first well-studied CP was polyacetylene, this material was researched in 1977 to be conductive after n- or p- doping, allowing an increased conductivity due to the polymer entering a metallic-like state (Nezakati et al., 2018). The doping processes incorporates impurities into the polymer matrix, modifying the electrical conductivity. CPs have conductivities between 10^{-10} and 10^{-5} S/cm and up to 1 to 10^{4} S/cm using various dopants (Nezakati et al., 2018; MacDiarmid, 2001). The increase in conductivity overlaps with the range of metal conductivities between 10^{-4} to 10^{6} S/cm (Nezakati et al., 2018).

There are two common creation methods for CPs: chemical or electrochemical

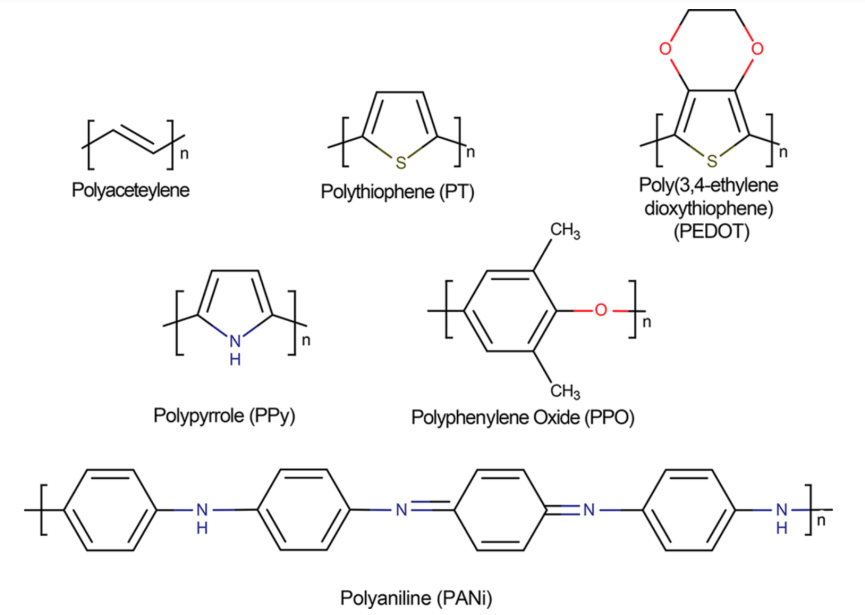

Figure 2.3: Chemical structures of common conjugated polymers that show the conjugated bonding arrangement of alternating double and single bonds that give rise to conductivity (© Nezakati et al. (2018), included with permission).

polymerization (Hamzah et al., 2007). During electrochemical creation, two electrodes are placed in a solution containing the solubilized monomer and an electrical potential is applied, causing a redox reaction to polymerize the polymer on the surface of the working electrode (Qu et al., 2004; Liubchak et al., 2020). This creation methodology results in thin films on the working electrode, commonly used to coat devices such as medical implants (Rikhari et al., 2020). Electrochemical synthesis offers the creation of highly conductive coatings with the ability to create complex hierarchical structures (Liubchak et al., 2020; Qu et al., 2004). Chemical polymerization uses an aqueous oxidant in a solution that contains solubilized monomer where a resulting redox reaction connects the individual monomer units into a polymer that is dispersed in the creation solution (Leonavicius et al., 2011). Synthesis using chemical processes usually results in a large quantity of polymer that is scalable at a reasonable cost (Hamzah et al., 2007).

Polymer	Chemical Formula	Conductivity (S/cm)
poly(p-phenylene)	$[C_6H_4]_n$	$10^{-3} - 10^2$
polyaniline	$[C_6H_4NH]_n$	$10^{-2} - 10^0$
polythiophene	$[C_4H_4S]_n$	$10^0 - 10^3$
polypyrrole	$[C_4H_2NH]_n$	$2 - 100$
polyacetylene	$[C_2H_2]_n$	10^5

Table 2.1: Common conjugated polymers with their chemical structures and ranging conductivity values that are a result of the structures described in Figure 2.3 Nezakati et al. (2018).

2.2.4 Polypyrrole

The most interesting CP to the OMASML group is PPy, an organic and biocompatible polymer that yields a high conductivity compared to other CPs (Wang et al., 2001; Nezakati et al., 2018). PPy is the polymer form of pyrrole, an organic compound that has an aromatic heterocyclic structure (Nezakati et al., 2018). During polymer formation, two pyrrole molecules each eliminate two hydrogen molecules, the free electrons are then able to bond to each other, creating sigma bonds between each aromatic unit (Street et al., 1985). PPy is similar to other CPs in that it has poor processability after creation, unable to be fused or solubilized, which restricts its applications (Wang et al., 2001). PPy is known to be brittle with no crystalline structure, leading to it being classified as an amorphous polymer (Fonner et al., 2008). The presence of dopant molecules in PPy chains can change the biocompatibility, cell adhesion, conductivity, and chemical exchange properties (Fonner et al., 2008; Bendrea et al., 2011; Jovanović et al., 1995).

Unlike other CPs, PPy is used most often in biomedical applications due to its biocompatibility with many cell types, such as catecholamine cells, Schwann cells, osteoblasts, and fibroblasts, and is capable of supporting local cell adhesion and subsequent cell growth (Fonner et al., 2008; Fahlgren et al., 2015; Guimard et al., 2007). Fonner et al. (2008) showed PPy doped with chloride, tosylate, polystyrene sulfonate all had various impacts on the final material properties. Chloride increased PPy roughness, tosylate increased PPy conductivity and both tosylate and polystyrene sulfonate increased

PPy cell adhesion when compared against each other. Given the biologic activity and conductivity of PPy many researchers have begun using it in biomedical applications. Vijayavenkataraman et al. (2019) used PPy combined with the co-polymer polycaprolactone to allow the 3D printing of porous nerve guide conduit with a max conductivity of 1.15 mS/cm and allowed the differentiation of neural crest stem cells. Two types of surface morphologies of PPy coating on titanium bone implants were investigated to visualize the impact of osteoblast cell adhesion, proliferation and differentiation (He et al., 2017). The rough surface of the PPy nanowire coatings supported increased osteoconductivity compared to traditional PPy surfaces and titanium (He et al., 2017). Additionally, electrical stimulation was applied to each of the substrates which yielded 2× higher proliferation activity and increased the expression and secretion of proteins when compared against no electrical stimulation (He et al., 2017). Electrical stimulation has been shown to increase bone healing and mineralization in multiple studies (Brighton et al., 1992; Wiesmann et al., 2001; Meng et al., 2013). Combining the conductive nature of PPy and applying electrical stimulation to increase cell activity is a natural advantage of this material. Yang et al. (2016) used PPy with hyaluronic acid hydrogels to create highly conductive hydrogels for broad tissue engineering applications.

PPy has also been used as a biosensing and drug delivery platform for various molecules *in-vivo* (Geetha et al., 2006). A redox reaction of the charged polymer allows positive, neutral and negatively charges molecules to become entrapped into, or repelled from, the CP (Tandon et al., 2017). Zanjanizadeh Ezazi et al. (2018) utilized mesoporous PPy/silica scaffolds as a delivery system for vancomycin, specifically looking at bone regeneration. The incorporation of PPy in the scaffolds allowed an increased dopant release of 80%, compared to scaffolds without PPy which only achieved 50% dopant release. As opposed to passive diffusion, there are methods of drug entrapment and release that are more controlled, such as electrical or pH-triggered release (Shah et al., 2018; Samanta et al., 2015). Electrochemical PPy dopant storage and release is based

on a redox reaction that occurs when a voltage is applied (Wadhwa et al., 2006). Shah et al. (2018) compared the release of dexamethasone phosphate and meropenem from PPy films and highlighted an increase of 10–15% and 10–30% compared to passive drug diffusion at each time point from electrical stimulation release using 30 s on at 0.6 V (a reducing potential). Hosseini-Nassab et al. (2016) showed the use of PPy NPs that were doped with insulin with an on-demand release by applying 1 V for a 2 min pulse. With each subsequent pulse, the release of insulin increased in a step-wise manner. Wadhwa et al. (2006) used PPy coatings that were doped and undoped with dexamethasone using cyclic voltammetry. After 1 release cycle 0.5 $\mu g/cm^2$ was achieved, totalling 16 $\mu g/cm^2$ after 30 cycles, showing the very controlled means of release using electrical methods. Although electrical release is useful, these controlled voltages are not seen inside the human body and require external stimuli, leading to the investigation of other stimuli methods. pH-sensitive release for PPy has been described by Samanta et al. (2015) using PPy NPs doped with fluorescein, rhodamine-6G and piroxicam. This author entrapped the drug molecules during PPy polymerization and triggered release using various pH solutions. Drug release from the NPs showed that negatively charged molecules (fluorescein and piroxicam) favoured release at pH 7.4 and 8 compared to pH 2 and 5. This was validated by Liubchak et al. (2020) with fluorescein release from electrochemically doped PPy films showing a marked increase in release at alkaline pH values. Samanta et al. (2015) described the process of dopant release as a mixture of both electrostatic and hydrophobic interactions and that the higher pH causes PPy deprotonation, therefore lowering the overall positive PPy backbone charge and allowing the release of charged molecules. Given this literature, there is interest in using PPy as an *in-vivo* drug delivery vehicle that can respond to changes in pH in conjugation with hydrogels.

2.3 Additive Manufacturing

2.3.1 Classifications

Additive Manufacturing (AM), otherwise known as 3D printing, is an emerging and exciting creation methodology with a wide variety of applications. It uses computer-assisted design (CAD) models and allows them to be turned into fully realized objects through the layer-by-layer deposition of material. There are many classifications of AM but they can be broken down into four main categories: extrusion-based, laser-assisted, inkjet, and stereolithography, each offering specific advantages (Unagolla and Jayasuriya, 2020). Briefly, extrusion-based 3D printing is a low-cost technique that most individuals think of when considering 3D printing. It involves creating a structure from the bottom-up where the material is being forced out of a nozzle through heating or pressure gradients (Vaezi et al., 2018; Unagolla and Jayasuriya, 2020). Extrusion-based printing is seen as simple and cost-effective but comes with a slow print speed and limitation of resolution based on nozzle diameter (Murphy and Atala, 2014). Laser-assisted 3D printing used a two-layer setup where a laser is focused on the upper absorbing substrate and the lower substrate acts as the collector, slowly building the print with each laser pulse. This method offers microscale resolution but with a trade-off of high price and preparation time (Murphy and Atala, 2014; Unagolla and Jayasuriya, 2020). Inkjet printing offers a fast printing time through an aerosol-based system that forces material droplets out of the nozzle onto a substrate to build up the print (Murphy and Atala, 2014). Finally, stereolithography falls into the category of vat-polymerization. This method uses liquid resins that can be solidified with UV light patterns projected onto the surface of the resin, curing one thin layer at a time, seen in Figure 2.4 (FormLabs, 2021; Cullen, 2018). AM, specifically looking at stereolithography, offers a very high resolution with a fast printing time (Murphy and Atala, 2014; Unagolla and Jayasuriya, 2020).

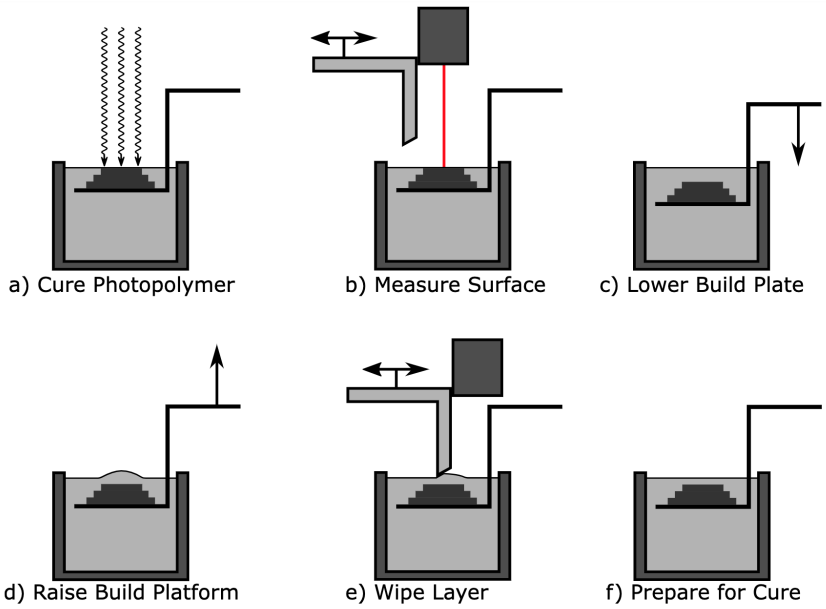

Figure 2.4: The process diagram for the stereolithography additive manufacturing highlighting the repetitive process of (a) curing a thin polymer layer, (b) measuring the height to the resin surface, (c & d) lowering the build plate to expose a fresh layer of uncured resin, (e) measuring distance to resin surface and finally, (f) preparing for the next layer cure (© Cullen and Price (2019), included with permission).

2.3.2 Applications

Given that there are major limitations to the creation methodology and vast applications for CPs, the OMASML group has worked to investigate the use of AM with CPs. Cullen (2018) researched 3D printed PPy/Urethane Dimethacrylate and PPy/bisphenol A ethoxylate dimethacrylate resins using stereolithography techniques and was able to create complex 3D shapes, typically unachievable with traditional creation methods for CPs. Holness (2017) combined polyaniline with dodecylbenzenesulfonic acid into a paste for extrusion-based 3D printing applications and was able to achieve customizable polyaniline shapes and patterns with a layer thickness of 200 μm and an XY resolution of approximately 2 mm.

Bioprinting involves applying the previously outlined additive manufacturing techniques with living cells and biologic, growth and differentiation factors for the creation of tissue engineering applications (Unagolla and Jayasuriya, 2020). The biologic applications of 3D printing are wide, ranging from 3D printed corneas to allowing surgeons to better prepare for complex surgeries (Isaacson et al., 2018; Shilo et al., 2018). In Tissue Engineering (TE), the creation of complex structures that match the physical, mechanical and physiological properties of native tissues is often difficult due to inflexible processing methods (Vaezi et al., 2018). Bioprinting is a customizable method that can involve patient imagining, material selection, cell selection, printing and application, each step allowing a range of choices and customizations to better model living tissue to ensure biomimicry (Murphy and Atala, 2014). Kang et al. (2016) demonstrated the capabilities of an “integrated tissue–organ printer” printing biodegradable polymers in conjunction with cell-laden hydrogels using extrusion based methods. Cristovão et al. (2019) showed the capabilities of extrusion based 3D printing tracheal implants design. Nguyen et al. (2013) showed the use of a two-photon stereolithography printer for the creation of cell scaffolds. Many applications of 3D bioprinting implement a hydrogel formulation due to their cell-compatibility and ease of crosslinking (Unagolla and Jayasuriya, 2020). Addi-

tionally, the previously outlined methods of AM CPs has been applied to bioprinting. Ma et al. (2019) used PPy NPs paired with extrusion based 3D printing to create structures that better match complex tissue types. Vijayavenkataraman et al. (2019) used PPy and collagen for neural tissue devices but also used extrusion based 3D printing methods. Li et al. (2018) successfully used extrusion based 3D printing to create poly-lactic acid PPy scaffolds for bone regeneration with hydroxyapatite particles and dexamethasone delivery. Stereolithography printing of CPs for biomedical applications has yet to be researched and is the basis of this thesis.

2.4 Chapter summary

This chapter has outlined the necessary information pertaining to the research completed in the following chapters. It has covered three key aspects to this project: bone, polymers and AM. Specifically, the physiological characteristics of both bone and bone graft allow the visualization of the tissue that is most important to this thesis. Polymers, highlighting both hydrogels and conjugated polymers, along with the current research in each field was presented. Finally, the various types of AM were explored with an emphasis on bioprinting.

List of references

Abalymov, A. A., Parakhonskiy, B. V. and Skirtach, A. G. (2020), 'Colloids-at-surfaces: Physicochemical approaches for facilitating cell adhesion on hybrid hydrogels', *Colloids and Surfaces A: Physicochemical and Engineering Aspects* **603**, 125185.

Ahmed, E. M. (2015), 'Hydrogel: Preparation, characterization, and applications: A review', *Journal of Advanced Research* **6**(2), 105–121.

Balmer, T. W., Vesztergom, S., Broekmann, P., Stahel, A. and Büchler, P. (2018), 'Characterization of the electrical conductivity of bone and its correlation to osseous structure', *Scientific Reports* **8**(1), 8601.

Batchelor, R. R., Kwandou, G., Spicer, P. T. and Stenzel, M. H. (2016), '(-)-Riboflavin (vitamin B2) and flavin mononucleotide as visible light photo initiators in the thiol–ene polymerisation of PEG-based hydrogels', *Polymer Chemistry* **8**(6), 980–984.

Bendrea, A.-D., Cianga, L. and Cianga, I. (2011), 'Review paper: Progress in the Field of Conducting Polymers for Tissue Engineering Applications', *Journal of Biomaterials Applications* **26**(1), 3–84.

Beswick, A. and Blom, A. W. (2011), 'Bone graft substitutes in hip revision surgery: a comprehensive overview.', *Injury* **42 Suppl 2**, S40–6.

Bialy, I. E., Jiskoot, W. and Nejadnik, M. R. (2017), 'Formulation, Delivery and Stability of Bone Morphogenetic Proteins for Effective Bone Regeneration', *Pharmaceutical Research* **34**(6), 1152–1170.

Brighton, C. T., Okereke, E., Pollack, S. R. and Clark, C. C. (1992), 'In vitro bone-cell response to a capacitively coupled electrical field. the role of field strength, pulse pattern, and duty cycle.', *Clin Orthop Relat Res* (285), 255–262.

Carles-Carner, M., Saleh, L. S. and Bryant, S. J. (2018), 'The effects of hydroxyapatite nanoparticles embedded in a MMP-sensitive photoclickable PEG hydrogel on encapsulated MC3T3-E1 pre-osteoblasts', *Biomedical Materials* **13**(4), 045009.

Chakkalakal, D. A., Mashoof, A. A., Novak, J., Strates, B. S. and McGuire, M. H. (1994), 'Mineralization and ph relationships in healing skeletal defects grafted with demineralized bone matrix', *Journal of Biomedical Materials Research* **28**(12), 1439–1443.

Clarke, B. (2008), 'Normal bone anatomy and physiology.', *Clin J Am Soc Nephrol* **3 Suppl 3**(Suppl 3), S131–9.

Cristovão, A. F., Sousa, D., Silvestre, F., Ropio, I., Gaspar, A., Henriques, C., Velhinho, A., Baptista, A. C., Faustino, M. and Ferreira, I. (2019), 'Customized tracheal design using 3D printing of a polymer hydrogel: influence of UV laser cross-linking on mechanical properties', *3D Printing in Medicine* **5**(1), 12.

Cullen, A. (2018), 'Fabrication of 3d conjugated polymer structures via vat polymerization additive manufacturing', *Electronic Thesis and Dissertation Repository* .

Cullen, A. T. and Price, A. D. (2019), 'Fabrication of 3d conjugated polymer structures via vat polymerization additive manufacturing', *Smart Materials and Structures* **28**(10), 104007.

Drumheller, P. D. and Hubbell, J. A. (1994), 'Polymer networks with grafted cell adhesion peptides for highly biospecific cell adhesive substrates.', *Anal Biochem* **222**(2), 380–388.

D'souza, A. A. and Shegokar, R. (2016), 'Polyethylene glycol (peg): a versatile polymer for pharmaceutical applications', *Expert Opinion on Drug Delivery* **13**(9), 1257–1275. PMID: 27116988.

Fahlgren, A., Bratengeier, C., Gelmi, A., Semeins, C. M., Klein-Nulend, J., Jager, E. W. H. and Bakker, A. D. (2015), 'Biocompatibility of Polypyrrole with Human Primary Osteoblasts and the Effect of Dopants', *PLOS ONE* **10**(7), e0134023.

Fonner, J. M., Forciniti, L., Nguyen, H., Byrne, J. D., Kou, Y.-F., Syeda-Nawaz, J. and Schmidt, C. E. (2008), 'Biocompatibility implications of polypyrrole synthesis techniques.', *Biomedical materials (Bristol, England)* **3**(3), 034124.

FormLabs (2021), 'Guide to stereolithography (sla) 3d printing'.

Fu, S., Ni, P., Wang, B., Chu, B., Zheng, L., Luo, F., Luo, J. and Qian, Z. (2012), 'Injectable and thermo-sensitive peg-pcl-peg copolymer/collagen/n-ha hydrogel composite for guided bone regeneration', *Biomaterials* **33**(19), 4801–4809.

Galow, A.-M., Rebl, A., Koczan, D., Bonk, S. M., Baumann, W. and Gimsa, J. (2017), 'Increased osteoblast viability at alkaline pH in vitro provides a new perspective on bone regeneration', *Biochemistry and Biophysics Reports* **10**, 17–25.

Geetha, S., Rao, C., Vijayan, M. and Trivedi, D. (2006), 'Biosensing and drug delivery by polypyrrole', *Analytica Chimica Acta* **568**(1-2), 119–125.

Gibbs, D. M. R., Black, C. R. M., Dawson, J. I. and Oreffo, R. O. C. (2016), 'A review of hydrogel use in fracture healing and bone regeneration', *Journal of Tissue Engineering and Regenerative Medicine* **10**(3), 187–198.

Guimard, N. K., Gomez, N. and Schmidt, C. E. (2007), 'Conducting polymers in biomedical engineering', *Progress in Polymer Science* **32**(8-9), 876–921.

Hamzah, M., Saion, E., Kassim, A. and Yahya, N. (2007), 'Conjugated conducting polymers: A brief overview', *Springer Ser. Solid State Sci.* **102**.

Haugen, H. J., Lyngstadaas, S. P., Rossi, F. and Perale, G. (2019), 'Bone grafts: which is the ideal biomaterial?', *Journal of Clinical Periodontology* **46**(S21), 92–102.

He, Y., Wang, S., Mu, J., Dai, L., Zhang, Z., Sun, Y., Shi, W. and Ge, D. (2017), 'Synthesis of polypyrrole nanowires with positive effect on MC3T3-E1 cell functions through electrical stimulation', *Materials Science and Engineering: C* **71**, 43–50.

Hokugo, A., Saito, T., Li, A., Sato, K., Tabata, Y. and Jarrahy, R. (2014), 'Stimulation of bone regeneration following the controlled release of water-insoluble oxysterol from biodegradable hydrogel', *Biomaterials* **35**(21), 5565–5571.

Holness, F. (2017), 'Additive manufacturing process of 3d polyaniline transducers via direct ink writing', *Electronic Thesis and Dissertation Repository* .

Hosseini-Nassab, N., Samanta, D., Abdolazimi, Y., Annes, J. P. and Zare, R. N. (2016), 'Electrically controlled release of insulin using polypyrrole nanoparticles.', *Nanoscale* **9**(1), 143–149.

Isaacson, A., Swioklo, S. and Connon, C. J. (2018), '3d bioprinting of a corneal stroma equivalent.', *Exp Eye Res* **173**, 188–193.

Jaiswal, N., Haynesworth, S. E., Caplan, A. I. and Bruder, S. P. (1997), 'Osteogenic differentiation of purified, culture-expanded human mesenchymal stem cells in vitro', *Journal of Cellular Biochemistry* **1097**(4644).

Jovanović, V. M., Markičević, L., Stanković, S., Stanković, R. and Jovanović, M. S. (1995), 'The behavior of polypyrrole doped with different anions as an ion-selective electrode', *Electroanalysis* **7**(6), 574–578.

Kaito, T., Myoui, A., Takaoka, K., Saito, N., Nishikawa, M., Tamai, N., Ohgushi, H. and Yoshikawa, H. (2005), 'Potentiation of the activity of bone morphogenetic protein-2 in bone regeneration by a pla–peg/hydroxyapatite composite', *Biomaterials* **26**(1), 73–79.

Kang, H.-W., Lee, S. J., Ko, I. K., Kengla, C., Yoo, J. J. and Atala, A. (2016), 'A 3D bioprinting system to produce human-scale tissue constructs with structural integrity', *Nature Biotechnology* **34**(3), 312–319.

Karageorgiou, V. and Kaplan, D. (2005), 'Porosity of 3D biomaterial scaffolds and osteogenesis', *Biomaterials* **26**(27), 5474–5491.

Kim, S.-H. and Chu, C.-C. (2009), 'Fabrication of a biodegradable polysaccharide hydrogel with riboflavin, vitamin B2, as a photo-initiator and L-arginine as coinitiator

upon UV irradiation', *Journal of Biomedical Materials Research Part B: Applied Biomaterials* **91B**(1), 390–400.

Kumar, P., Vinitha, B. and Fathima, G. (2013), 'Bone grafts in dentistry.', *J Pharm Bioallied Sci* **5**(Suppl 1), S125–7.

Laurencin, C., Khan, Y. and El-Amin, S. F. (2014), 'Bone graft substitutes', *Expert Review of Medical Devices* **3**(1), 49–57.

Lee, W., Lee, T. and Koh, W.-G. (2007), 'Grafting of poly(acrylic acid) on the poly(ethylene glycol) hydrogel using surface-initiated photopolymerization for covalent immobilization of collagen', *JOURNAL OF INDUSTRIAL AND ENGINEERING CHEMISTRY -SEOUL-* **13**, 1195–1200.

Leonavicius, K., Ramanaviciene, A. and Ramanavicius, A. (2011), 'Polymerization Model for Hydrogen Peroxide Initiated Synthesis of Polypyrrole Nanoparticles', *Langmuir* **27**(17), 10970–10976.

Li, X., Wang, Y., Wang, Z., Qi, Y., Li, L., Zhang, P., Chen, X. and Huang, Y. (2018), 'Composite PLA/PEG/nHA/Dexamethasone Scaffold Prepared by 3D Printing for Bone Regeneration', *Macromolecular Bioscience* **18**(6), 1800068.

LibreTexts (2020), 'Overlap of adjacent p orbitals-electron delocalization'.

Liubchak, I., Lawrence, M. T., Holness, F. B. and Price, A. D. (2020), 'Soft template electropolymerization of polypyrrole for improved ph-induced drug delivery', *International Journal of Molecular Sciences* **21**(21).

Ma, C., Jiang, L., Wang, Y., Gang, F., Xu, N., Li, T., Liu, Z., Chi, Y., Wang, X., Zhao, L., Feng, Q. and Sun, X. (2019), '3D Printing of Conductive Tissue Engineering Scaffolds Containing Polypyrrole Nanoparticles with Different Morphologies and Concentrations', *Materials* **12**(15), 2491.

MacDiarmid, A. G. (2001), "'synthetic metals": A novel role for organic polymers (nobel lecture)', *Angewandte Chemie International Edition* **40**(14), 2581–2590.

Meng, S., Rouabhia, M. and Zhang, Z. (2013), 'Electrical stimulation modulates osteoblast proliferation and bone protein production through heparin-bioactivated conductive scaffolds', *Bioelectromagnetics* **34**(3), 189–199.

Mishra, A. and Daswal, S. (2005), 'Curcumin, a novel natural photoinitiator for the copolymerization of styrene and methylmethacrylate', *Journal of Macromolecular Science, Part A* **42**(12), 1667–1678.

Murphy, S. V. and Atala, A. (2014), '3d bioprinting of tissues and organs', *Nature Biotechnology* **32**(8), 773–785.

Nair, A. K., Gautieri, A., Chang, S.-W. and Buehler, M. J. (2013), 'Molecular mechanics of mineralized collagen fibrils in bone.', *Nat Commun* **4**, 1724.

Nezakati, T., Seifalian, A., Tan, A. and Seifalian, A. M. (2018), 'Conductive Polymers: Opportunities and Challenges in Biomedical Applications', *Chemical Reviews* **118**(14), 6766–6843.

Nguyen, A. K., Gittard, S. D., Koroleva, A., Schlie, S., Gaidukeviciute, A., Chichkov, B. N. and Narayan, R. J. (2013), 'Two-photon polymerization of polyethylene glycol diacrylate scaffolds with riboflavin and triethanolamine used as a water-soluble photoinitiator', *Regenerative Medicine* **8**(6), 725–738.

Qu, L., Shi, G., Yuan, J., Han, G. and Chen, F. (2004), 'Preparation of polypyrrole microstructures by direct electrochemical oxidation of pyrrole in an aqueous solution of camphorsulfonic acid', *Journal of Electroanalytical Chemistry* **561**, 149–156.

Rikhari, B., Mani, S. P. and Rajendran, N. (2020), 'Polypyrrole/graphene oxide composite

coating on ti implants: a promising material for biomedical applications', *Journal of Materials Science* **55**(12), 5211–5229.

Sabnis, A., Rahimi, M., Chapman, C. and Nguyen, K. T. (2009), 'Cytocompatibility studies of an in situ photopolymerized thermoresponsive hydrogel nanoparticle system using human aortic smooth muscle cells', *Journal of Biomedical Materials Research Part A* **91A**(1), 52–59.

Samanta, D., Meiser, J. L. and Zare, R. N. (2015), 'Polypyrrole nanoparticles for tunable, pH-sensitive and sustained drug release', *Nanoscale* **7**(21), 9497–9504.

Sangermano, M. (2012), 'Advances in cationic photopolymerization', *Pure and Applied Chemistry* **84**(10), 2089–2101.

Schneider, L. A., Korber, A., Grabbe, S. and Dissemond, J. (2007), 'Influence of pH on wound-healing: a new perspective for wound-therapy?', *Archives of Dermatological Research* **298**(9), 413–420.

Shah, S., Firlak, M., Berrow, S., Halcovitch, N., Baldock, S., Yousafzai, B., Hathout, R. and Hardy, J. (2018), 'Electrochemically enhanced drug delivery using polypyrrole films', *Materials* **11**(7), 1123.

Shilo, D., Emodi, O., Blanc, O., Noy, D. and Rachmiel, A. (2018), 'Printing the future—updates in 3d printing for surgical applications', *Rambam Maimonides Medical Journal* **9**(3), e0020.

Shirakawa, H., Louis, E. J., MacDiarmid, A. G., Chiang, C. K. and Heeger, A. J. (1977), 'Synthesis of electrically conducting organic polymers: halogen derivatives of polyacetylene, (CH) x', *Journal of the Chemical Society, Chemical Communications* (16), 578.

Stone, C. A., Liu, Y., Relling, M. V., Krantz, M. S., Pratt, A. L., Abreo, A., Hemler, J. A. and Phillips, E. J. (2019), 'Immediate hypersensitivity to polyethylene glycols and polysorbates: More common than we have recognized', *The Journal of Allergy and Clinical Immunology: In Practice* **7**(5), 1533–1540.e8.

Street, G. B., Lindsey, S. E., Nazzal, A. I. and Wynne, K. J. (1985), 'The structure and mechanical properties of polypyrrole', *Molecular Crystals and Liquid Crystals* **118**(1), 137–148.

Tandon, B., Magaz, A., Balint, R., Blaker, J. J. and Cartmell, S. H. (2017), 'Electroactive biomaterials: Vehicles for controlled delivery of therapeutic agents for drug delivery and tissue regeneration', *Advanced Drug Delivery Reviews* (J. Eur. Acad. Dermatol. Venereol. 26 2012).

Unagolla, J. M. and Jayasuriya, A. C. (2020), 'Hydrogel-based 3d bioprinting: A comprehensive review on cell-laden hydrogels, bioink formulations, and future perspectives', *Applied Materials Today* **18**, 100479.

Vaezi, M., Zhong, G., Kalami, H. and Yang, S. (2018), 10 - extrusion-based 3d printing technologies for 3d scaffold engineering, *in* Y. Deng and J. Kuiper, eds, 'Functional 3D Tissue Engineering Scaffolds', Woodhead Publishing, pp. 235–254.

Van, T. D., Tran, N. Q., Nguyen, D. H., Nguyen, C. K., Tran, D. L. and Nguyen, P. T. (2016), 'Injectable Hydrogel Composite Based Gelatin-PEG and Biphasic Calcium Phosphate Nanoparticles for Bone Regeneration', *Journal of Electronic Materials* **45**(5), 2415–2422.

Vijayavenkataraman, S., Kannan, S., Cao, T., Fuh, J. Y. H., Sriram, G. and Lu, W. F. (2019), '3d-printed pcl/ppy conductive scaffolds as three-dimensional porous nerve guide conduits (ngcs) for peripheral nerve injury repair', *Frontiers in Bioengineering and Biotechnology* **7**, 266.

Wadhwa, R., Lagenaur, C. F. and Cui, X. T. (2006), 'Electrochemically controlled release of dexamethasone from conducting polymer polypyrrole coated electrode', *Journal of Controlled Release* **110**(3), 531–541.

Wang, L.-X., Li, X.-G. and Yang, Y.-L. (2001), 'Preparation, properties and applications of polypyrroles', *Reactive and Functional Polymers* **47**(2), 125 – 139.

Wang, W. and Yeung, K. W. K. (2017), 'Bone grafts and biomaterials substitutes for bone defect repair: A review.', *Bioact Mater* **2**(4), 224–247.

Wiesmann, H.-P., Hartig, M., Stratmann, U., Meyer, U. and Joos, U. (2001), 'Electrical stimulation influences mineral formation of osteoblast-like cells in vitro', *Biochimica et Biophysica Acta (BBA) - Molecular Cell Research* **1538**(1), 28–37.

Williams, C. G., Malik, A. N., Kim, T. K., Manson, P. N. and Elisseeff, J. H. (2005), 'Variable cytocompatibility of six cell lines with photoinitiators used for polymerizing hydrogels and cell encapsulation', *Biomaterials* **26**(11), 1211–1218.

Yang, J., Choe, G., Yang, S., Jo, H. and Lee, J. Y. (2016), 'Polypyrrole-incorporated conductive hyaluronic acid hydrogels', *Biomaterials Research* **20**(1), 31.

Zanjanizadeh Ezazi, N., Shahbazi, M.-A., Shatalin, Y. V., Nadal, E., Mäkilä, E., Salonen, J., Kemell, M., Correia, A., Hirvonen, J. and Santos, H. A. (2018), 'Conductive vancomycin-loaded mesoporous silica polypyrrole-based scaffolds for bone regeneration', *International Journal of Pharmaceutics* **536**(1), 241–250.

Zeng, B., Cai, Z., Lalevée, J., Yang, Q., Lai, H., Xiao, P., Liu, J. and Xing, F. (2021), 'Cytotoxic and cytocompatible comparison among seven photoinitiators-triggered polymers in different tissue cells.', *Toxicol In Vitro* **72**, 105103.

Zeng, J.-H., Liu, S.-W., Xiong, L., Qiu, P., Ding, L.-H., Xiong, S.-L., Li, J.-T., Liao, X.-G.

and Tang, Z.-M. (2018), 'Scaffolds for the repair of bone defects in clinical studies: a systematic review', *Journal of Orthopaedic Surgery and Research* **13**(1).

Zhao, J., Lalevée, J., Lu, H., MacQueen, R., Kable, S. H., Schmidt, T. W., Stenzel, M. H. and Xiao, P. (2015), 'A new role of curcumin: as a multicolor photoinitiator for polymer fabrication under household uv to red led bulbs', *Polym. Chem.* **6**, 5053–5061.

Zhu, J. (2010), 'Bioactive modification of poly(ethylene glycol) hydrogels for tissue engineering', *Biomaterials* **31**(17), 4639–4656.

Chapter 3

Development and Characterization of Polypyrrole and Poly(ethylene) Glycol Copolymer Resin Blend

This chapter outlines the process of creating a PPy/PEGDA photoactive resin blend. PPy NPs were created through oxidative polymerization and incorporated into PEGDA resin to form a composite biomaterial. Characterization of the photo-initiated resin was completed before moving to Chapter 4: *PPy/PEGDA Composite Resin Application*.

3.1 Introduction

Traditional PPy synthesis methods are limited and lead to polymers with poor processability (Wang et al., 2001). This has hindered the use of PPy in applications that require flexibility, such as 3D printing. One method of overcoming these poor material properties is by combining PPy with a second polymer which offers complimentary characteristics. This two-polymer composition was the basis of the following experiments. The goal of this chapter relates to the first objective of developing a biocompatible PPy

resin that was capable of being printed on a UV-based stereolithography 3D printer. This overarching goal extended between the material selection, creation and processing aspects of this chapter to ensure that steps were taken so the material would be successfully 3D printed while having low cytotoxicity. To achieve this, PPy NPs were incorporated into UV-curable PEGDA hydrogels with a natural photoinitiator, riboflavin. PPy NPs offered a high surface-area-to-volume ratio, potential drug delivery ability and electrical conductivity whereas hydrogels provided a customizable 3D polymer with high biocompatibility and easily crosslinked through various methods (Samanta et al., 2015; Unagolla and Jayasuriya, 2020). Previous works have studied PPy NPs and/or hydrogels alone, no researchers have worked to characterize a composite PPy/PEGDA material. To understand the composite PPy/PEGDA material, studies into PPy NPs, PEGDA hydrogel matrices and the interaction between these two materials were completed through UV-absorption, cure tests, swelling ratio studies and conductivity measurements. The results of these tests showed a successfully cured PPy/PEGDA biomaterial using riboflavin. Characterization of this bio-composite helped elucidate the interaction of the two distinct materials, the hydrogel and the NPs. The composite material showed a decreased swelling ratio and increased conductivity with each addition of PPy NPs, to a maximum of 0.75% PPy. Above this limit, the NPs inhibited proper excitation of the riboflavin molecule and the polymers were unable to cure. The following work has successfully created a flexible biomaterial that harnesses the benefits of PPy within a customizable PEGDA hydrogel format.

3.2 Materials and Methods

3.2.1 Materials

Pyrrole (CAS #109-97-7) was distilled prior to use to remove any impurities. Hydrochloric acid (HCl) (CAS #7647-01-0) was diluted to 40 mmol/l with deionized H_2O. Sodium do-

decyl sulfate (SDS) (CAS #151-21-3), PEGDA (Mn=700, CAS #26570-48-9), riboflavin (CAS #83-88-5), TEA (CAS #102-71-6), Irgacure 2959 (CAS #106797-53-9), 30% hydrogen peroxide (H_2O_2) (CAS #7722-84-1), Isopropyl alcohol (IPA) (CAS # 67-63-0) and phosphate-buffered saline (PBS) (Fisher Cat. #10010023, 144 mg/ml Potassium Phosphate monobasic, 9000 mg/ml Sodium Chloride, 795 mg/ml Sodium Phosphate dibasic) were all used as received. 3.5K MWCO dialysis tubing was purchased from ThermoFisher (Cat. #88242) and 3K NMWL Ultra-15 centrifugal filter units were purchased from Millipore Sigma (Cat. #UFC900308).

3.2.2 Methods

PPy NPs were created by dissolving 144 mg of SDS in 5 ml of 40 mmol/l HCl, stirred at 200 r/min in a 20 ml beaker with a 2 cm egg-shaped stir bar on a magnetic hot plate. After the SDS was dissolved, the rotational speed was increased to 1200 r/min and 1 ml of distilled pyrrole was added in a drop-wise manner. Immediately after the addition of pyrrole, 2 ml of 30% H_2O_2 was added in a drop-wise manner. The mixture was left for 24 h at 1200 r/min to completely polymerize. The solution was moved into a pre-soaked 3.5K MWCO dialysis bag that was placed in 1 l of deionized H_2O. The H_2O was changed every 24 h for 5 d. After the wash period, the solution was sonicated for 1 h in a bath sonicator to break up any agglomerated NPs. Concentration measurements were completed using evaporation in triplicate, measuring the beaker mass before and after evaporation of 100 μl of solution to calculate the mass of PPy /ml. NP size was measured by diluting 100 μl of NP solution in 10 ml of deionized H_2O and placing the solution into a 90Plus/BI-MAS Zeta particle sizing machine which measured 10$\times$/sample. From the Zeta sizing machine, the mean diameter and polydispersity were averaged over 10 runs for each sample was collected. Particle morphology was analyzed by evaporating a small sample of the washed PPy NP suspension on a glass slide. A Keyence VHX-7000 optical microscope was used to visualize NP morphology

on a micro-scale. Scanning electron microscopy (SEM) was used to visualize the nano-scale of the PPy NPs. Silicon wafers were coated with iridium before pipetting the NP solution on top. The samples were dried fully before being imaged using a Hitachi SU8230 SEM with a 5 kV accelerating voltage and secondary electron mode. Polymers were left uncoated during SEM to not obstruct the PPy NP surface morphology.

A 0.01 mg/ml Irgacure 2959 solution and 0.11 mg/ml riboflavin solution were created and read using a Cary 60 UV-vis spectrophotometer, the absorbance between $200 - 550$ nm was collected. PEGDA resins were created using a 1:1 PEGDA:H_2O ratio (described by Nguyen et al. (2013)) with varying concentrations of TEA. Six resins with the following ratios of PEGDA:TEA were used: 36:1, 28:1, 20:1, 12:1, 4:1 and 3.2:1. Riboflavin concentration was kept constant throughout these tests to ensure there were no confounding variable effects. The maximum concentration of riboflavin was added based off the solubility of 0.3 g/l of H_2O (Sigma-Aldrich, 2021). For each test resin, 5 ml of PEGDA was combined with 5 ml of H_2O and 1.5 mg of riboflavin. The mixture was sonicated to allow the riboflavin to fully dissolve. After dissolution, the desired amount of TEA was added and the resin was vortexed. All resins were protected from light before curing to prevent photobleaching. Absorbance was measured by diluting 1 ml of resin with 10 ml of H_2O. Samples were read using a Cary 60 UV-vis spectrophotometer and the absorbance between $300 - 500$ nm was collected.

PPy resins were created using a 1:1 PEGDA:H_2O and 12:1 PEGDA:TEA ratio. Five concentrations of NP solution were created 0, 0.1, 0.25, 0.5 and 0.75 wt%. PPy resins will be referred to as the wt% of the NP solution used for creation here on in. Based off the g PPy /ml measurements, solutions were either diluted or placed into a 3K NMWL Ultra-15 centrifugal filter unit for 20 min at 3,270 (x*g*) RCF using an Allegra X-12R centrifuge to concentrate the particles. Once the correct wt% were created, 5 ml of the PPy solution was added to 5 ml of PEGDA with 1.5 mg of riboflavin and 42 µl of TEA. The resin was sonicated and protected from light before testing. An

identical UV absorbance preparation and collection process was followed for the PPy resins compared to the TEA resins. To complete the swelling ratio tests, 160 µl of resin was pipetted into 1 cm × 1.5 cm transparent polydimethylsiloxane molds in triplicate. Polymers were cured using a 400 nm Prusa CW1. The 0, 0.1, 0.25, 0.5 and 0.75 PPy resins were cured for 30, 40, 50, 60 and 60 min, respectively to obtain a solid polymer. Each polymer was rinsed in IPA after printing to wash away the uncured monomers and left to dry. Once dry, the polymers were weighed and placed into H_2O for 24 h. After swelling, any excess water from the surface was absorbed with a paper towel and the mass was recoded again. The swelling ratio was calculated using the following equation:

$$Swelling\ Ratio = \frac{m_s - m_d}{m_d} \tag{3.1}$$

where m_s was the mass of the swollen polymer and m_d was the mass of the rinsed and dried polymer before swelling. In addition to swelling ratio, the average molecular weight between crosslinks, M_c, of the polymers were calculated using the following parameters and formulas (Lin and Metters, 2006; Lin et al., 2011):

$$\frac{1}{\overline{M_C}} = \frac{2}{\overline{M_n}} - \frac{\left(\bar{v}/V_1\right)\left[\ln\left(1 - v_{2,\,s}\right) + v_{2,\,s} + \chi_1 v_{2,\,s}^2\right]}{v_{2,r}\left[\left(\frac{v_{2,s}}{v_{2,r}}\right)^{1/3} - \frac{v_{2,s}}{2v_{2,r}}\right]} \tag{3.2}$$

where $\overline{M_n}$ was the average weight of the PEGDA (700 Mn), $\bar{v}$ was the specific volume of PEGDA (0.893 cm^3/g), V_1 was the molar volume of water (18 cm^3/mol), χ_1 was the Flory-Huggin's PEG-water interaction parameter (0.426), $v_{2,r}$ was the polymer fraction (0.5 for this resin composition) and $v_{2,s}$ was the polymer volume fraction in the swollen state, defined by the following formula:

$$v_{2,s} = \frac{\frac{1}{\rho_2}}{\frac{Q_m}{\rho_1} + \frac{1}{\rho_2}} \tag{3.3}$$

where ρ_1 and ρ_2 was the density of the solvent and PEGDA respectively and Q_m was the mass swollen ratio. Equation 3.2 is a modified version of the Flory-Rehner model, described by Peppas and Merrill where polymerization occurred while in H_2O (Peppas and Merrill, 1977; Lin and Metters, 2006; Lin et al., 2011).

Conductivity was measured using a 4-point probe method, with electrodes placed 2 mm apart, on both dry and PBS-swollen polymers. Conductivity was recorded with a Keithley 2611 source meter combined with a custom Matlab script. Voltage measurements were taken until a stable reading was achieved and the average over 25 s was used in the following equation to calculate conductivity:

$$\sigma = \frac{I * \ln 2}{\pi * \Delta V * t} \tag{3.4}$$

where σ is the apparent conductivity, I is the current applied between the first and fourth electrodes, ΔV is the recorded voltage drop between the second and third electrodes and t is thickness. It should be noted that a correction divisor to account for thickness was incorporated into this calculation, defined by Blythe (1984), due to the polymers having significantly different thicknesses depending on the PPy concentration used. Results are reported alongside the standard error (SE), n=3 unless otherwise stated.

3.3 Results

3.3.1 Nanoparticle Creation and Characterization

PPy NP sizing was averaged over three polymerization reactions and showed a mean diameter of 72.5 $\pm$ 7.5 nm and a polydispersity of 0.122 $\pm$ 0.038. The size distribution data of each run was collected from the Zeta software which uses a Non-Negatively constrained Least Squares algorithm to fit the data, seen in panel (a) of Figure 3.1. The three runs of n = 1, 2 and 3 had an average particle diameter of 70.5, 86.4

and 60.7 nm respectively. SEM, seen in panels (b) and (c) of Figure 3.1, show the creation of NP through the polymerization process. Both panels (b) and (c) showed spherical PPy NPs with some irregularities and a rough surface topography. The diameter measurements in panel (c) showed a range of diameters between 39.4 to 157 nm, averaging 73.8 ± 11.2 nm.

3.3.2 PPy/PEGDA Resin Creation and Characterization

The absorbance plots in Figure 3.2 showed the peaks of riboflavin at 370 nm and 444 nm compared to a commercially available photoinitiator, Irgacure 2959, with a single peak at 276 nm. The Irgacure 2959 photoinitiator was shown to be ineffective at the wavelength of the OMASML printer whereas riboflavin had a relatively high absorbance. The UV absorption from each TEA ratio resin, seen in Figure 3.3, showed variable peak absorbances. The specific peaks of each curve were in the same locations, fitting the Riboflavin UV absorption curve seen in Figure 3.2. It was observed that three ratios of 28:1, 20:1 and 12:1, were grouped together and had increased absorption compared to the three other resins. The largest (36:1) and smallest (4:1, 3.2:1) TEA ratio resins yielded the lowest absorption values at all wavelengths. At 385 nm, the 20:1 and 12:1 samples showed the highest absorption.

After characterization of the PEGDA resin by itself, PPy NPs were added. The UV absorbance of each PPy concentration resin, outlined in Figure 3.4, was collected and showed the impact of the black PPy NPs. With each increase in the concentration of PPy NPs, the UV absorption of the diluted resin was also increased. The 0 PPy resin served as a baseline with no interference from the PPy NPs, highlighting the same riboflavin peaks seen in Figure 3.2 and Figure 3.3. The specific peak at 370 nm was less distinct in the samples with larger concentrations of PPy, with a total loss of the absorbance peak seen with the 0.75 PPy resin.

PPy/PEGDA resins were cured for variable lengths of time with the Prusa SL1 due to

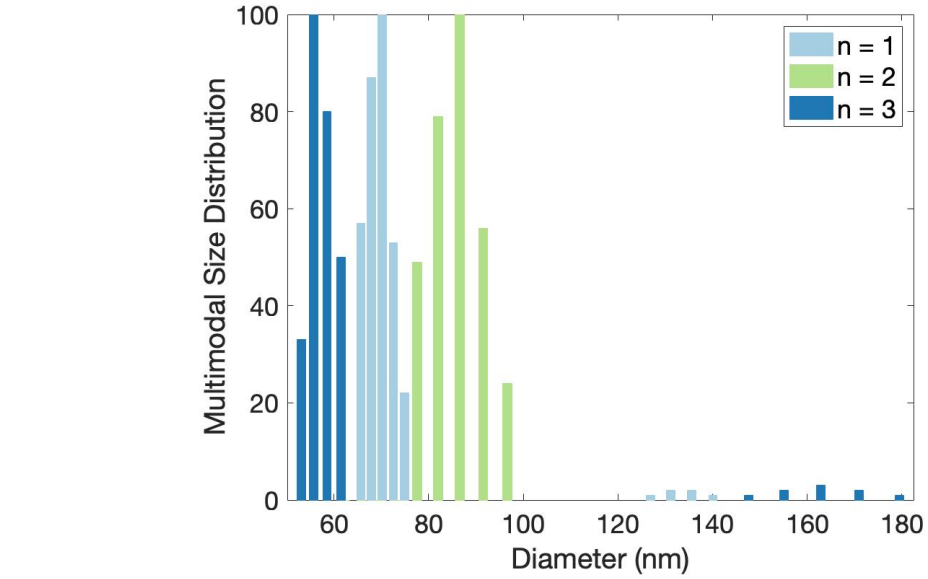

(a)

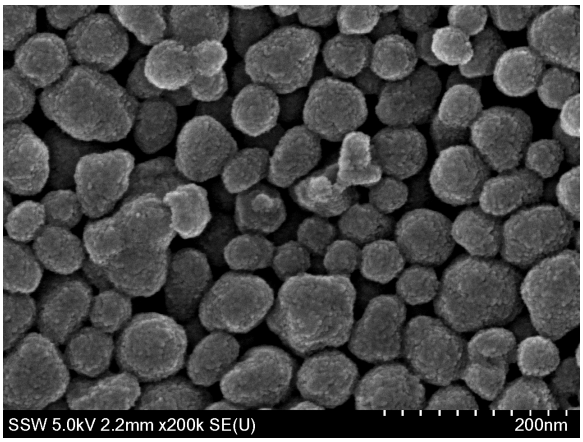

(b)

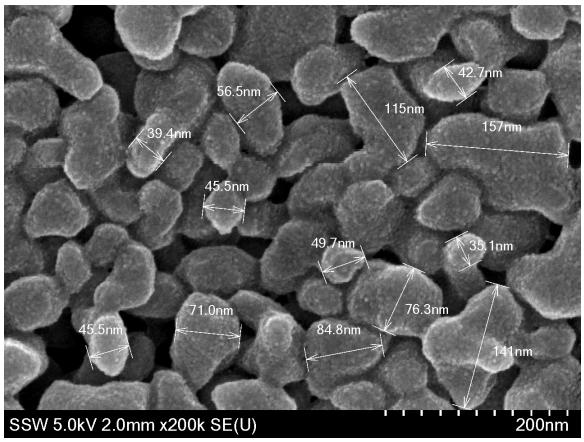

(c)

Figure 3.1: Polypyrrole (PPy) nanoparticle sizing and morphology results: (a) size distribution of three separate creation trials showing the variance in average diameter between trials, (b) SEM images of the nanoparticles and (c) measured SEM images outlining the size distribution seen in panel (a).

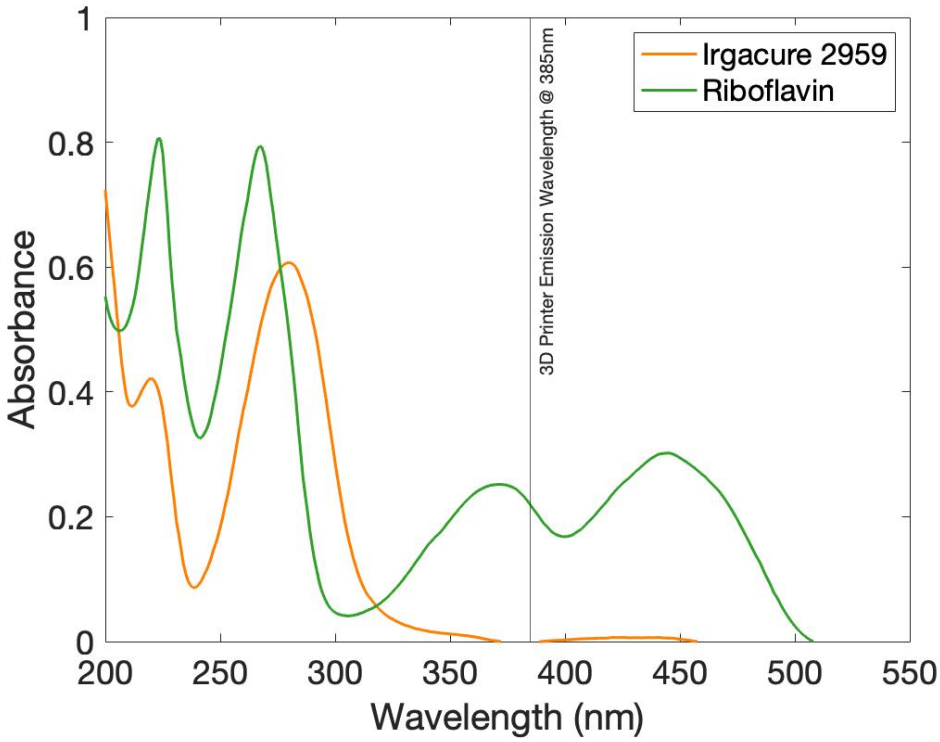

Figure 3.2: The UV absorption spectrums for 0.01 mg/ml Irgacure 2959 and 0.11 mg/ml riboflavin in H_2O, showing the riboflavin peaks are very close to the emission wavelength of the OMASML printer whereas Irgacure 2959 peaks occur at 270 nm and is barely excited at the printer emission wavelength, ruling it out of this application.

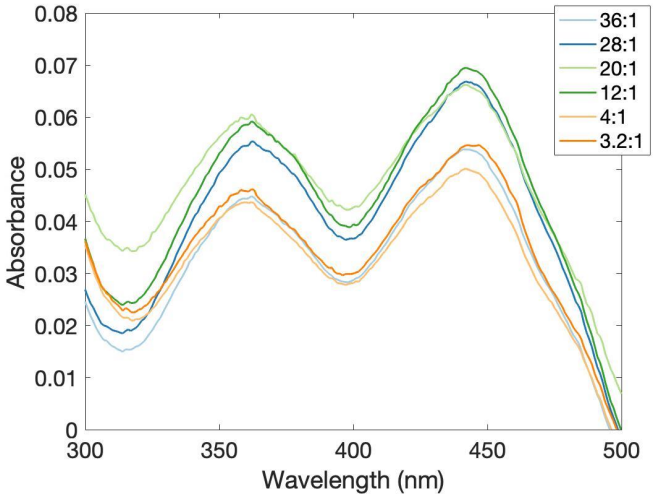

Figure 3.3: UV absorption of diluted poly(ethylene) glycol diacrylate (PEGDA) and triethanolamine (TEA) and riboflavin resins with the following ratios (PEGDA:TEA): 36:1, 28:1, 20:1, 12:1, 4:1 and 3.2:1, based off research from Nguyen et al. (2013) and Cristovão et al. (2019).

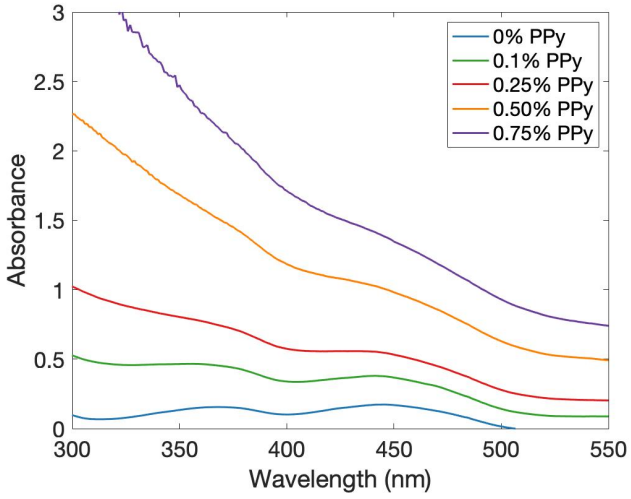

Figure 3.4: UV absorption of diluted poly(ethylene) glycol, riboflavin, triethanolamine and polypyrrole (PPy) nanoparticle (NP) suspension (0, 0.1, 0.25, 0.5 and 0.75 wt%) resins. The absorption increases as the black PPy NPs are added, as they decrease the amount of light able to pass through the samples. The loss of the 370 nm riboflavin peak was observed in the 0.75 PPy sample.

(a) (b) (c) (d) (e)

Figure 3.5: Cast polypyrrole (PPy) and poly(ethylene) glycol diacrylate resins, created with (a) 0, (b) 0.1, (c) 0.25, (d) 0.5 and (e) 0.75 wt% PPy H_2O suspensions cured for 30, 40, 50, 60 and 60 min, respectively, showing the dramatic change in colour and surface roughness that the particles had on the final hydrogel composition.

the higher UV absorbance seen in Figure 3.4, yielding the polymers seen in Figure 3.5. The 0, 0.1, 0.25, 0.5 and 0.75 PPy polymers were cured for 30, 40, 50, 60 and 60 min respectively, to ensure that there was solidification throughout the entire depth of the polymer. Panel (a) shows the colour of the print due to the yellow-riboflavin molecule. Both the 0 and 0.1 PPy polymers were still semi-transparent after curing whereas the 0.25, 0.5 and 0.75 PPy polymers were deep black. The 0.75 PPy polymer was cured for 60 min and only a thin film was cured, seen in Panel (e), highlighting the inefficiency of the photoinitiation system with added PPy NPs.

Results from the PPy/PEGDA polymer swelling ratio and M_c calculations showed that the incorporation of PPy NPs into the hydrogel modified the PEGDA crosslinking. Figure 3.6 showed that with each increase in PPy NP concentration, there was an observed decrease in swelling ratio. The 0.75 PPy sample showed the lowest swelling ratio of 0.18 ± 0.03. The 0.1, 0.25 and 0.5 PPy polymers showed a swelling ratio of 0.92 ± 0.08, 0.63 ± 0.08 and 0.73 ± 0.07. Only the 0 PPy sample showed a swelling ratio larger than one, with a ratio of 1.37 ± 0.12. Using Equation 3.2 and Equation 3.3, the average molecular weights between chains were calculated. The 0, 0.1, 0.25 and 0.5 PPy samples all showed similar results, having M_c values of 546 ± 16, 630 ± 22, 747 ± 40 and 699 ± 30 g/mol respectively. The 0.75 PPy sample had a very high M_c value of 1400 ± 123 g/mol.

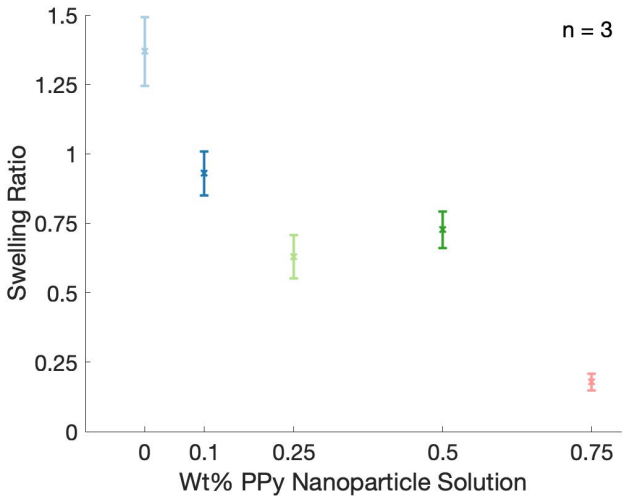

Figure 3.6: Swelling ratio of the polypyrrole (PPy) and poly(ethylene) glycol diacrylate resins, showing the impact of the addition of PPy nanoparticles on the matrix.

Conductivity measurements of both the dry and PBS-swollen PPy/PEGDA polymers were outlined in Figure 3.7. The conductivity of the dried polymers showed that there was a large increase in conductivity for all PPy hydrogels compared to the PEGDA hydrogel alone, which had a conductivity of $(2.2 \pm 0.03) \times 10^{-8}$ S/cm. The 0.1, 0.25 and 0.5 PPy polymers yielded conductivity values of $(1.6 \pm 0.13) \times 10^{-7}$, $(1.5 \pm 0.13) \times 10^{-7}$ and $(2.5 \pm 0.28) \times 10^{-7}$ S/cm respectively, showing a 6.8 to 10$\times$ increase in conductivity compared to PEGDA alone. The 0.75 PPy polymers yielded the highest conductivity of $(5.6 \pm 0.97) \times 10^{-7}$ S/cm, a 25-fold increase compared to 0 PPy polymers. ANOVA testing showed that there was a significant difference ($p < 0.05$) between all samples and the 0.75 PPy polymer. The PBS swollen samples all yielded higher conductivity values compared to the dry samples, shown in Figure 3.7 panel (b). The 0 PPy polymer yielded a conductivity value of 2.1 ± 0.4 mS/cm. Interesting, 0.1 PPy polymer showed the lowest conductivity of 1.2 ± 0.2 mS/cm. The 0.25 and 0.5 PPy samples gave conductivity values of 2.5 ± 0.2 and 2.1 ± 0.1 mS/cm respectively. Finally, the 0.75 PPy sample showed the highest conductivity of 3.5 ± 1.0 mS/cm. ANOVA testing with a p values of 0.05 showed a significant difference in conductivity between the 0.1 and 0.75

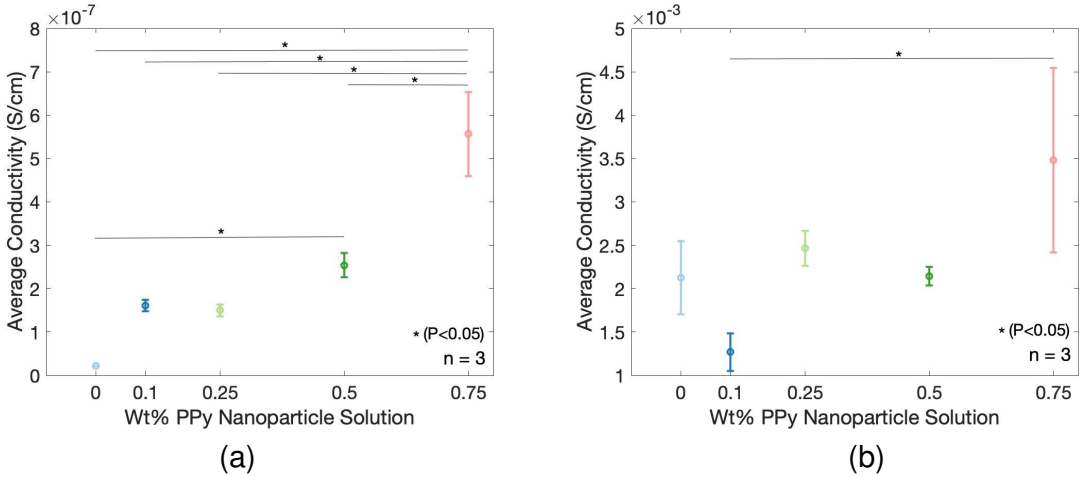

Figure 3.7: Conductivity measurements of polypyrrole (PPy) and poly(ethylene) glycol diacrylate resins when (a) dry and (b) swollen in phosphate buffered saline, showing increase in conductivity due to the addition of conductive PPy nanoparticles.

PPy samples (p = 0.013).

3.4 Discussion

3.4.1 Nanoparticle Creation and Characterization

NPs were created using oxidative chemical synthesis, outlined in Figure 3.8. The process used SDS to suspend micelles of pyrrole monomers in an acidic medium. This type of pyrrole polymerization method has been previously described by Samanta et al. (2015) and Leonavicius et al. (2011) and was chosen as it avoids the use of harsh oxidization conditions or oxidizing agents. This polymerization method avoids the use of $FeCl_3$, K_2Cr_2O and $KMnO_4$ etc. which are strong oxidizing agents that have the potential of being incorporated into PPy NPs and cause downstream effects, such as cytotoxicity (Leonavicius et al., 2011). As these NPs were used in biomedical applications, a H_2O_2 polymerization process was implemented. The success of polymerization was first visualized by the colour change of the solution, demonstrated in Figure 4.4. The mixture

started as a cloudy white pyrrole suspension just before adding H_2O_2 and immediately darkened after the addition of H_2O_2. After 24 h, the solution was completely black, indicating the complete polymerization of pyrrole. Leonavicius et al. (2011) described the micelle size of $20 - 30$ nm which correlated to the 30 nm diameter particles created. The average diameter of the particles created in this thesis was 72.5 ± 7.5 nm, slightly larger compared to Leonavicius et al. (2011). The SEM images seen in Figure 3.1 validated the ZETA measurements and showed that some micelles were able to achieve the $40 - 50$ nm range. Samanta et al. (2015) created PPy NPs with 34, 43 and 28 nm diameter with fluorescein, Piroxicam and rhodamine-6G incorporated into the polymerization solution. The larger diameter particles in this study are most likely due to the $10\times$ increase in PPy and H_2O_2 volumes compared to Samanta et al. (2015) during polymerization, creating larger pyrrole micelles. The $10\times$ volume increase allowed for increasingly concentrated NP solutions to be created, used in the PPy/PEGDA resins. Additionally, Leonavicius et al. (2011) used a rotational speed of 2,500 $r/min$with unspecified equipment sizes (beaker and stir bar) whereas this study was limited by the equipment available which had a maximum of 1,200 r/min, these changes may affect emulsification conditions and micelle size. Referencing other types of oxidants, the H_2O_2 polymerization method yielded comparable NPs. For example, Wen et al. (2017) used $FeCl_3$ to create PPy NPs 86.8 nm in diameter. Kwon et al. (2008) also used $FeCl_3$ with various surfactants to create cubed PPy NPs with diameters between $60 - 100$ nm. The results of this study showed the success of creating PPy NPs that could then be used for biomedical applications, although yielding a larger diameter than Samanta et al. (2015) and Leonavicius et al. (2011), the particles were still on the nano-scale. The large variance between n-values, seen in Figure 3.1, is hypothesized to be from minor differences in the creation process that could not be accounted for, such as minor differences in speed of H_2O_2 addition and vortex quality, that could affect the particle diameter by changing the micelle size. Overall, this method successfully created PPy

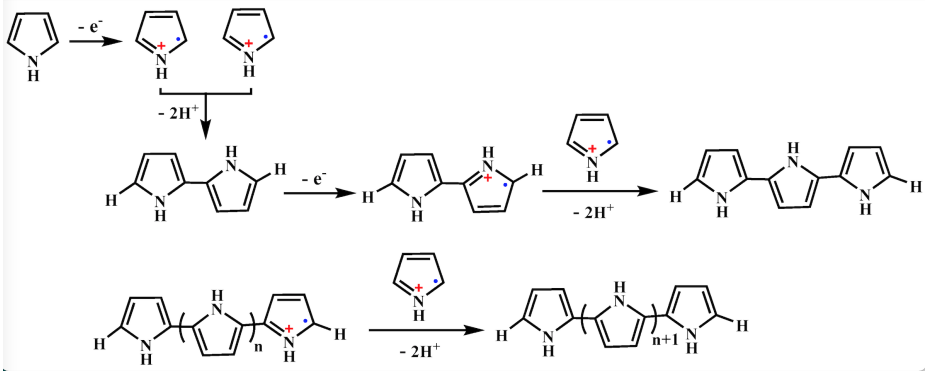

Figure 3.8: Diagram outlining the oxidative polymerization process of PPy (© Wang (2016), included with permission).

NPs that could then be incorporated into PEGDA resins.

3.4.2 PPy/PEGDA Resin Creation and Characterization

Figure 3.2 demonstrated the UV absorbance of riboflavin and Irgacure 2959. Irgacure 2959 is semi-biocompatible, commercially available photoinitiator that is commonly used due to its efficiency (Williams et al., 2005). Although said to be biocompatible, at larger concentrations or with certain cell lines Irgacure 2959 has been deemed to be cytotoxic (Williams et al., 2005). Additionally, the absorption curve shows that significant excitation doesn't occur above 365 nm, making it an ineffective photoinitiator for the OMASML printer. The UV absorbance of riboflavin showed the molecule is excited at 385 nm light emitted by the OMASML printer, making it an optimal biocompatible choice. Riboflavin has previously been used as a photoinitiator, Orellana et al. (1999) first investigated its use in conjunction with TEA to polymerize vinyl. Referencing pertinent literature on riboflavin and TEA photoinitiation, two studies using riboflavin/TEA for the polymerization of PEGDA were chosen to base the TEA concentration tests on. Cristovão et al. (2019) used this polymerization method with extrusion based 3D printing with a PEGDA:TEA ratio of 3.2:1 and Nguyen et al. (2013) used a 36:1 PEGDA:TEA ratio with two-photon 3D printing using high-powered lasers. From this

literature, a range of PEGDA:TEA ratios were chosen to optimize the concentration for the OMASML printer. A linear trend in absorbance was expected as the amount of TEA was increased. Surprisingly, it was shown that the 12:1, 20:1 and 28:1 ratios had the highest UV absorbance values compared to the 3.2:1, 4:1 and 36:1 ratios. Orellana et al. (1999) outlined that amine concentration to create active radicals was not linear. The graphs of both *Polymerization Rate* and *Active Radical Yield vs. TEA Concentration* showed a sharp increase in Polymerization Rate and Active Radical Yield with TEA concentration until peaking at 0.01 mol/l, then slowly decreasing. Although this study used HEMA/water at a (1:2) (v/v) ratio at pH 9, the same trend of TEA concentration was seen. It was noted that during the curing process for the TEA resins, the higher ratios of PEGDA:TEA were quickly photo-bleached, leading to a clear polymer. This observation was important as the incorporation of NPs severely inhibited riboflavin excitation (discussed below), leading to a smaller ratio of PEGDA:TEA being chosen. The final PEGDA:TEA ratio was chosen to be 12:1, which contained a significant concentration of TEA to keep riboflavin excited without photobleaching.

The addition of PPy NPs was shown to greatly affect the PEGDA matrix that was formed. Figure 3.4 showed that the UV absorbance of the resins increased with the larger concentrations of PPy NP. This is due to the black PPy NPs absorbing an increasing amount of UV light and blocking the riboflavin molecules from becoming excited. Although it has been shown that the absorbance of PPy NPs is low between 300–600 nm and some visible light can pass through, Figure 3.4 showed a concentration dependent absorbance (Chen et al., 2015). These absorption results fit with the polymer-cure times that were used to create Figure 3.5. With each addition of PPy, a longer cure time was required to solidify the mixture, again showing that an increased amount of light was being absorbed by the PPy NPs. The 0.75 PPy resin was cured for the longest and the polymer created was incredibly thin, showing that 0.5 PPy was the maximum PPy concentration that could be incorporated into the resin. Other research incorporating

NPs showed various impacts on the hydrogel creation and properties. Ma et al. (2019) created poly-l-lactide scaffolds with 0.5% (w/v) PPy particles but avoided the issues with curing by implementing an extrusion based 3D printing method. Lee et al. (2018) used similar stereolithography methods to print PEGDA resin with 0.02–0.1% (w/v) black carbon nanotubes but did not discuss curing issues with larger concentrations. Interestingly, Fantino et al. (2018) avoided the use of NPs by implementing a two-step polymerization process where PEGDA was first created with stereolithography and a subsequent interfacial polymerization method deposited PPy on the surface on the hydrogel. Looking into the hydrogel matrix properties, it was seen that the addition of PPy NPs impacted the hydrogel quality. Swelling ratio studies showed that the addition of PPy NPs lowered the water absorption. Swelling ratio is defined as water absorptivity of the polymer and can be modified through the crosslinking density. Polymers with closer crosslinks are able to expand less. This has been seen with higher molecular weight PEGs having larger mesh sizes and swelling ratios compared to PEG with lower molecular weights (Park et al., 2009). The results from the addition of the PPy NPs into PEGDA resin show the opposite phenomenon, smaller swelling ratios as the PPy concentration was increased. It was hypothesized that the addition of PPy would allow larger spaces between crosslinks, therefore increasing the swelling ratio. The average molecular weight between PEGDA crosslinks was calculated to examine the degree of crosslinking for each PPy concentration. Results from this study showed that the 0.75 PPy resin had a M_c twice the Mn value of PEGDA (700 Mn), whereas the 0–0.5 PPy resin showed an average M_c value between 546–747(g/mol). The high M_c value and low swelling ratio of the 0.75 PPy polymer was hypothesized to be from excess unreacted monomers that were not able to polymerize due to PPy NPs blocking the riboflavin excitation. Looking at literature with hydrogel swelling and NPs, Sajesh et al. (2013) described lower swelling ratios due to the addition of PPy-alginate into chitosan polymers, stating that the PPy in that application was hydrophobic. A contact angle study

of the PPy NPs created in this study could determine their interaction on the swelling ratio. Chang et al. (2010) also saw a reduced swelling ratio with larger concentrations of Laponite NPs in PEGDA hydrogels, attributing the decease to the interaction of Laponite and PEG causing a higher cross-linking density. Further testing is needed to elucidate the relationship between swelling ratio and PPy NP concentration. Overall, this study showed that the maximum concentration of PPy NP solution that can be added into a 1:1 PEGDA:H_2O resin was 0.5 wt.% before the addition severely affects the matrix properties.

Finally, the conductivity of the scaffolds was collected as the incorporation of PPy NPs was hypothesized to improve the electrical properties of the PEGDA hydrogels. The conductivity of these scaffolds is important because bone has the capability to respond to external electrical stimuli for improved healing (Sajesh et al., 2013; Wiesmann et al., 2001). Additionally, osteoblast differentiation has been shown to increase in the presence of electrical stimuli (Liu et al., 2013). This means that conductive PPy/PEGDA bone scaffolds could be electrically modulated after implantation to increase healing. The 4-point probe method implemented allowed the conductivity to be measured without a dependency on the contact area (Blythe and Bloor, 2008). The addition of PPy NPs showed a large increase in the conductivity values when the polymers were dry and swollen in PBS. The PBS samples had the compounding effect of ionic conductivity from the ions present in solution, but allowed a physiologically relevant testing environment. The 0.25 and 0.75 PPy PBS-swollen samples yielded conductivity measurements higher than bone marrow (0.23 S/m), where the 0 and 0.5 PPy samples were just under this target (Balmer et al., 2018). All PBS-swollen polymers showed a higher conductivity compared to cortical bone (9.1 mS/m) (Balmer et al., 2018). Comparing these polymers to other conducting hydrogels, Guarino et al. (2013) used a polyaniline/PEGDA polymer and were able to achieve conductivity values of $(1.1 \pm 0.2) \times 10^{-8}$ and $(1.1 \pm 0.5) \times 10^{-6}$ S/cm for 1:99 and 3:97 PANI:PEGDA ratios,

showing that the polymers in our study had higher conductivity values with smaller concentrations of CP. Liang et al. (2018) used hyperbranched poly(amino ester)-pyrrole with gelatin that was capable of *in-situ* polymerization that gave a maximum conductivity of $(6.51 \pm 0.12) \times 10^{-4}$ S/cm. This application used Fe^{+3} to polymerize pyrrole and were not limited by the UV-absorbance described above. The conductivity measurements showed that these scaffolds can be applied in future studies in osteogenic healing applications.

3.5 Chapter summary

This chapter has outlined the creation and characterization methodologies used to develop a PPy/PEGDA resin. First, PPy NPs were created using oxidative polymerization methods and subsequently characterized according to size and morphology. The investigation into a non-cytotoxic photoinitation system for PEGDA led to the use of riboflavin and TEA. Combining PPy NPs and photoactive PEGDA created a composite hydrogel that was characterized through UV-absorbance, swelling-ratio and conductivity. These tests have shown the success of creating a conductive photoactive resin that can applied to varied applications, outlined in Chapter 4: *PPy/PEGDA Composite Resin Application*.

List of references

Balmer, T. W., Vesztergom, S., Broekmann, P., Stahel, A. and Büchler, P. (2018), 'Characterization of the electrical conductivity of bone and its correlation to osseous structure', *Scientific Reports* **8**(1), 8601.

Blythe, A. (1984), 'Electrical resistivity measurements of polymer materials', *Polymer Testing* **4**(2), 195–209. Measurement Techniques for Polymeric Solids.

Blythe, T. and Bloor, D. (2008), *Electrical Properties of Polymers*, Cambridge University Press.

Chang, C.-W., van Spreeuwel, A., Zhang, C. and Varghese, S. (2010), 'PEG/clay nanocomposite hydrogel: a mechanically robust tissue engineering scaffold', *Soft Matter* **6**(20), 5157.

Chen, X., Yu, N., Zhang, L., Liu, Z., Wang, Z. and Chen, Z. (2015), 'Synthesis of polypyrrole nanoparticles for constructing full-polymer uv/nir-shielding film', *RSC Adv.* **5**, 96888–96895.

Cristovão, A. F., Sousa, D., Silvestre, F., Ropio, I., Gaspar, A., Henriques, C., Velhinho, A., Baptista, A. C., Faustino, M. and Ferreira, I. (2019), 'Customized tracheal design using 3D printing of a polymer hydrogel: influence of UV laser cross-linking on mechanical properties', *3D Printing in Medicine* **5**(1), 12.

Fantino, E., Roppolo, I., Zhang, D., Xiao, J., Chiappone, A., Castellino, M., Guo, Q., Pirri, C. F. and Yang, J. (2018), '3D Printing/Interfacial Polymerization Coupling for the Fabrication of Conductive Hydrogel', *Macromolecular Materials and Engineering* **303**(4), 1700356.

Guarino, V., Alvarez-Perez, M. A., Borriello, A., Napolitano, T. and Ambrosio, L. (2013), 'Conductive PANi/PEGDA Macroporous Hydrogels For Nerve Regeneration', *Advanced Healthcare Materials* **2**(1), 218–227.

Kwon, W. J., Suh, D. H., Chin, B. D. and Yu, J.-W. (2008), 'Preparation of polypyrrole nanoparticles in mixed surfactants system', *Journal of Applied Polymer Science* **110**(3), 1324–1329.

Lee, S.-J., Zhu, W., Nowicki, M., Lee, G., Heo, D. N., Kim, J., Zuo, Y. Y. and Zhang, L. G. (2018), '3d printing nano conductive multi-walled carbon nanotube scaffolds for nerve regeneration', *Journal of Neural Engineering* **15**(1), 016018.

Leonavicius, K., Ramanaviciene, A. and Ramanavicius, A. (2011), 'Polymerization Model for Hydrogen Peroxide Initiated Synthesis of Polypyrrole Nanoparticles', *Langmuir* **27**(17), 10970–10976.

Liang, S., Zhang, Y., Wang, H., Xu, Z., Chen, J., Bao, R., Tan, B., Cui, Y., Fan, G., Wang, W., Wang, W. and Liu, W. (2018), 'Paintable and rapidly bondable conductive hydrogels as therapeutic cardiac patches', *Advanced Materials* **30**(23), 1704235.

Lin, C.-C. and Metters, A. T. (2006), 'Hydrogels in controlled release formulations: Network design and mathematical modeling', *Advanced Drug Delivery Reviews* **58**(12), 1379–1408. Computational Drug Delivery.

Lin, S., Sangaj, N., Razafiarison, T., Zhang, C. and Varghese, S. (2011), 'Influence of physical properties of biomaterials on cellular behavior.', *Pharm Res* **28**(6), 1422–1430.

Liu, L., Li, P., Zhou, G., Wang, M., Jia, X., Liu, M., Niu, X., Song, W., Liu, H. and Fan, Y. (2013), 'Increased proliferation and differentiation of pre-osteoblasts MC3t3-e1 cells on nanostructured polypyrrole membrane under combined electrical and mechanical stimulation', *Journal of Biomedical Nanotechnology* **9**(9), 1532–1539.

Ma, C., Jiang, L., Wang, Y., Gang, F., Xu, N., Li, T., Liu, Z., Chi, Y., Wang, X., Zhao, L., Feng, Q. and Sun, X. (2019), '3D Printing of Conductive Tissue Engineering Scaffolds Containing Polypyrrole Nanoparticles with Different Morphologies and Concentrations', *Materials* **12**(15), 2491.

Nguyen, A. K., Gittard, S. D., Koroleva, A., Schlie, S., Gaidukeviciute, A., Chichkov, B. N. and Narayan, R. J. (2013), 'Two-photon polymerization of polyethylene glycol diacrylate scaffolds with riboflavin and triethanolamine used as a water-soluble photoinitiator', *Regenerative Medicine* **8**(6), 725–738.

Orellana, B., Rufs, A. M., Encinas, M. V., Previtali, C. M. and Bertolotti, S. (1999), 'The Photoinitiation Mechanism of Vinyl Polymerization by Riboflavin/Triethanolamine in Aqueous Medium', *Macromolecules* **32**(20), 6570–6573.

Park, H., Guo, X., Temenoff, J. S., Tabata, Y., Caplan, A. I., Kasper, F. K. and Mikos, A. G. (2009), 'Effect of swelling ratio of injectable hydrogel composites on chondrogenic differentiation of encapsulated rabbit marrow mesenchymal stem cells in vitro.', *Biomacromolecules* **10**(3), 541–546.

Peppas, N. A. and Merrill, E. W. (1977), 'Crosslinked poly(vinyl alcohol) hydrogels as swollen elastic networks', *Journal of Applied Polymer Science* **21**(7), 1763–1770.

Sajesh, K., Jayakumar, R., Nair, S. V. and Chennazhi, K. (2013), 'Biocompatible conducting chitosan/polypyrrole–alginate composite scaffold for bone tissue engineering', *International Journal of Biological Macromolecules* **62**, 465 – 471.

Samanta, D., Meiser, J. L. and Zare, R. N. (2015), 'Polypyrrole nanoparticles for tunable, pH-sensitive and sustained drug release', *Nanoscale* **7**(21), 9497–9504.

Sigma-Aldrich (2021), '(-)-riboflavin product information'.

Unagolla, J. M. and Jayasuriya, A. C. (2020), 'Hydrogel-based 3d bioprinting: A comprehensive review on cell-laden hydrogels, bioink formulations, and future perspectives', *Applied Materials Today* **18**, 100479.

Wang, L.-X., Li, X.-G. and Yang, Y.-L. (2001), 'Preparation, properties and applications of polypyrroles', *Reactive and Functional Polymers* **47**(2), 125 – 139.

Wang, M. (2016), 'Emerging multifunctional NIR photothermal therapy systems based on polypyrrole nanoparticles', *Polymers* **8**(10), 373.

Wen, J., Tian, Y., Mei, Z., Wu, W. and Tian, Y. (2017), 'Synthesis of polypyrrole nanoparticles and their applications in electrically conductive adhesives for improving conductivity', *RSC Advances* **7**(84), 53219–53225.

Wiesmann, H.-P., Hartig, M., Stratmann, U., Meyer, U. and Joos, U. (2001), 'Electrical stimulation influences mineral formation of osteoblast-like cells in vitro', *Biochimica et Biophysica Acta (BBA) - Molecular Cell Research* **1538**(1), 28–37.

Williams, C. G., Malik, A. N., Kim, T. K., Manson, P. N. and Elisseeff, J. H. (2005), 'Variable cytocompatibility of six cell lines with photoinitiators used for polymerizing hydrogels and cell encapsulation', *Biomaterials* **26**(11), 1211–1218.

Chapter 4

PPy/PEGDA Composite Resin 3D Printing and Drug Delivery

This chapter covers the applications of the PPy/PEGDA resin described in Chapter 3: *PPy/PEGDA Composite Resin Creation*. The 3D printing capabilities of the resins were characterized to determine the minimum feature resolution to ensure it can achieve the pore sizes needed for osteogenesis. Additionally, the drug delivery capabilities of the PPy NPs encapsulated in PEGDA resin were evaluated over a biologically relevant pH range.

4.1 Introduction

Stereolithography printing technology, outlined in Chapter 2, allows the creation of highly customized 3D shapes that are optimal for patient customized biomedical devices. Previous studies have used extrusion based 3D printing with CP/hydrogel composites, but were limited by the nozzle size and rheological properties of the printing ink (Vijayavenkataraman et al., 2019; Li et al., 2018). Given the development of the photoactive PPy/PEGDA resin outlined in Chapter 3 and the advantages of stereolithography print-

ing, characterization of the PPy/PEGDA resin 3D printing capabilities was seen as the next step towards patient customized PPy/PEGDA devices. To our knowledge, no study has combined PPy/PEGDA into a resin for stereolithography printing. Testing was focused on the XY print resolution of the PPy/PEGDA resins, the minimum print diameter for both positive and negative features allowed the impact of the PPy NPs on the PEGDA print resolution to be characterized. The prints tested the stereolithography parameters for the customized OMASML printer to create complex microarchitectures that are needed for osteo-scaffolds for biomedical applications. The goal was to achieve the smallest features possible, as that would set the lower limit for porosity moving forward in research. Additional prints fabricated using 3D bone models obtained from micro-CT imaging allowed validation of real world osteogenic applications in which these implants could be used in place of traditional bone grafts. In addition to 3D printing, the drug delivery capabilities from the PPy NPs was investigated. Previous studies have shown that PPy is capable of dopant entrapment and release, outlined in Chapter 2. The drug-delivery tests helped elucidate the dopant entrapment and release characteristics from PPy NPs for their utilization in areas of bone regeneration. The goal of this section was to maximize dopant entrapment, while protecting drug function, and show the pH dependent release from NPs. Past literature tested pH-triggered dopant release from PPy NPs over large pH ranges, whereas this study narrowed the pH release values to a physiological range between 6 – 8 (Samanta et al., 2015). Both PPy NPs alone and PEGDA encapsulated NPs showed pH triggered release, favouring larger release in increasingly alkaline conditions. The experiments outlined below demonstrate both the 3D printing and drug delivery capabilities of the PPy/PEGDA resins.

4.2 Materials and Methods

4.2.1 Materials

Fluorescein (FL) (CAS #2321-07-5) and vancomycin (CAS #1404-90-6) were used as received. Three potassium phosphate monobasic/sodium hydroxide buffers of pH 6, 7 & 8 were mixed to create a pH range between 6–8 at 0.25 increments (CAS #SB104-500, #SB108-500, #SB112-500, respectively). Pyrrole, HCl, SDS, H_2O_2, PEGDA, riboflavin, TEA, IPA and PBS were all used as listed in Chapter 3.

4.2.2 Methods

To identify the effect of PPy NP concentration on feature resolution, four PPy/PEGDA resins (0, 0.1, 0.25 and 0.5 PPy) were created as outlined in Chapter 3. Resins were cured using the custom-designed OMASML digital light projection printer, outlined in Figure 4.1. The printer had an emission wavelength of 385 nm, an irradiation energy of 7.37 J/cm^2 and a theoretical minimum XY feature resolution of 5 μm. PPy/PEGDA resolution was measured using the patterns outlined in Figure 4.2, adapted from an open access online repository, Thingiverse (Thingiverse #2011862). To create the print, five layers of Figure 4.2 panel (a) was cured, followed by 5 layers of panel (b). All prints used a 25 μm layer thickness and a 5 s settling time. The cure time for the 0, 0.1, 0.25 and 0.5 PPy resins was selected to be 1.5, 20, 100 and 200 s/ layer based off previous printing results and the UV absorbance data in Chapter 3. Cured polymers were rinsed with IPA to remove any excess resin. Images were collected using a Keyence VHX-7000 digital microscope. To validate material functionality for bone grafts, two resins (0 PPy and 0.1 PPy) were selected to print a 50 layer micro-CT scan of trabecular bone, seen in Figure 4.3, with identical parameters as above. These two resins were selected because they had the shortest curing times, allowing rapid testing and evaluation of various

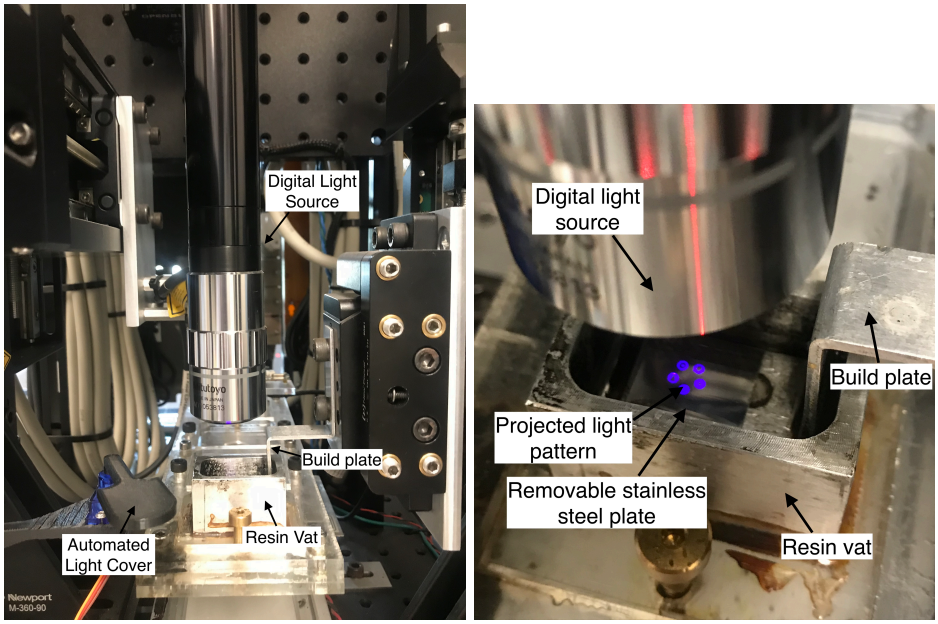

(a) (b)

Figure 4.1: Images of the custom designed stereolithography printer outlining (a) the general overview, labelled with the important components, and (b) the light pattern being projected on a layer of resin.

print parameters. The model was adapted from Thingiverse #3750517. Post-imaging measurements were completed using ImageJ.

For drug delivery testing, PPy particles were created following the methods described in Section 3.2.2 with minor changes to incorporate dopant molecules. To create FL-doped NPs, 30 mg of FL was added to the SDS and HCl mixture before pyrrole polymerization, seen in Figure 4.4. FL-doped NPs were washed for 5 d following the same procedure in Chapter 3 to wash away any unbound dopant molecules. To create vancomycin doped NPs, 2.5 ml of washed un-doped PPy NPs were mixed with an equal volume of 25 mg/ml vancomycin dissolved in distilled water. The solution was vortexed for 10 min to attach vancomycin molecules on the surface of PPy NPs. The mixture was placed into a 3K MWCO dialysis bag in 1 l of distilled water and left overnight to remove any unbound vancomycin. After 12 h, a 10 ml sample of the wash fluid and the wash liquid volume was collected to calculate drug loading.

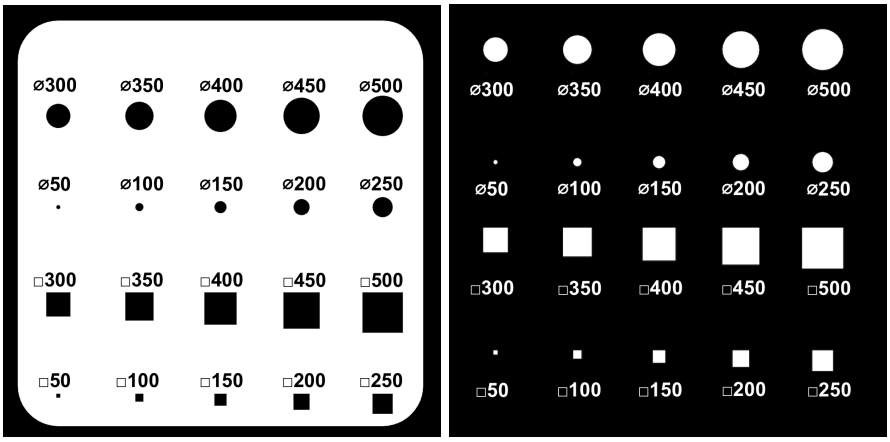

(a) (b)

Figure 4.2: The (a) hole and (b) pillar pattern to create the hole/pillar test print where everything shown in white is solidified. 5 layers of (a) were exposed followed by 5 layers of (b) which created a measurable print that defined the smallest feature resolution of various resin composition (All measurements in μm).

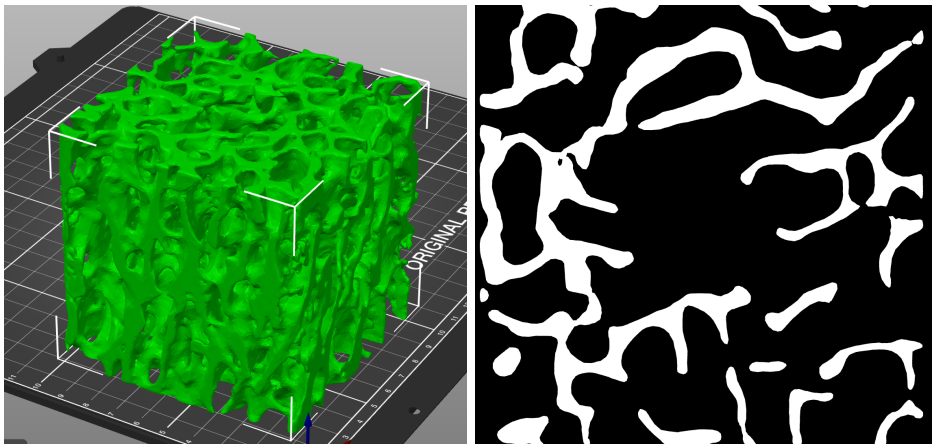

(a) (b)

Figure 4.3: (a) The CAD model created from Micro-CT data from trabecular bone with 30% bone volume/tissue volume and (b) an example of one of the 50 layers in the print pattern created from the CT model.

Two conditions were used to measure drug release from PPy NPs between pH 6–8 at 0.25 increments. PPy NPs alone and PEGDA encapsulated PPy NPs were tested for drug release. For NP release, 100 μl of doped-PPy NP solution was added to 3 ml of pH solution in triplicate and incubated at 37 °C. To create PEGDA encapsulated doped-NPs, the resin formula described in Chapter 3 was used along with the same casting method. The drug-doped PPy/PEGDA polymers were rinsed with IPA and subsequently placed into buffer solutions at 37 °C. FL-doped NP release was measured for over four time points: 2 h, 24 h, 7 d and 14 d. FL has a pH dependent absorbance value, showing a 50% decrease in absorption at 490 nm between pH 7.5 to 6.75, therefore the isosbestic value of 460 nm was selected to measure absorbance (Doughty, 2010). Vancomycin doped NP release was measured at 2 h and 24 h. The peak for vancomycin were seen at 281 nm and were used in conjunction with standard curves to calculate the dopant release values. A Cary 60 UV spectrometer was used to collect the absorbance data between 200 and 600 nm. Statistical analysis was completed using MATLAB. Results are reported with the standard error (n=3) unless otherwise stated. Two-way (analysis of variance) ANOVA was completed using a p value of 0.05.

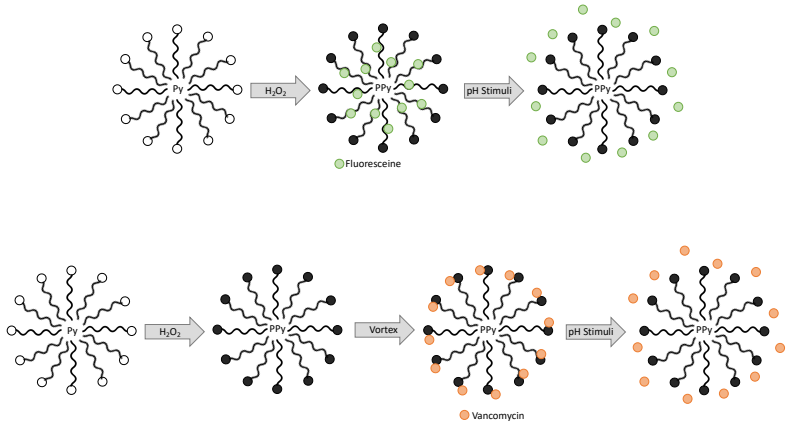

(a)

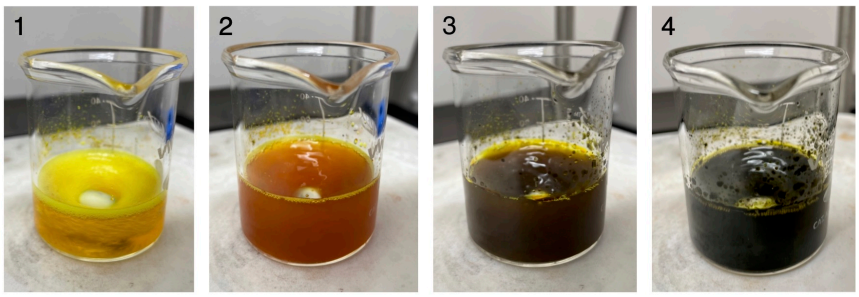

(b)

Figure 4.4: (a) Schematic of the polymerization of pyrrole micelles using hydrogen peroxide to initiate oxidative polymerization and (b) the colour change seen during pyrrole polymerization with incorporated fluorescein molecules at 1. before the addition of pyrrole, 2. immediately following the addition of pyrrole, 3. 1 h after adding hydrogen peroxide and 4. 24 h after the addition of hydrogen peroxide.

4.3 Results

4.3.1 3D Printing

Resolution testing of the PPy/PEGDA resins was visualized through the polymers created in Figure 4.5. The printing time of each resin was adjusted to allow for adequate curing and increased alongside PPy concentration, as described in Chapter 3: *PPy/PEGDA Composite Resin Creation*. The layer cure time was increased in 30 s intervals until solidification was seen. From this base, the print time was adjusted as needed based on the print quality, looking at feature resolution and layer adhesion. These tests were not seen as exhaustive as various print parameters such as cure time, settling time, layer thickness and depth between layers could impact the resolution, this study only focuses on layer print time. The minimum feature resolution measurements along with the pattern diameters are outlined in Table 4.1. Table 4.2 outlines the error between print pattern and the achieved print resolution, using a 150 μm pillar pattern and a 200 μm hole pattern. These diameters were chosen because they were the smallest diameter that all resins could achieve and could be compared. Overall, resins with larger concentrations of PPy showed smaller diameter features with smaller pillar resolution error and larger hole resolution error. The 0.5 PPy resin was able to achieve the smallest diameter pillars and holes. The 0.5 PPy resin also showed the least amount of over-cure, where excess resin is cured outside the given light pattern, outlined in Table 4.2 with the smallest pillar error. The 0 PPy resin showed the most over-cure, yielding the largest diameter pillar with the smallest print pattern and the largest pillar error, with +147 μm larger diameter seen compared to the pattern. Bone prints, seen in panel (e) and (f) of Figure 4.5, were successful in mimicking trabecular bone architecture. The 0 PPy resin was able to print a wall thickness of 30 μm and a pore diameter of 119 μm. The 0.1 PPy resin yielded a minimum wall thickness of 42 μm and a minimum pore diameter of 184 μm. Looking at the z-resolution, the theoretical total print height

	Pillar		Hole	
PPy	Achieved (μm)	Pattern (μm)	Achieved (μm)	Pattern (μm)
0	138	50	114	250
0.1	125	100	105	350
0.25	137	100	72	200
0.5	120	150	73	200

Table 4.1: Minimum achieved pillar and hole diameter for polypyrrole/poly(ethylene) glycol diacrylate resins, showing the smaller feature resolution possible due to the increase in concentration of NPs.

	Pillar		Hole	
PPy	Achieved (150 μm)	Error (μm)	Achieved (200 μm)	Error (μm)
0	297	+147	135	-65
0.1	192	+42	104	-96
0.25	188	+38	91	-109
0.5	120	-30	99	-101

Table 4.2: Achieved pillar and hole diameter for polypyrrole/poly(ethylene) glycol diacrylate resins using the 150 μm and 200 μm diameter pillar and hole patterns, respectively, showing the change in printing resolution errer due to the increase in concentration of NPs.

was 1250 μm and the 0 PPy and 0.1 PPy resins gave print heights of 1738 and 1555 μm respectively. The bone prints showed higher than expected total print heights, most likely due to the manual adjustment of the build plate during setup, which could lead to variances in the first layer thicknesses.

4.3.2 PPy Drug Delivery

Figure 4.4 outlines the process that occurred during PPy polymerization to create FL-doped NPs, visualized by the colour change moving from yellow to dark black due to the creation of PPy NPs. The UV absorption curve measurements seen in Figure 4.6 showed the peak of both dopant molecules. The FL molecule showed a peak at 488 μm and the vancomycin molecule showed a distinct peak at 281 nm. FL release between pH 6–8 at 0.25 increments was collected in triplicate over a 14 d period, shown in

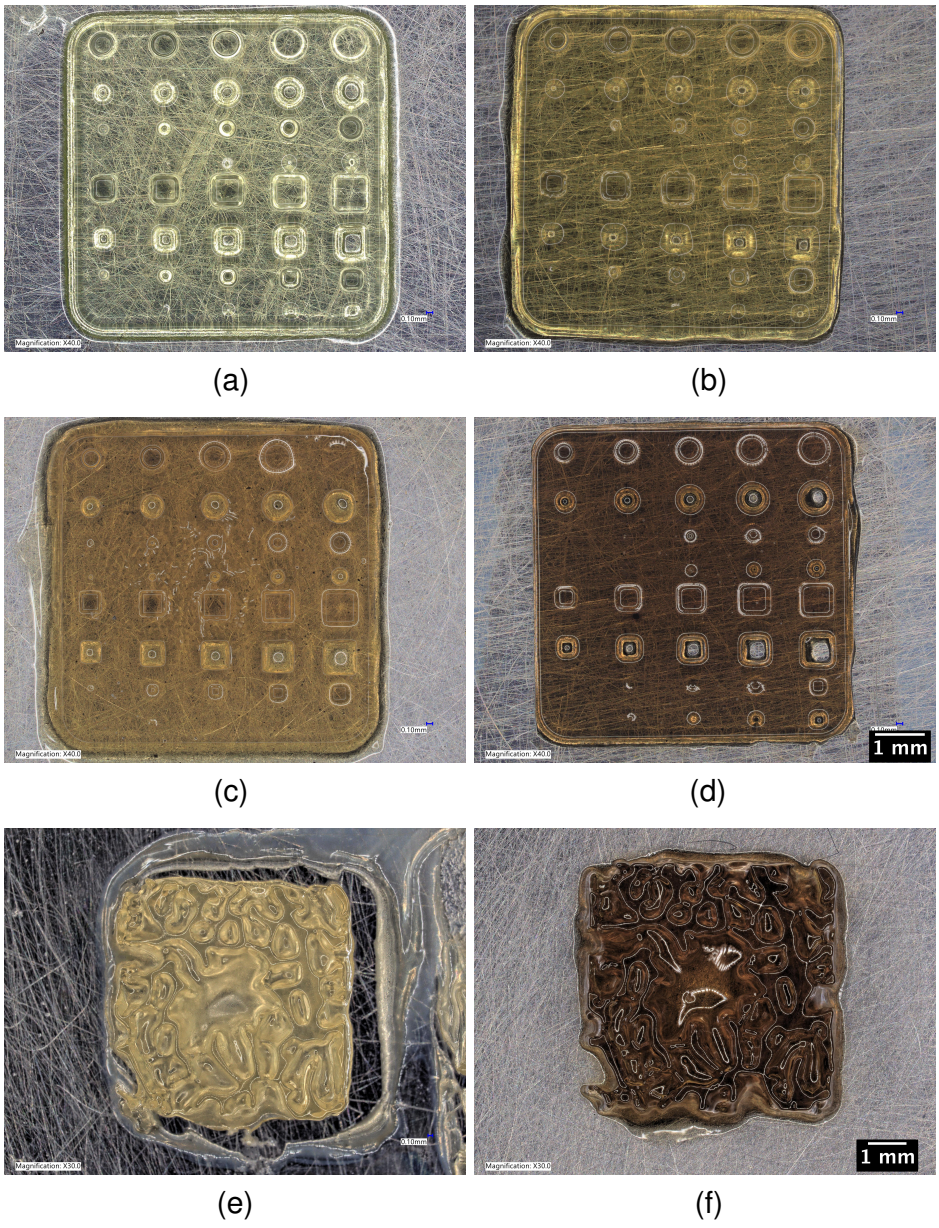

Figure 4.5: Pillar and hole print resolution tests with (a) 0 PPy, (b) 0.1 PPy, (c) 0.25 PPy, and (d) 0.5 PPy resins. Trabecular bone micro-CT prints using (e) 0 PPy and (f) 0.1 PPy resin, showing the applicability of PPy/PEGDA resins.

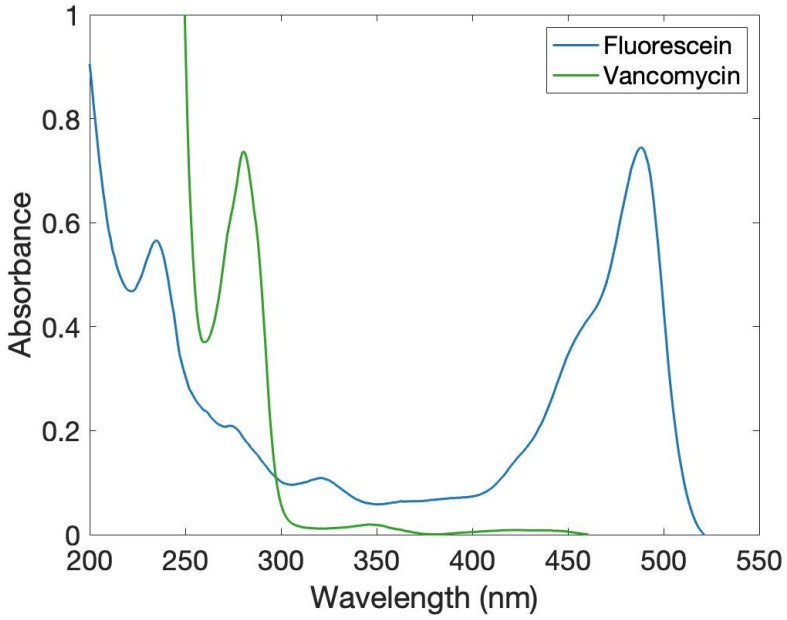

Figure 4.6: Absorption spectrums of both fluorescein (2.5 μg/ml) and vancomycin (0.125 mg/ml) molecules, showing their respective peaks at 488 and 281 nm that were used to detect drug release from the nanoparticles.

Figure 4.7. FL release was normalized by the mass of PPy NP used in each study. At all time points there was an increase in the average FL release at higher pH values, seen by the positive slope of all release graphs in panels (a) through (d). This qualitatively demonstrated the pH-dependent release that PPy is capable of. The 2 h release data showed overlapping averages when looking at the particle and resin FL release. This was contrasted against the 24 h, 7 d and 14 d experiments where the resin yielded higher averages values compared to the particles alone. The time dependent release from PPy NPs was visualized in panel (e) of Figure 4.7, highlighting three pH values: 6, 7 and 8. It can be seen that there was increased FL release for both the 7 d and 14 d time points compared to the shorter release times. Two-way ANOVA testing was completed measuring FL release between pH and release time for the NPs alone and resin encapsulated NPs. NP FL release was statistically significant for pH ($F=2.40$, $p=0.0234$) and for release time ($F=5.16$, $p=0.0028$). Specifically, there was a difference

in release between pH 8 and 6, 6.25 and 6.75. The resin encapsulated NPs showed no statistical differences in FL release by pH (F=0.42, p=0.9037) but the release was significant for release time (F=21.44, p=4.99×10^{-10}).

Vancomycin showed a less pronounced release trend over the tested pH values, seen in Figure 4.8. From the NP wash liquid, drug loading was calculated and taken as 100%. The vancomycin doped NPs were able to achieve an encapsulation efficiency of 16% from the solution that they were vortexed in. Vancomycin release from NPs alone was almost identical at both time points, yielding an average over all pH values of 50.7 ± 0.01 and 51.2 ± 0.02 % release for 2 and 24 h respectively. Slight decreases in the cumulative release between 2 h and 24 h are due to the filtering process at the 24 h timepoint where an added 1 ml of H_2O was added to pre-wet the filter, but was accounted for in the release calculations. In contrast, PEGDA encapsulated PPy NPs showed an average release of 30.2 ± 0.01 % over 2 h and 63.0 ± 0.03 % over 24 h, demonstrating the effect of encapsulating NPs into PEGDA. A two-way ANOVA was used and showed that NPs alone did not have a significant difference between the pH or release time and vancomycin release. PEGDA encapsulated vancomycin NPs showed a statistically different release in regards to pH (F=2.22, p=0.049) and release time (F=511.0, p=7.32×10^{-23}). This was specifically seen between pH 6.5 and 8, showing a large pH difference needed to trigger a significant increase in vancomycin release.

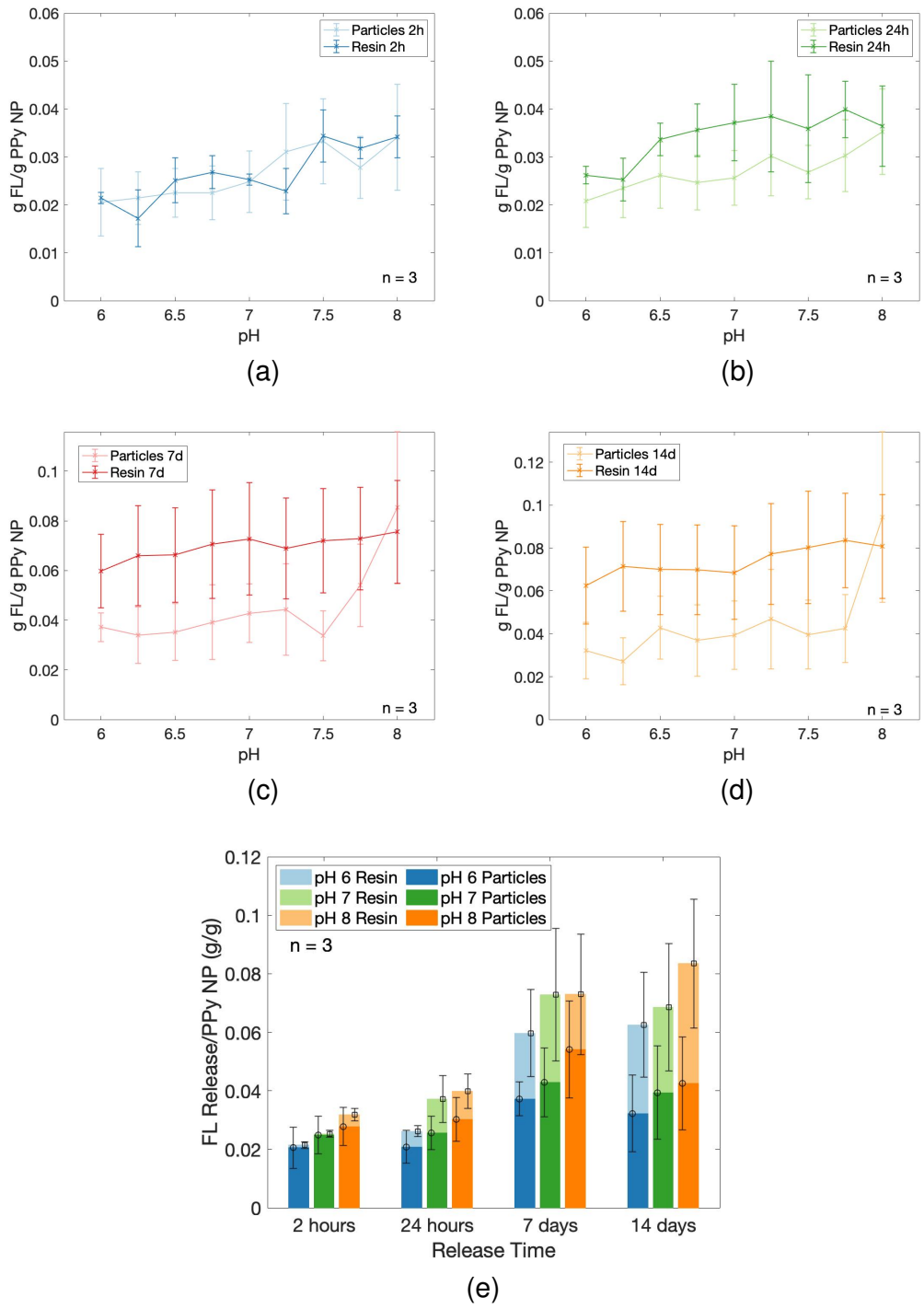

Figure 4.7: pH dependent release of fluorescein at 460 nm over (a) 2 h, (b) 24 h, (c) 7 d and (d) 14 d period from polypyrrole (PPy) nanoparticles (NP) in pH solution alone, shown in the darker shades, and poly(ethylene) glycol diacrylate resin encapsulated PPy NPs in pH solutions, shown in lighter shades. The time dependent release comparison (e) showing the extended release characteristics of the NPs alone and resin encapsulated NPs.

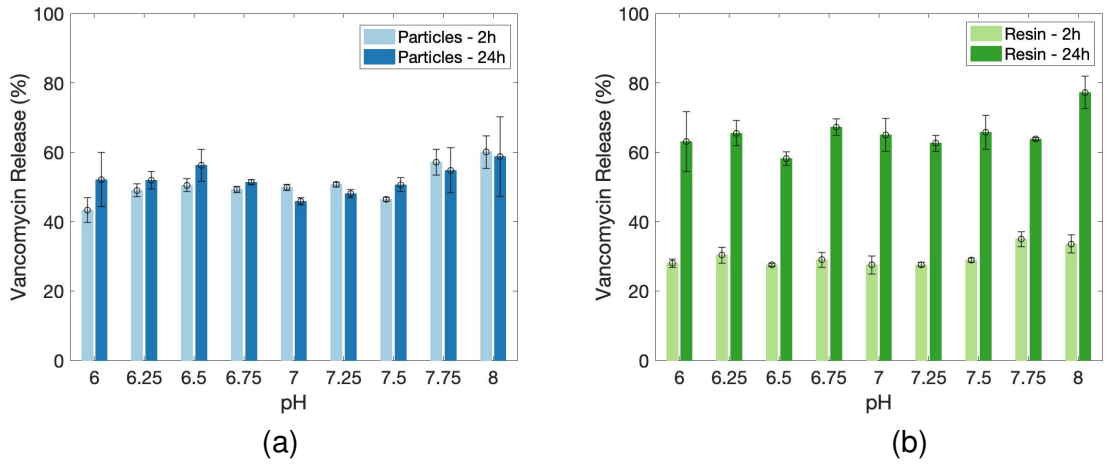

Figure 4.8: Vancomycin release from polypyrrole nanoparticles at 2 and 24 h for (a) nanoparticles alone and (b) nanoparticles encapsulated in resin.

4.4 Discussion

4.4.1 3D Printing

The results from the resolution testing were unexpected given the curing data analyzed in Chapter 3: *PPy/PEGDA Composite Resin Creation*. Layer print times were determined experimentally, based off the UV absorbance of the resin seen in Figure 3.4. Cure times were increased in 50 s intervals until a solid print was achieved and there was adequate layer adhesion. After successful curing, the print resolution was evaluated. It was hypothesized that the print resolution would decrease with the addition of NPs due to the lower curing efficiency. Conversely, the addition of NPs helped absorb any excess light. This was why the higher concentration PPy resins were able to better resolve hole patterns; excess light outside the pattern was being absorbed by the particles and wasn't able to cure resin. Over-curing was seen acutely with the 0 PPy sample because light was easily spread throughout the polymer, outside the given pattern. The over-curing in the 0 PPy sample helped build up larger-diameter pillars with excess cured polymer from the smallest diameter print pattern. Further optimization is needed

to fully test a range of printing parameters such as layer cure time, settling time and layer thickness, that may allow the creation of even smaller features to be resolved. Overall, the decease in print resolution can be accounted for in the print parameters and a larger number of PPy NPs for drug delivery, therefore the 0.5 PPy resin was said to be the most successful. Comparing these results against other types of 3D printing, Nguyen et al. (2013) used two-photon printing methods to cure PEGDA with riboflavin as a photoinitiator. Two-photon printing uses two ultra-short laser pulses to trigger polymerization at the intersection. Nguyen et al. (2013) was able to create 120 μm diameter hollow cylinders with a wall thickness of 20 μm, much smaller than the results outlined above. This type of two-photon method of polymerization is known to have high resolution, but rely on the light path being able to penetrate into the resin. The stereolithography methods used in this thesis create thin layers of resin where light only has to penetrate down 25 μm/layer. Therefore, two-photon curing methods described by Nguyen et al. (2013) may not be suitable with the dark PPy/PEGDA resins described in this thesis. Fantino et al. (2018) also used stereolithography printing of PEGDA and H_2O (40, 60, and 70% (w/w)) and was able to reliably yield 200 μm details. The printer used by this author had a XY resolution of 39 μm compared to the printer used in this thesis with a XY resolution of 5 μm. Therefore, it is reasonable that the results in this thesis yielded smaller diameter features but are still limited by the properties of PEGDA, H_2O and riboflavin (Cullen, 2018). Comparing these results to extrusion based printing of conductive hydrogels, Ma et al. (2019) was able to print poly-l-lactide with PPy NPs using a 260 μm diameter nozzle, which limited their minimum feature size to 260 μm. Vijayavenkataraman et al. (2019) was limited by the 0.8 mm diameter nozzle used and reported major rheological issues while printing, a significant drawback of this creation method. Overall, the results presented in this chapter have shown that all resins were able to achieve minimum feature resolutions smaller than that of current PEGDA stereolithography printing. These results are important because is has been

shown that there is an optimal pore size for osteogenesis. Karageorgiou and Kaplan (2005) found that the minimum pore size was 100 μm for cell migration and ingrowth, whereas scaffolds with $>$ 300 μm was ideal. The larger pore size allowed the formation of capillaries, leading to high oxygenation in the area, subsequently increasing the bone growth (Karageorgiou and Kaplan, 2005). It was seen that all resins were able to achieve resolutions under the recommended 300 μm. Further testing is needed to fine tune and characterize the full capabilities of the PPy/PEGDA resins and their ultimate bone feature resolution. The results outlined in this section have demonstrated the capability of the PPy/PEGDA resins in terms of print resolution and the application towards creating patient customized bone grafts.

4.4.2 Drug Delivery

PPy pH drug delivery has been previously described by Samanta et al. (2015) & Liubchak et al. (2020) and was the basis of this investigation. The theory of PPy pH drug delivery, touched upon in Chapter 2, is that drug molecules are electrostatically charged onto the surface of the PPy NPs, the increase in pH causes increased deprotonation of the PPy backbone, reducing its overall charge and changing the electrostatic interactions that occur with the dopant molecules. Previous studies have failed to test dopant release from PPy over a biologically relevant pH range. FL was chosen as it was a molecule that had previously been tested with PPy NPs and was easily visualized using UV spectroscopy. FL was incorporated during the PPy NP polymerization process, allowing FL attachment to the PPy NP. Vancomycin was used a second dopant because it is a common antibiotic used for Gram-positive infections (Takács-Novák et al., 1993). This positively charged molecule was vortexed with PPy NPs after creation to protect function but still relied on the electrostatic interactions between the drug molecule and the PPy NP. The results outlined from this study showed that there were statistically different increases in FL release over large pH changes. The NPs alone had an increased FL release between

pH 8 & 6, 8 & 6.25 and 8 & 6.75, whereas PEGDA encapsulated NPs showed no statistical difference in FL release at any pH tested. Trends in FL release showed the this molecule favoured alkaline release conditions and were in line with the referencing literature. Samanta et al. (2015) showed that FL release was increased with each pH increment, testing pH 2, 5, 7.4 and 8 after 10 s of vortexing. These increased FL release in alkaline environments was attributed to the negative charge of FL and the electrostatic forces the occur with the changing pH values Samanta et al. (2015). The conditions to trigger significant changes in FL release are contrasted by the pH fluctuations seen in areas of bone regeneration. It was previously shown that physicological pH of 7.4 fluctuates between 7.28 to 7.54 in areas bone regrowth, reported by Chakkalakal et al. (1994) using a rat model. Given this, it can be said that the change in pH around areas of bone regrowth would not cause a significant increase in drug release, although the entrapped dopant molecules would still be delivered over this pH range. The non-significant changes in drug delivery between smaller pH changes may be due to the variance between n values, which yielded larger than expected standard deviations. It is hypothesized that this was due to variances in particles creation and drug loading. The similarity of the PEGDA encapsulated PPy FL release values at the tested pH levels lead to them being calculated as non-significant. This was expected as the hydrogel encapsulation was hypothesized to slow PPy pH triggering and add drug diffusion time into the release parameters. These results are in line with previous work showing that hydrogel networks heavily impact drug delivery. Huang et al. (2004) used allylamine and acrylic-acid based hydrogels networks for controlled drug release and found that dextran release depended on the hydrogel molecular weight and pore size of the hydrogel. These results highlight the hydrogel results in Chapter 3 and show that further tuning of the hydrogel may be needed to facilitate optimal drug delivery. One limitation of the FL polymer release study was that the riboflavin molecule used to cure the PEGDA polymer showed an absorbance at 460 nm. This meant that any excess riboflavin could leach

out of the polymer to increase the absorbance value collected. This is hypothesized to be the reason for the increased FL release values from the hydrogel NPs at the longer time points, see acutely in the 7 and 14 d data. A second hypothesis for this increased release could be that the PEGDA gels are affecting the electrostatic and hydrophobic interactions between the PPy NPs and dopant molecules, triggering a more efficient dopant release (Samanta et al., 2015). To test these hypotheses, future work could utilize a fluorescent molecule for drug loading that does not have an absorption at 460 nm.

Riboflavin absorption was accounted for in the vancomycin testing because there was no overlap between riboflavin and vancomycin at wavelengths over 375 nm. Vancomycin loading had to be modified from the FL doping since the delicate drug molecule would not be functional after being solubilized in an acidic SDS mixture. From this, the methods described by Hosseini-Nassab et al. (2016) for insulin loading of PPy NPs was utilized and the PPy NPs were vortexed to allow surface attachment of the vancomycin. From the outlined results, it was shown that this doping method was successful for vancomycin. For the encapsulated vancomycin-loaded NPs there was a significant increase in release between pH 6.5 and 8, this may be due to the deprotonation of vancomycin. The vancomycin molecule has a pKa of 7.75, moving from an overall charge of (+1) to (0), causing a release from the PPy NPs due to a change in electrostatic interaction between these molecules (Takács-Novák et al., 1993). It was hypothesized that PPy NPs with hydrogel encapsulation would allow for an increasingly controlled release compared to NPs alone. Hydrogel release showed 30.2% dopant release after 2 h compared to 50.7% from the particles alone. After 24 h, the PEGDA encapsulated NPs released 63% of the dopant molecules whereas the particles showed 51% release, less than a 1% increase from the 2 h time point. It can be said that the release of NP alone occurred in the first two hours of being placed into the solution. The remaining 50% may be more tightly bound to the NPs and therefore require a larger pH change to overcome the

electrostatic interactions. The PEGDA PPy NPs had an extended release timeline that occurred after sometime between the 2 and 24 h time points. These results showed the benefits of the hydrogel entrapment to create a controlled drug release mechanism that may have increased clinical significance compared to burst release. Comparing release percentages to other studies, Samanta et al. (2015) showed that PPy NPs alone yielded approximately 25% peroxicam release after only 10 s of vortexing at pH 8, validating that the unencapsulated NPs respond quickly to the change in pH. Looking at longer PPy release studies, Zanjanizadeh Ezazi et al. (2018) showed 80% vancomycin release from silica particles when combined with gelatin, PPy and hydroxyapatite over a four month period compared to scaffolds without PPy, which only yielded 50% drug release. These authors were only interested in a single pH value of 7.4, but did help demonstrate that PPy has a positive effect on drug delivery, which they attributed to the the positive chains of PPy repelling the positively charged vancomycin. Additionally, the previous study was only able to achieve an encapsulation efficiency of 6.5%, compared to 16% in this thesis. It was hypothesized that a larger drug concentration was entrapped into the PPy NPs due to the high surface area-to-volume ratio that is a main characteristic of NPs. This high surface area may also have led to a faster switching method, which is why there was over 50% dopant release seen in only 24 h. Future studies are needed to investigate the complex interaction between PPy and vancomycin, but this work has shown the benefits of combining hydrogels and PPy NPs into a composite material for drug delivery applications. Additionally, combining the 3D printing capabilities of these resins could impact the drug delivery capability of these NPs encapsulated in PEGDA. The geometry could impact the diffusion variables or exposed surface area to control the release rate to suit a variety of applications. The pH-dependent nature of PPy NPs make them an ideal candidate for drug release inside the human body where pH fluctuations are common.

4.5 Chapter summary

The chapter has applied the previously described PPy NPs and PPy/PEGDA resins. The 3D printing capability of the resins was investigated through the use of a custom designed stereolithography printer, validating its use to recreate complex bone morphology. Additionally, the drug delivery capability of PPy NPs was tested over biologically relevant pH ranges, showing higher release at higher pH values. This chapter opens up new research directions in various types of 3D geometries and dopant molecules for PPy/PEGDA scaffold drug delivery. The results have demonstrated the capability of these resins to create patient-customized scaffolds that are capable of drug delivery inside the human body for improved osteogenic healing.

List of references

Chakkalakal, D. A., Mashoof, A. A., Novak, J., Strates, B. S. and McGuire, M. H. (1994), 'Mineralization and ph relationships in healing skeletal defects grafted with demineralized bone matrix', *Journal of Biomedical Materials Research* **28**(12), 1439–1443.

Cullen, A. (2018), 'Fabrication of 3d conjugated polymer structures via vat polymerization additive manufacturing', *Electronic Thesis and Dissertation Repository* .

Doughty, M. J. (2010), 'ph dependent spectral properties of sodium fluorescein ophthalmic solutions revisited.', *Ophthalmic Physiol Opt* **30**(2), 167–174.

Fantino, E., Roppolo, I., Zhang, D., Xiao, J., Chiappone, A., Castellino, M., Guo, Q., Pirri, C. F. and Yang, J. (2018), '3D Printing/Interfacial Polymerization Coupling for the Fabrication of Conductive Hydrogel', *Macromolecular Materials and Engineering* **303**(4), 1700356.

Hosseini-Nassab, N., Samanta, D., Abdolazimi, Y., Annes, J. P. and Zare, R. N. (2016), 'Electrically controlled release of insulin using polypyrrole nanoparticles.', *Nanoscale* **9**(1), 143–149.

Huang, G., Gao, J., Hu, Z., St. John, J. V., Ponder, B. C. and Moro, D. (2004), 'Controlled drug release from hydrogel nanoparticle networks', *Journal of Controlled Release* **94**(2), 303–311.

Karageorgiou, V. and Kaplan, D. (2005), 'Porosity of 3D biomaterial scaffolds and osteogenesis', *Biomaterials* **26**(27), 5474–5491.

Li, X., Wang, Y., Wang, Z., Qi, Y., Li, L., Zhang, P., Chen, X. and Huang, Y. (2018), 'Composite PLA/PEG/nHA/Dexamethasone Scaffold Prepared by 3D Printing for Bone Regeneration', *Macromolecular Bioscience* **18**(6), 1800068.

Liubchak, I., Lawrence, M. T., Holness, F. B. and Price, A. D. (2020), 'Soft template electropolymerization of polypyrrole for improved ph-induced drug delivery', *International Journal of Molecular Sciences* **21**(21).

Ma, C., Jiang, L., Wang, Y., Gang, F., Xu, N., Li, T., Liu, Z., Chi, Y., Wang, X., Zhao, L., Feng, Q. and Sun, X. (2019), '3D Printing of Conductive Tissue Engineering Scaffolds Containing Polypyrrole Nanoparticles with Different Morphologies and Concentrations', *Materials* **12**(15), 2491.

Nguyen, A. K., Gittard, S. D., Koroleva, A., Schlie, S., Gaidukeviciute, A., Chichkov, B. N. and Narayan, R. J. (2013), 'Two-photon polymerization of polyethylene glycol diacrylate scaffolds with riboflavin and triethanolamine used as a water-soluble photoinitiator', *Regenerative Medicine* **8**(6), 725–738.

Samanta, D., Meiser, J. L. and Zare, R. N. (2015), 'Polypyrrole nanoparticles for tunable, pH-sensitive and sustained drug release', *Nanoscale* **7**(21), 9497–9504.

Takács-Novák, K., Noszál, B., Tókés-Kövesdi, M. and Szász, G. (1993), 'Acid-base properties and proton-speciation of vancomycin', *International Journal of Pharmaceutics* **89**(3), 261–263.

Vijayavenkataraman, S., Kannan, S., Cao, T., Fuh, J. Y. H., Sriram, G. and Lu, W. F. (2019), '3d-printed pcl/ppy conductive scaffolds as three-dimensional porous nerve guide conduits (ngcs) for peripheral nerve injury repair', *Frontiers in Bioengineering and Biotechnology* **7**, 266.

Zanjanizadeh Ezazi, N., Shahbazi, M.-A., Shatalin, Y. V., Nadal, E., Mäkilä, E., Salonen, J., Kemell, M., Correia, A., Hirvonen, J. and Santos, H. A. (2018), 'Conductive vancomycin-loaded mesoporous silica polypyrrole-based scaffolds for bone regeneration', *International Journal of Pharmaceutics* **536**(1), 241–250.

Chapter 5

Biocompatibility Testing of Printed PPy/PEGDA Resin

This chapter outlines the biological testing on the previously described PPy/PEGDA printed resins. These are vital tests for the proper function for biomaterials and their applications *in-vivo* under biological conditions. The cytotoxicity and cell adhesion of the PPy/PEGDA polymers were tested with pre-osteoblastic cells to understand these interactions. These evaluations are the first step in the validation of PPy/PEGDA scaffolds used for bone regeneration.

5.1 Introduction

The success of any biomaterial depends heavily on the ability to interact with the surrounding tissues. Dee et al. (2002) described the tissue-biomaterial interface as a complex milieu with chemical, electrical and mechanical interactions occurring. The purpose of biomaterials is to integrate with the surrounding environment, restoring proper function without disruption (Dee et al., 2002). Given this information and the successful creation of PPy/PEGDA polymers, the biological interaction of the material needed

to be analyzed. The PPy/PEGDA polymers must not be cytotoxic or have cytotoxic leachates, ensuring no damage to the surrounding cells when used *in-vivo*. In addition to cytotoxicity, qualitative cell adhesion with the scaffold material was investigated as these interactions can dictate cell morphology, viability and signalling. Previous studies have explored PPy and PEG but this work is the first to investigate the addition of PPy NPs on the cytotoxicity and cell adhesion of PEGDA. The addition of PPy NPs showed no adverse cytotoxic effects whereas the cell adhesion was drastically improved. The results from this work validate that PPy/PEGDA can be used as a biomaterial with applications in replacing traditional bone grafts.

5.2 Materials and Methods

5.2.1 Materials

MC3T3-E1 pre-osteoblast cells from mouse calvaria were used in all experiments outlined below. Cell adhesion studies used Minimum Essential Medium-α (α-mem) (ThermoFisher Cat. #12571063) whereas cytotoxicity testing used Minimum Essential Medium-α without phenol red (ThermoFisher Cat. #41061029). Fetal bovine serum (FBS) (ThermoFisher Cat. #12483020), Penicillin-Streptomycin (ThermoFisher Cat. #15140122) and Dulbecco's phosphate-buffered saline (DPBS) (ThermoFisher Cat. #14190144) were used as received. The CyQUANT XTT Cell viability assay was used as purchased from ThermoFisher (Cat. #X12223). 100% Ethanol was diluted with distilled water down to 70% for sterilization purposes. Trypsin was diluted in cell culture media to 0.25 (w/v). 0.1% Gelatin solution was created and sterilized for cell culture. PBS was used to create 1% Bovine Serum Albumin (BSA) blocking solution and 0.1% Triton X-100 solution. Alexa Fluor 488 Phalloidin and Hoechst 33342 were used for cell staining.

5.2.2 Methods

Cell culture media was prepared by combining α-mem, 10% FBS and 1% penicillin-streptomycin followed by sterile filtration. Cells were maintained by changing culture media every two days and passaging at 80% confluence with a 1:10 split ratio.

For cytotoxicity testing, the same PPy/PEGDA resins from Chapter 3 were cast in quadruplicate with an area of 1.2 cm $\times$ 1 cm and a thickness of 1 mm. Cured polymers were placed into 3 ml of 70% ethanol overnight. The following day, polymers were moved into a bio-safety cabinet and washed twice with DPBS for 15 min each, followed by a 30 min cell culture media soak at 37 °C. This removed any DPBS salts or ethanol entrapped in the scaffold. Two polymers were then moved into one new culture well, totalling 2.4 cm^2 of polymer area. According to International Organization for Standardization (ISO) 10993-12: Section 10.3.3, which defines the surface area to media volume ratio for cytotoxicity testing, 800 μl of cell culture media with no phenol red was added to each well. The polymers were incubated for 14 d, 7 d, 72 h and 24 h. During this time the media quantity was monitored to check if it dropped below 300 μl, the volume needed for a triplicate test. If the media had evaporated, 100 μl of fresh media was added. The polymer soaking periods were staggered-started so all media would reach the desired time point on a single day when the cells were 80% confluent. Two days before the media reached its time point, MC3T3-E1 cells were passaged into 96-well plates with a cell density of 15,000 cells$/cm^2$, correlating to 4,800 cells$/$ well, with media containing no phenol red. This allowed the cells to reach 80% confluence on the day of the experiment. Additionally, two triplicates of a standard curve containing 500, 1,000, 2,500, 5,000 and 7,500 cells$/$ well were plated, the first to measure absorption values from the XTT assay and the second to perform cell counts. On the day of the experiment, the original cell culture media was removed and 100 μl of polymer-soaked media was added to each well in triplicate. A positive control was created by adding 100 μl of media with 35 mmol SDS to promote cell death. The standard curve and

negative-control media was changed with fresh phenol-red free media. Three wells with only media were left to serve as blanks. The cells were left to incubate for 24 h. The following day, the XTT assay was mixed according to the given instructions, 2 ml of the Electron Coupling reagent was added to 12 ml of the XTT reagent and vortexed. Directly following vortexing, 70 μl of the XTT solution was added to each test well and left to incubate for 4 h at 37 °C and 5% CO_2. After incubation the plate was protected from light and moved to a TECAN Safire plate reader and read at 450 nm for XTT absorption and 660 nm to pick up any debris. The specific absorbance and cell viability were calculated using the following formulas.

$$Absorbance = [Abs_{450}(Test) - Abs_{660}(Blank)] - Abs_{660}(Test) \tag{5.1}$$

$$\%\ Viability = \frac{[Abs_{450}(Test) - Abs_{660}(Test)]}{[Abs_{450}(Blank) - Abs_{660}(Blank)]} * 100 \tag{5.2}$$

The second standard curve was used to gather direct cell counts. 30 μl of trypsin was added to each well, incubated for 4 min and neutralized by 70 μl of cell culture media. Cells were counted using a hemocytometer and correlated to the standard curve absorbance data from the XTT assay.

Cell adhesion studies were completed by curing polymers at various PPy concentrations in 1.2 cm $\times$ 1 cm molds. An analogous preparation method was implemented for the cell adhesion studies with one change, the cell culture media was extended to 3 h at 37 °C. All volumes refer to preparation in standard 12-well plates. Initially, no coatings were applied to the polymer and the cell were plated directly on top using a monolayer culture method. Subsequent ECM coatings of 0.1% gelatin or 100% FBS were used directly after the media soak. 1 ml of 0.1% gelatin or 100% FBS was added to each well, incubated for 1 h with a 10 min drying period. Plating densities of 5,000, 15,000 and 30,000 cells$/cm^2$ were achieved after completing a cell-count and adjusting the media volume to 1 ml$/$ well. The polymers were incubated for five days with media changes

every other day to ensure there was adequate time for cell adhesion and growth. After five days, the polymers were carefully moved into an adjacent empty well. Both the polymer and cell-plating well were stained with Hoechst and Phalloidin stains to visualize the cell nuclei and cytoplasmic actin, respectively. The cell plating wells acted as a reference for cell attachment. The staining process was completed as described. Both the polymer and culture well were twice-rinsed with DPBS before being fixed with 0.1% PFA for 10 min, followed by two 5 min PBS rinses. A blocking solution of 1% BSA in PBS was applied for 30 min and washed again with two 5 min PBS rinses. Actin staining used 800 μl PBS with 20 μl stock Phalloidin. 200 μl of diluted stain was added to each well and incubated for 20 min with agitation. Two 5 min PBS rinses were completed. Nuclear staining used 1 ml/well of Hoechst stain (diluted to 1000:1) for 10 min followed with two 5 min PBS rinses. Cells were imaged using a Leica DMI6000 microscope.

5.3 Results

5.3.1 Cytotoxicity

The cytotoxicity of four PPy/PEGDA formulations were investigated according to the ISO protocol #10993: *Biological evaluation of medical devices*, specifically referencing Parts 5 and 12, *Tests for in vitro cytotoxicity* and *Sample preparation and reference materials* (International Organization for Standardization, 2012). Four time-points for polymer soaking were chosen: 24 h, 72 h, 7 d and 14 d to exaggerate testing conditions. These results are summarized in Figure 5.1 and Table 5.1, reported with SE of the mean (n = 4).

Cell viability was used to compare polymer-soaked media cell activity to the control wells, calculated using Equation 5.2 as defined by ISO #10993-5 *Cytotoxicity - XTT Assay*. The formula used the control well as 100% viability to visualize cell growth/death. The ISO defines cytotoxicity as <70% cell viability, which was seen in the positive

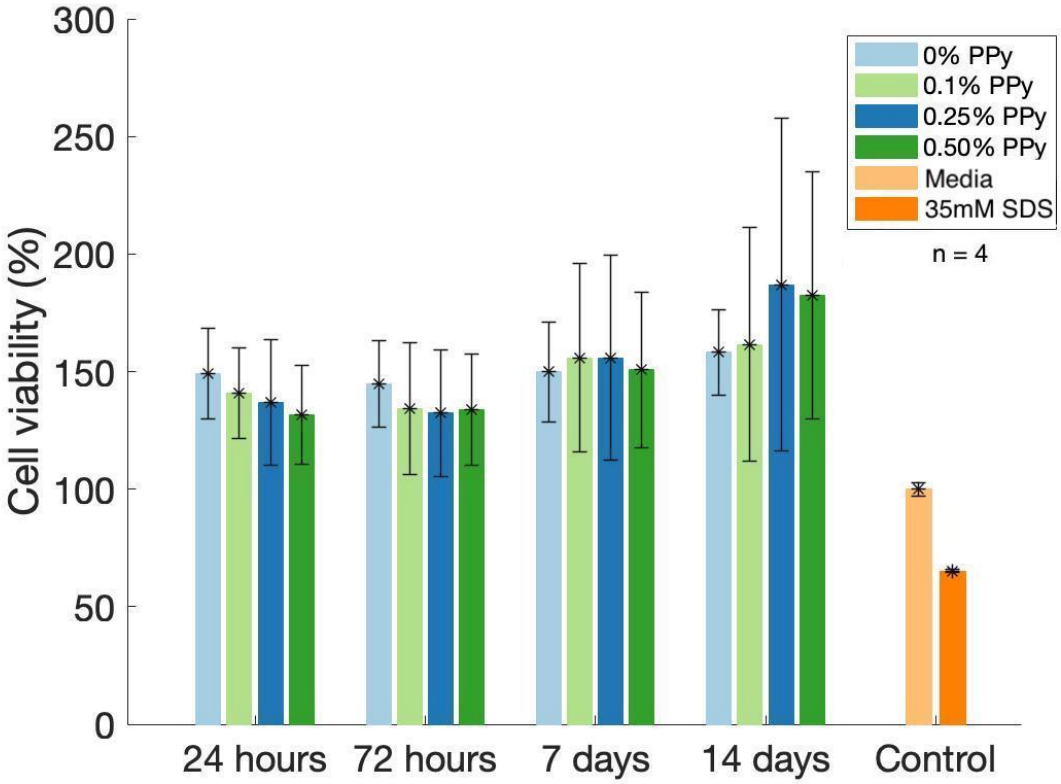

Figure 5.1: Cell viability from the XTT assay calculated using Equation 5.2 after exposure to conditioned media for 24 h. Regular media was used as the negative control and 35 mmol sodium dodecyl sulfate in culture media was used as the positive control. There were no significant differences between treatment groups, demonstrating that no cytotoxic effects from the polymer over a 14 d time period at all PPy concentrations tested. Reported as the mean with standard error (n = 4).

	Cell Counts (Mean ± Standard Error)							
PPy	24 h		72 h		7 d		14 d	
0	22,300	7,300	20,900	6,700	22,500	8,700	25,200	6,300
0.10	19,600	4,600	17,500	6,500	24,400	9,700	26,200	12,700
0.25	18,300	6,400	16,900	5,900	24,400	10,800	34,400	19,500
0.50	16,700	5,300	17,300	5,200	22,700	7,500	32,900	13,700

Table 5.1: Calculated cells/well from the XTT absorbance data using Equation 5.1 and the plated standard curves to create a linear formula relating absorbance to cell numbers. No statistical difference was seen between any the timepoints or PPy concentrations. Results reported with the standard error (n=4) and rounded to the nearest hundredth.

control of 35 mmol SDS media with a viability of 65%. All polymer samples had an average cell viability % ranging from 130% (24 h, 0.5 PPy) up to 186% (7 d, 0.25 PPy). The shorter two timepoints showed minor decreases in the average viability as the concentration of PPy was increased. The longer timepoints showed no trend between PPy concentration and average viability. The results showed an increased average viability when using polymer-soaked media compared to the negative control, but no significant differences were seen using a one-way ANOVA test with a p-value of 0.05. Looking at Table 5.1, the 24 and 72 h time points showed similar cell counts for all PPy concentrations, ranging from 16,700–22,300 cells/well, whereas the 7 and 14 d had higher average cell numbers between 22,500–34,400 cells/well. Samples from the 72 h experiment yielded the lowest average cell counts for all PPy concentrations. Conversely, the 14 d samples yielded the highest average cell counts compared to the three shorter timepoints for all PPy concentrations. Looking at the SE for the samples, it was seen that the viability SE mirrors the same trends as the average cell counts, increasing with the time of polymer-soak. The 14 d samples showed the largest variance, specifically the 0.25% sample with a SE of $\pm 19,500$ cells/well, four times the smallest SE value seen with the 24 h, 0.1% sample of $\pm 4,600$.

5.3.2 Cell Adhesion

Cell adhesion studies were completed in an iterative manner to maximize the bioactivity of PPy/PEGDA. The un-coated polymers were first tested to see if the MC3T3-E1 cells would adhere to the PEGDA polymer, with and without 0.1 PPy NPs, seeded at a cell density of 5,000 cells$/$cm^2. It was observed that there were no cells adhered to the surface of either polymer. Phase contrast images were taken to confirm that images were taken on the polymer surface and not on the plate below. From these results, the investigation into additional ECM coatings began. To increase the cell adhesion, two different ECM coatings were applied to the polymers with and without PPy NPs (0.2 wt% PPy H_2O creation solution) with a higher cell density. Figure 5.2 showed the cell adhesion on the polymers seeded with a cell density of 15,000 cells$/$cm^2 with either gelatin or FBS coatings. Qualitative observations from cell images dictated the coating success. It was observed from the images that there were cells attached to both coatings, an improvement from the uncoated polymers. The gelatin coating, seen in panels (a) & (b), showed less pronounced cell spreading (as indicated by actin cytoskeleton visualization) compared to the FBS coatings, seen in panels (c) & (d). The number of nuclei were still considered low but were comparable between the two coatings.

From the coatings results, FBS was selected to be used in future experiments and the study moved to increasing the PPy NP concentration. Four PPy NP suspension concentrations (0, 0.1, 0.25 & 0.5 wt% PPy) were incorporated into the PEGDA polymers. The polymers were seeded at three cell densities to investigate the impacts of PPy concentration and plating density on cell adhesion. The results of the study were outlined in Figure 5.3 and Figure 5.4, along with corresponding phase contrast images in Figure A.1 and Figure A.2. It was observed that there were very few nuclei attached to the 0 PPy polymers in panels, validating the results of Figure 5.2. The cells on the 0 PPy polymers appeared to be rounded with clusters of nuclei seen with little surrounding

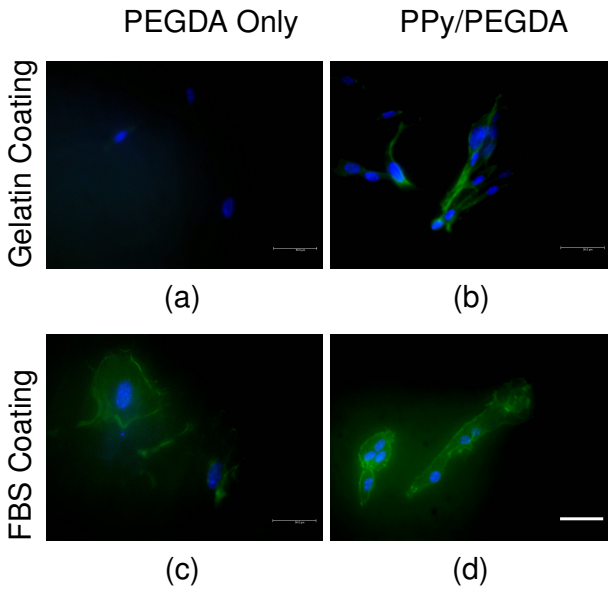

Figure 5.2: MC3T3-E1 pre-osteoblast cells stained with Hoechst (cell nuclei stained blue) and phalloidin (actin filaments stained green) fluorescent imaging seeded onto PEGDA polymers, with and without PPy NPs, with two surface treatments. Panels (a) and (b) were treated with a 0.1% gelatin coating and panels (c) and (d) were treated with a 100% FBS coating, both plated at 15,000 cells$/$cm^2. It was observed that the FBS coating provided better cell attachment, seen through the actin staining in green. This allowed the qualitative selection of FBS used in the following tests. Scale bar denotes 50 μm.

actin being observed. Qualitatively, with each increase in PPy concentration, there was a corresponding increase in the cell adhesion of the polymers, demonstrated by an increased number of nuclei and presence/extended shape of actin fibres. The 0.1 PPy samples showed similar results to the 0 PPy polymers with low number of cell nuclei and very little actin being visualized. There was a qualitative increase in the number of nuclei and actin fibres seen attached to the 0.25 and 0.5 PPy samples at all cell densities. Specifically, there were larger actin extensions visualized between cells as opposed to the rounded cells seen on the 0 and 0.1 PPy polymers. Even at the lowest plating density, there was an increased presence of nuclei imaged with each increase of PPy concentrations. These images are compared against the control of the surrounding cell culture plastic, seen in panels (m), (n) and (o) of Figure 5.3. The culture plastic cell

adhesion showed that none of the PPy concentrations were able to mimic the same adhesive properties.

Figure 5.4 was collected from the same polymers seen in Figure 5.3 at a higher magnification to visualize the cell morphology. Higher magnification allowed the visualization of the actin fibres that show cell spreading, a positive sign a cell attachment. The 0 PPy and 0.1 PPy samples again showed rounded actin filaments, pointing towards a non-adhesive surface inhibiting cell attachment. Additionally, the 0.1 PPy sample showed distinct clusters of cells attached between PPy NPs, seen in panels (m), (n) & (o) of Figure 5.4. Cells appeared to favour scaffolds with higher concentrations of PPy with a qualitative increase in the presence of nuclei. There was also a marked increase in the visualization of actin filaments in the 0.25 and 0.5 PPy polymers compared to lower PPy concentrations. The higher PPy concentrations showed clusters of nuclei with outgrowths of actin connecting each cluster.

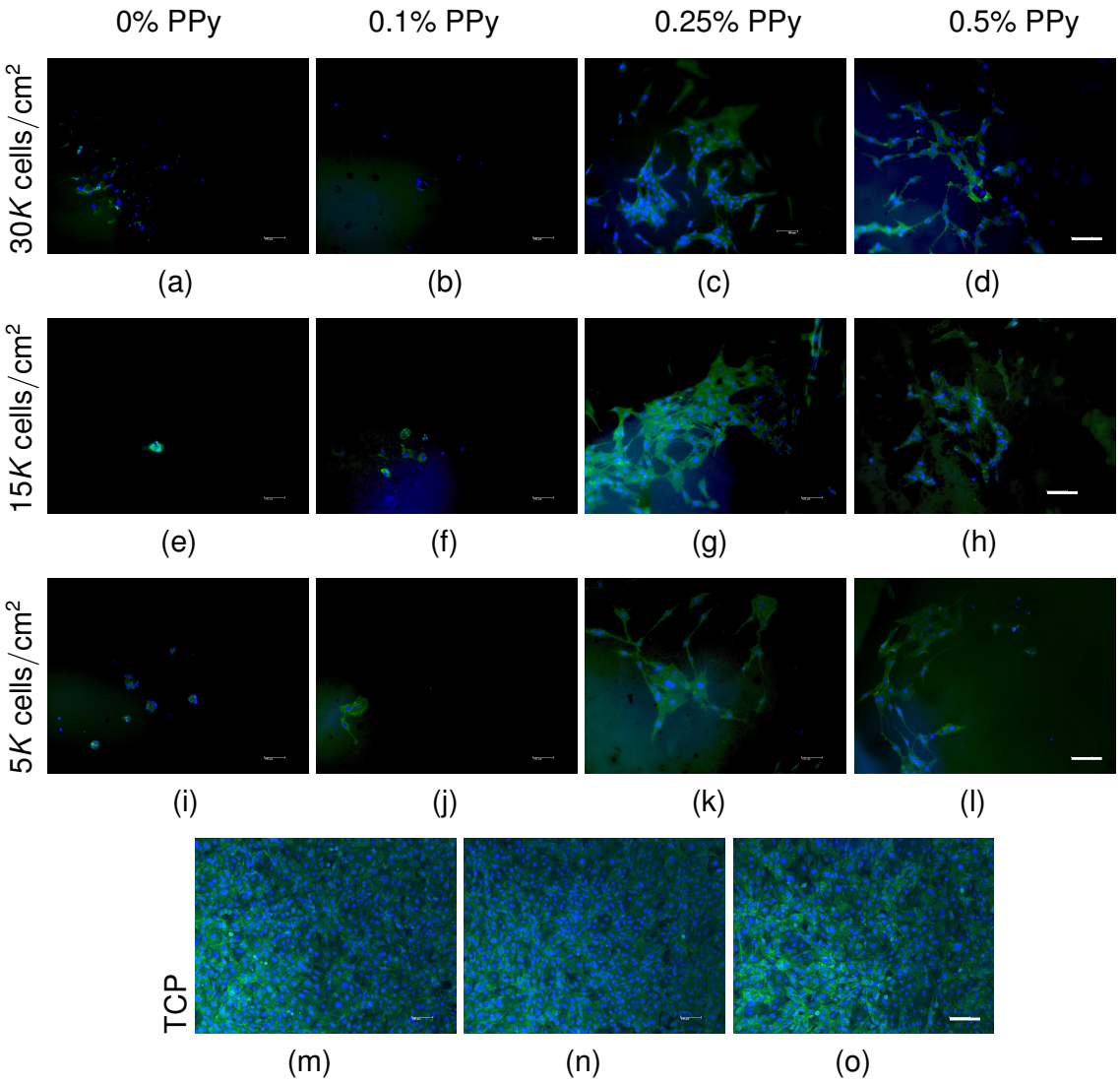

Figure 5.3: MC3T3-E1 pre-osteoblast cells stained with Hoechst (cell nuclei stained blue) and phalloidin (actin filaments stained green) seeded onto 0, 0.1, 0.25 & 0.5 % PPy polymers, plated at three cell densities: 30,000, 15,000 & 5,000 cells/cm^2 cultured for 5 d. Compared to the control of the surrounding tissue culture plastic (TCP) in panels (m), (n) and (o) for 30,000, 15,000 & 5,000 cells/cm^2, respectively. The cell adhesion qualitatively increased as the amount of PPy was increased, seen by the increased presence of cell nuclei and actin fibres. Scale bar denotes 150 μm.

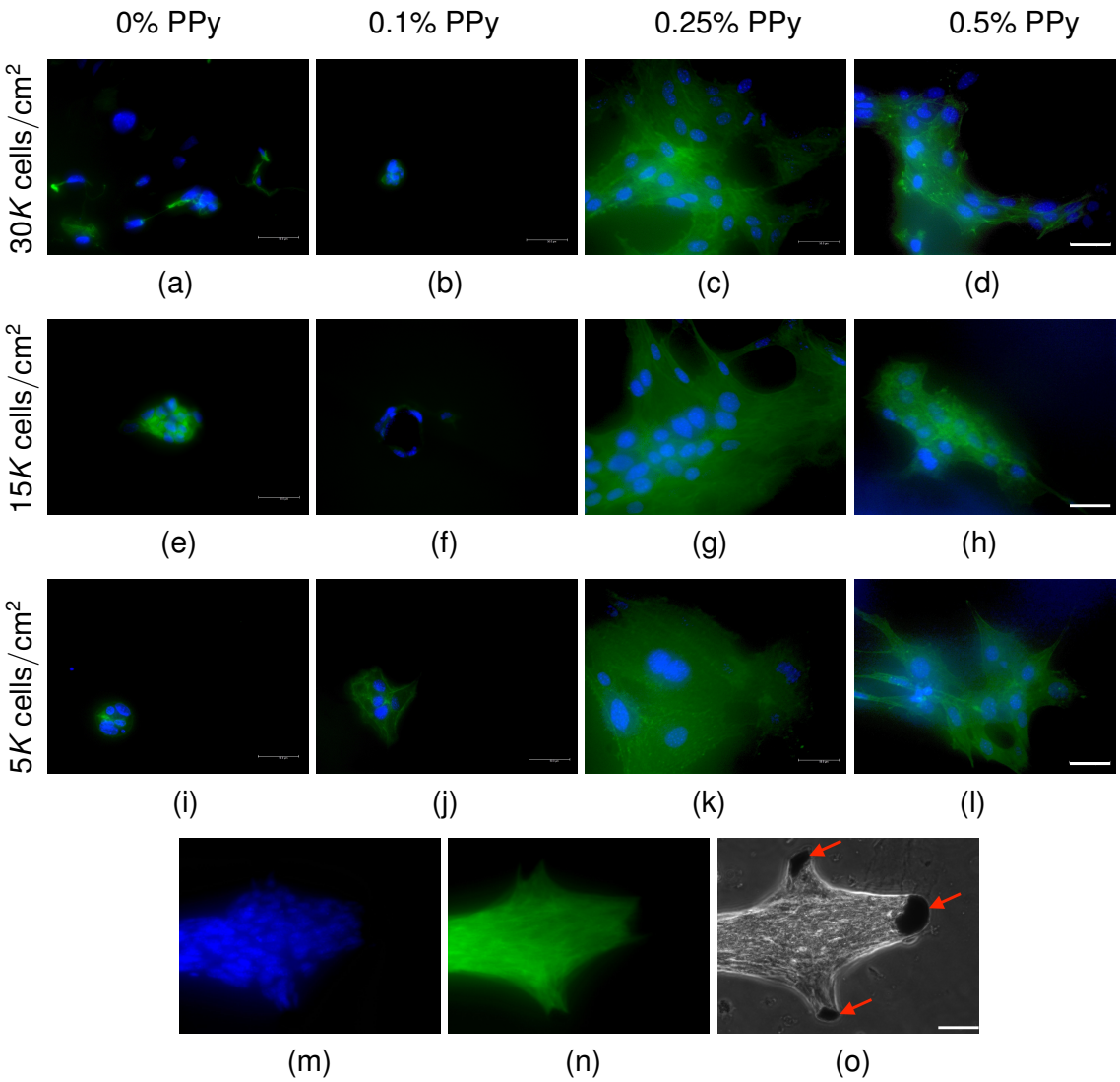

Figure 5.4: MC3T3-E1 pre-osteoblast cells stained with Hoechst (cell nuclei stained blue) and phalloidin (actin filaments stained green) seeded onto 0.1, 0.25 & 0.5 % PPy polymers, plated at three cell densities: 5,000, 15,000 & 30,000 cells/cm^2 cultured for 5 d. The cell spreading was qualitatively increased with the addition of PPy NPs, visualized by the actin fibre extension between nuclei. Panels (m) to (o) demonstrate the cell adhesion to PPy NPs (marked with red arrows). Scale bar denotes 50 μm.

5.4 Discussion

5.4.1 Cytotoxicity

All tests used MC3T3-E1 pre-osteoblast cells harvested from mouse calivaria given the bone regeneration application of these materials. The ISO 10993 - *Biological evaluation of medical devices* was referenced heavily during the creation of this experiment to ensure that proper protocols were followed. The ISO outlined a required 24 h exposure at 37 C but extended time points were added to better fit the application of this polymer. Since these materials would stay inside the body, extended polymer soaking time points up to 14 d allowed the long term impacts to be visualized. An extract method of testing cytotoxicity was selected because it could facilitate the exaggerated leachate release from the polymers, not achievable with other methods. Both types of contact testing (direct and indirect) require the polymer to be in contact with the cell culture media as cells proliferate and are therefore limited by the media-change or passage frequency. The XTT assay ((2,3-bis(2-methoxy-4-nitro-5-sulfophenyl)-5-[(phenylamino)carbonyl] -2H-tetrazolium hydroxide), referred to as XTT) was chosen because it was a measure of cell metabolic activity through mitochondrial dehydrogenases (Scudiero et al., 1988). XTT was reduced in metabolically active cells into a photometric assay which was related to the cell death caused by polymer leachates.

The cytotoxicity results showed that the developed polymer sterilization protocol for cell culture was successful. The overnight 70% ethanol soak was long enough to allow the ethanol to penetrate into the core of the polymer while washing away any uncured monomers, a main source of cytotoxicity (Liu et al., 2017). Additionally, the ethanol removed excess riboflavin, which was a large source of autofluorescence during cell imaging in the *Cell Adhesion* tests due to its board absorption spectrum, seen in Figure 3.2. The subsequent DPBS rinses along with the media incubation allowed the ethanol to be successfully removed before plating cells. The results confirm that the

protocol outlined in the *Methods* section yielded a sterilized polymer.

The results from the XTT assay showed the PPy/PEGDA materials were non-cytotoxic over the 14 d period. There were no adverse impacts on cell viability from the polymer-soaked media at any of the four timepoints. The addition of PPy NPs at concentrations up to 0.5% had no effect on the cell viability compared to PEGDA alone, showing that the NP dialysis wash removed the acid and SDS that would have killed the cells. The results of this study was validated through the cell adhesion experiments will optimal cell growth occurring on the surrounding cell culture plastic alongside the polymers, seen in panels (m), (n) and (o) of Figure 5.3 for the 0.5 PPy sample. These results confirm the hypothesis that the polymers would be non-cytotoxic due to the materials and photoinitiator chosen. PEGDA and PEG derivatives are known to be bioinert and well-tolerated with a range of cell types (Unagolla and Jayasuriya, 2020; Zhu, 2010; Liu et al., 2017). The main source of cytotoxicity when working with polymers is the presence of uncured monomers, which were removed from the prints during the ethanol soak (Liu et al., 2017). Looking specifically at MC3T3-E1 cell interaction with PEG, previous research has used PEG in conjugation with poly-lactic acid and hydroxyapatite for dexamethasone drug delivery that was tested with MC3T3-E1 cells and showed no cytotoxicity (Li et al., 2018). Additionally, Carles-Carner et al. (2018) used PEG hydrogels to encapsulate MC3T3-E1 cells with no cytotoxicity. These studies are in line with our findings that PEGDA had no cytotoxic effects over a 14 d period on osteoblast cells. Riboflavin was selected as the photo-initiator for this application because of its compatibility compared to commercially available photoinitiators (Nguyen et al., 2013). Nguyen et al. (2013) used both PEGDA and riboflavin with GM-7373 bovine aortic endothelial cells and showed that there was no cell death using a LIVE/DEAD assay, our results extend these findings to MC3T3-E1 cells. Chaves Neto et al. (2010) investigated the use of riboflavin in MC3T3-E1 cells in cell culture and showed that it had no effect on cell-viability, which was validated by the cell-viability results from the 0

PPy prints in this study. Looking at the results from the increasing PPy concentrations in PEGDA resin, it was seen that there were no cytotoxic effects due to the PPy NPs and there were no significant differences between samples or timepoints. Ramanaviciene et al. (2007) previously showed that PPy NPs tested in the peritoneum of mice had no cytotoxic effects over a 6-week period. Our findings on PPy NP cytotoxicity with MC3T3-E1 cells fit with these results. This is encouraging because the PPy NPs used in this thesis were created with H_2O_2 oxidative polymerization methods with an SDS additive that has not been previously studied. The viability results, seen in Figure 5.1, showed an overall increase in the cell viability compared to the negative-control, cultured with regular media. The average cells calculated increased alongside the duration of polymer-soaking, seen in Table 5.1. The 72 h cell counts were seen to be the lowest for all PPy concentrations whereas the 14 d cell counts were the largest. This increase in cell viability over time can be attributed to two working hypotheses. First, the toxic leachates that are the most cytotoxic to cells are being degraded over time due to the increased temperature or by components of the cell culture media. This means that the shorter soaking times kept the cytotoxic elements in the fluid and could be applied to the cells before degradation. Further studying of the leachates present in the cell culture media at each timepoint could help elucidate this hypothesis but was not considered in the scope of this study. Secondly, the release of excess riboflavin that was not removed during the ethanol soak could have increased the absorption. Additionally, riboflavin is a component of the α-mem media chosen for this cell line at a concentration of 0.1 mg$/$l and it reported to have a role transferring electrons in the metabolic processes of cells (Millipore-Sigma, 2021; Thermo-Fisher, 2021; Chaves Neto et al., 2010). This means that as the polymer leachate time is extended there may be increased levels of riboflavin in the media that could be facilitating a minor increase in cell metabolism. To investigate this, a future study could use UV spectroscopy on polymer soaked cell culture media to calculate the concentration of riboflavin as a function of time to see if

there is a significant increase. Overall, this study has shown that the PEGDA materials with 0, 0.1, 0.25 & 0.5 PPy NPs are not cytotoxic to MC3T3-E1 cells over a 14 d period following the outlined ISO 10993 standards and can be used in future studies as a composite biomaterial.

5.4.2 Cell Adhesion

Interpreting the results from the cell adhesion studies, in was seen that PEGDA is not biologically active and alone does not support cell growth. The bio-inert nature of PEGDA was validated with no MC3T3-E1 cells able to be visualized on the polymer surface. Previous studies have shown that PEG does not have optimal cell adhesion but can be modified with various types of molecules to create a bioactive polymer(Zhu, 2010). It was hypothesized that the PPy NPs would add cell attachment points to allow the cells to adhere to the polymer. PPy was chosen for this application because it has previously been used with cells for osteogenic applications (Jie et al., 2017; Liu et al., 2013; He et al., 2017). He et al. (2017) investigated the use of PPy coatings for bone implants, showing that PPy nano-wires benefitted cell growth compared to titanium and normal “cauliflower-like” morphology PPy. Chitosan/PPy–alginate bone scaffolds were created by Sajesh et al. (2013) using chemical synthesis. The scaffolds demonstrated increased cell proliferation with the addition of PPy-alginate compared to chitosan only scaffolds with mg-63 osteoblast cells. These works demonstrate the cell adhesion capability of added PPy. From the pilot test, it was determined that PPy NPs would have to be used in conjunction with a second method to increase the cell adhesion of PEGDA.

To increase the cell adhesion of the PPy/PEGDA polymers, ECM coatings were added as a step before cell plating. Coatings were chosen because they have previously been used as surface coatings on cell culture plastic and silicone testing equipment, where certain cells would not normally adhere (Bello et al., 2020; Lee et al., 2019;

Kim et al., 2020). Gelatin, a natural polymer made of denatured collagen provided linear proteins that served as cell attachment points alongside the PPy NPs (Bello et al., 2020). FBS provided similar benefits to gelatin in a non-denatured form that was hypothesized to offer improved cell adhesion for the PPy/PEGDA polymers. Figure 5.2 panels (a) and (b) with a 0.1% gelatin coating showed that cells were able to adhere to the polymer. The FBS coatings, seen in panels (c) and (d), had a similar increase in cell adhesion as gelatin. These results were expected as the ECM components of both gelatin and FBS coated the polymer surface to act as attachment points and may have influenced cell signalling. Previous work has shown that ECM proteins bind to cell receptors and trigger a multitude of downstream cell-signaling effects such as gene and protein expression (Zhu, 2010). From these initial pilot studies investigating the ECM coatings, it was chosen that FBS would be used going forward as it qualitatively showed the a positive effect on actin fibres. With this coating, the impact of modifying the concentration of PPy NPs could be investigated.

Figure 5.3 and Figure 5.4 both showed a qualitative increase in cell adhesion when an increased concentration of PPy NPs was incorporated into PEGDA and the cells were plated at higher densities. Both of these results were expected. The higher cell density allowed a larger number of cells to be deposited on the polymer, offering an increased chance of attachment. Additionally, the higher cell densities could have increased cell-to-cell interactions and signalling, facilitating adherence. It was hypothesized that the 0.25 and 0.5 PPy polymers offered an increased presence of PPy NPs at the surface and created a rougher surface for cell adhesion compared to PEGDA. The rougher surface and increasingly black polymer was seen in Figure 3.5 as the PPy concentration was increased. Looking at panels (m), (n) & (o) of Figure 5.4 it was noted that the cells were stretched between clusters of PPy NPs. This finding was seen commonly in the 0.1 PPy samples and points towards cells preferentially adhering to PPy NPs compared to PEGDA. This finding highlighted the hypothesis that PPy NPs would act as cell

attachment points and was qualitatively confirmed when imaging the 0.25 and 0.5 PPy samples but would need further testing to fully elucidate. The higher concentration of PPy NPs allowed for an increased presence of nuclei and actin filaments attached to the polymer surface, seen in Figure 5.4. This hypothesis may be supported by the results outlined by Schexnailder et al. (2010) with polyethylene oxide, another polymer that does not support cell adhesion. This author used added silicate NPs in polyethylene oxide, but cell adhesion and proliferation was only achieved with higher concentrations (<40 wt.%) of silicate NPs. The best cell adhesion was seen with 70 wt.% silicate NPs, a much higher concentration than the maximum PPy NP concentration chosen for this study. Gaharwar et al. (2013) incorporated silica nanospheres into PEG hydrogels to increase the fibroblast adhesion. PEG with 1, 5 and 10% silica nanospheres showed an improved cell adhesion with each % increase, matching the results seen in our study. These studies are in line with the trends outlined in the results section with smaller percentages of PPy incorporated into the PEGDA resin tested. The concentration of NPs added into the PPy/PEGDA resin was limited due to the UV curing inhibition described in Chapter 3. From the results of this study, it was concluded that the addition of PPy NPs provided a qualitative increase in cell adhesion compared to PEGDA alone and that the 0.25 and 0.5 PPy polymers allowed a marked increases in nuclei attached and actin filaments between cells. A significant concentration of PPy NPs was not added to the PEGDA hydrogels to define them as an optimal cell binding surface compared to cell culture plastic, but the results provide insight into finding the critical % of PPy for cell adhesion. Future studies should include methods to allow increased PPy at the polymer surface through interfacial PPy polymerization or by overcoming the UV curing challenges that accompany the addition of PPy NPs. All materials tested in this study were cured with no surface modification or topographic alterations to allow a controlled environment to visualize only material composition impacts. The benefits of 3D printing PPy/PEGDA resin is that these parameters can be modulated to enhance cell attachment. de Vicente

and Lensen (2016) showed that surface-level topographic patterns on PEG materials induced fibroblast adhesion. Future work could include 3D printing complex structures that may have a positive impact on cell adhesion. Additionally, the conductive nature of PPy would allow electrical stimulation cells plated on the PPy/PEGDA scaffolds, which has previously been shown to increase osteoblast growth (Liu et al., 2013; He et al., 2017).

5.5 Chapter summary

This chapter has covered the biological testing of the PPy/PEGDA polymers to ensure they are capable of being used inside the human body. Cytotoxicity testing showed that PEGDA polymer cured with riboflavin containing various concentrations of PPy NPs were biocompatible over a 14 d period. Following defined ISO methods on cytotoxicity mean that these results are standardized and can have wide impacts on researchers using PEGDA and/or PPy in biomedical applications. Cell adhesion studies showed that the addition of PPy NPs did increase the cell adhesion of PEGDA, qualitatively increasing the presence of nuclei and connecting actin filaments.

List of references

Bello, A. B., Kim, D., Kim, D., Park, H. and Lee, S.-H. (2020), 'Engineering and functionalization of gelatin biomaterials: From cell culture to medical applications', *Tissue Engineering Part B: Reviews* **26**(2), 164–180. PMID: 31910095.

Carles-Carner, M., Saleh, L. S. and Bryant, S. J. (2018), 'The effects of hydroxyapatite nanoparticles embedded in a MMP-sensitive photoclickable PEG hydrogel on encapsulated MC3T3-E1 pre-osteoblasts', *Biomedical Materials* **13**(4), 045009.

Chaves Neto, A. H., Yano, C. L., Paredes-Gamero, E. J., Machado, D., Justo, G. Z., Peppelenbosch, M. P. and Ferreira, C. V. (2010), 'Riboflavin and photoproducts in mc3t3-e1 differentiation', *Toxicology in Vitro* **24**(7), 1911–1919.

de Vicente, G. and Lensen, M. C. (2016), 'Topographically and elastically micropatterned peg-based hydrogels to control cell adhesion and migration', *European Polymer Journal* **78**, 290–301.

Dee, K. C., Puleo, D. A. and Bizios, R. (2002), *Biomaterials*, John Wiley and Sons, Ltd, chapter 1, pp. 1–13.

Gaharwar, A. K., Rivera, C., Wu, C.-J., Chan, B. K. and Schmidt, G. (2013), 'Photocrosslinked nanocomposite hydrogels from peg and silica nanospheres: Structural, mechanical and cell adhesion characteristics', *Materials Science and Engineering: C* **33**(3), 1800–1807.

He, Y., Wang, S., Mu, J., Dai, L., Zhang, Z., Sun, Y., Shi, W. and Ge, D. (2017), 'Synthesis of polypyrrole nanowires with positive effect on MC3T3-E1 cell functions through electrical stimulation', *Materials Science and Engineering: C* **71**, 43–50.

International Organization for Standardization (2012), 'Iso 10993-12:2012'.

Jie, W., Song, F., Li, X., Li, W., Wang, R., Jiang, Y., Zhao, L., Fan, Z., Wang, J. and Liu, B. (2017), 'Enhancing the proliferation of MC3t3-e1 cells on casein phosphopeptide-biofunctionalized 3d reduced-graphene oxide/polypyrrole scaffolds', *RSC Advances* **7**(55), 34415–34424.

Kim, M. K. M., Burns, M. J., Serjeant, M. E. and Séguin, C. A. (2020), 'The mechano-response of murine annulus fibrosus cells to cyclic tensile strain is frequency dependent', *JOR SPINE* **3**(4), e21114.

Lee, R. J., Abbasalipour, M., Khosravi, M. A., Zeinali, S., Khanahmad, H., Karimipoor, M. and Azadmanesh, K. (2019), 'Improvement of k562 cell line transduction by fbs mediated attachment to the cell culture plate', *BioMed Research International* **2019**, 9540702.

Li, X., Wang, Y., Wang, Z., Qi, Y., Li, L., Zhang, P., Chen, X. and Huang, Y. (2018), 'Composite PLA/PEG/nHA/Dexamethasone Scaffold Prepared by 3D Printing for Bone Regeneration', *Macromolecular Bioscience* **18**(6), 1800068.

Liu, G., Li, Y., Yang, L., Wei, Y., Wang, X., Wang, Z. and Tao, L. (2017), 'Cytotoxicity study of polyethylene glycol derivatives', *RSC Adv.* **7**, 18252–18259.

Liu, L., Li, P., Zhou, G., Wang, M., Jia, X., Liu, M., Niu, X., Song, W., Liu, H. and Fan, Y. (2013), 'Increased proliferation and differentiation of pre-osteoblasts MC3t3-e1 cells on nanostructured polypyrrole membrane under combined electrical and mechanical stimulation', *Journal of Biomedical Nanotechnology* **9**(9), 1532–1539.

Millipore-Sigma (2021), 'Riboflavin in cell culture'.

Nguyen, A. K., Gittard, S. D., Koroleva, A., Schlie, S., Gaidukeviciute, A., Chichkov, B. N. and Narayan, R. J. (2013), 'Two-photon polymerization of polyethylene glycol diacrylate scaffolds with riboflavin and triethanolamine used as a water-soluble photoinitiator', *Regenerative Medicine* **8**(6), 725–738.

Ramanaviciene, A., Kausaite, A., Tautkus, S. and Ramanavicius, A. (2007), 'Biocompatibility of polypyrrole particles: an in-vivo study in mice', *Journal of Pharmacy and Pharmacology* **59**(2), 311–315.

Sajesh, K., Jayakumar, R., Nair, S. V. and Chennazhi, K. (2013), 'Biocompatible conducting chitosan/polypyrrole–alginate composite scaffold for bone tissue engineering', *International Journal of Biological Macromolecules* **62**, 465–471.

Schexnailder, P. J., Gaharwar, A. K., Bartlett II, R. L., Seal, B. L. and Schmidt, G. (2010), 'Tuning cell adhesion by incorporation of charged silicate nanoparticles as cross-linkers to polyethylene oxide', *Macromolecular Bioscience* **10**(12), 1416–1423.

Scudiero, D. A., Shoemaker, R. H., Paull, K. D., Monks, A., Tierney, S., Nofziger, T. H., Currens, M. J., Seniff, D. and Boyd, M. R. (1988), 'Evaluation of a soluble tetrazolium/formazan assay for cell growth and drug sensitivity in culture using human and other tumor cell lines.', *Cancer Res* **48**(17), 4827–4833.

Thermo-Fisher (2021), 'Mem alpha culture media (12571)'.

Unagolla, J. M. and Jayasuriya, A. C. (2020), 'Hydrogel-based 3d bioprinting: A comprehensive review on cell-laden hydrogels, bioink formulations, and future perspectives', *Applied Materials Today* **18**, 100479.

Zhu, J. (2010), 'Bioactive modification of poly(ethylene glycol) hydrogels for tissue engineering', *Biomaterials* **31**(17), 4639–4656.

Chapter 6

Concluding remarks

6.1 Summary of conclusions

This thesis has explored the creation and application of a composite PPy/PEGDA biomaterial for osteogenic applications. The findings ascertained through these studies have prompted the following conclusions:

1. PPy NPs can be successfully incorporated into photoactive PEGDA resins that are capable of being cured using riboflavin as a natural photoinitiator. This process entailed a two-step creation methodology of the composite resin, first the PPy NPs were formed using oxidative polymerization and added to the PEGDA resin. A novel PEGDA, TEA and riboflavin resin was developed to compliment the PPy NPs that avoided the use of potentially cytotoxic curing methods. The successful PPy/PEGDA composite polymer showed comparable conductivity to bone tissue along with novel findings into the impact of PPy on the hydrogel swelling ratio.

2. PPy/PEGDA resin was shown to be a successful stereolithography printing resin for the creation of complex microarchitectures. The impact of PPy NPs on hydrogel print resolution was investigated and showed that the NPs benefitted feature resolution by reducing over-cure. Resins were able to achieve features smaller

in diameter than required for optimal osteogenic activity in bone scaffolds. Additionally, the resins were able to mimic complex osteogenic morphology for the creation of patient customized bone grafts.

3. PPy NPs are capable of pH-dependent drug delivery that can be modulated to suit a wide variety of applications when used *in-vivo*. Modelling of dopant release using FL showed the pH dependent release over a biologically relevant pH range. Additionally, a novel entrapment method for vancomycin was deemed successful that has applications for the delivery of various pH-sensitive molecules. The PEGDA encapsulation of PPy NPs allowed for a controlled release of vancomycin that has increased clinical significance as opposed to burst dopant release.

4. Finally, the biological testing of the PPy/PEGDA polymers showed no cytotoxicity and improved cell-adhesion with the incorporation of PPy NPs. MC3T3-E1 cells integrated onto the polymer surface and showed the potential of this material to be used as a cell scaffold for improved bone regeneration.

6.2 Summary of contributions

The most significant research contributions presented in this thesis are summarized as follows:

- The first-ever study on the creation of a photoactive PPy/PEGDA resin utilizing riboflavin as a photoinitiator that is capable of being cured using UV light. Development highlighted the NP creation methods combined into a hydrogel format to develop a composite biomaterial. Characterization of the impact of PPy NPs on the hydrogel allowed the functional properties of the composite material to be understood.

- A novel study into the 3D printing characteristics of PPy/PEGDA riboflavin resin

using stereolithography techniques. The resin formulations allowed the creation of complex, high-resolution 3D structures that are capable of mimicking bone microarchitecture.

- The first study on the pH-dependent drug delivery from PPy NPs over a biologically relevant pH range for *in-vivo* applications. Testing included FL and vancomycin release at various time points that help elucidate the pH drug delivery mechanism and apparent efficiency with a focus on biologic applications. Integration of PPy NPs into hydrogels allowed for an increasingly controlled release mechanism.

- A new perspective on the biocompatibility and cell adhesion impact of PPy NPs when incorporated into PEGDA hydrogels. A full wash and sterilization procedure for hydrogels was created to complement this study. The results showed integration of pre-osteoblast cells on the scaffold surface with exposed PPy NPs that support its use as a cell scaffold for osteogenic applications.

6.3 Recommendations for future research

The hydrogel analysis in this thesis provided valuable information into the formation of UV-crosslinked PEGDA hydrogels and the impact that PPy NPs have on this phenomenon. As described in Chapter 3, increased testing is need to understand the impact of PPy on the swelling ratio, as it is was seen to decrease with NP addition. Wettability and contact angle tests of composite material would help understand these interactions. Additionally, further tuning of the hydrogel matrix properties would allow efficient drug delivery of specific molecules and add a second drug release control parameter, outside of pH.

The 3D printing parameters of this thesis serve as a base for future studies. Further tuning of the depth of cure, layer height, layer cure time and settling time could all lead to the definition of smaller features than were reported in this thesis. The capabilities of

3D printing can also be extended to the drug delivery and biological testing sections. Specifically, the creation of complex scaffold that increase diffusion rates or surface area ratios would heavily impact the drug release rates and could be modified based on the desired application. For biological testing, only flat polymers were studied to exclude any confounding effects of 3D morphology that could affect the cell adhesion data collected. The printing of complex microstructures could help further improve the cell adhesion of these materials.

To advance the biological testing of these materials, future studies could look at quantification of the cell adhesion data to solidify the relationship outlined in this thesis. Additionally, testing of the cell gene expression after being seeded onto the polymer would be useful. This could help elucidate the complex cell interactions that are occurring between the biomaterial and the cell signalling pathway. Future *in-vivo* testing could include mouse models that simulate large skeletal defects, measuring the bone ingrowth and calcification with these PPy/PEGDA scaffolds.

Appendices

Appendix A

Supplemental Cell Imaging Data

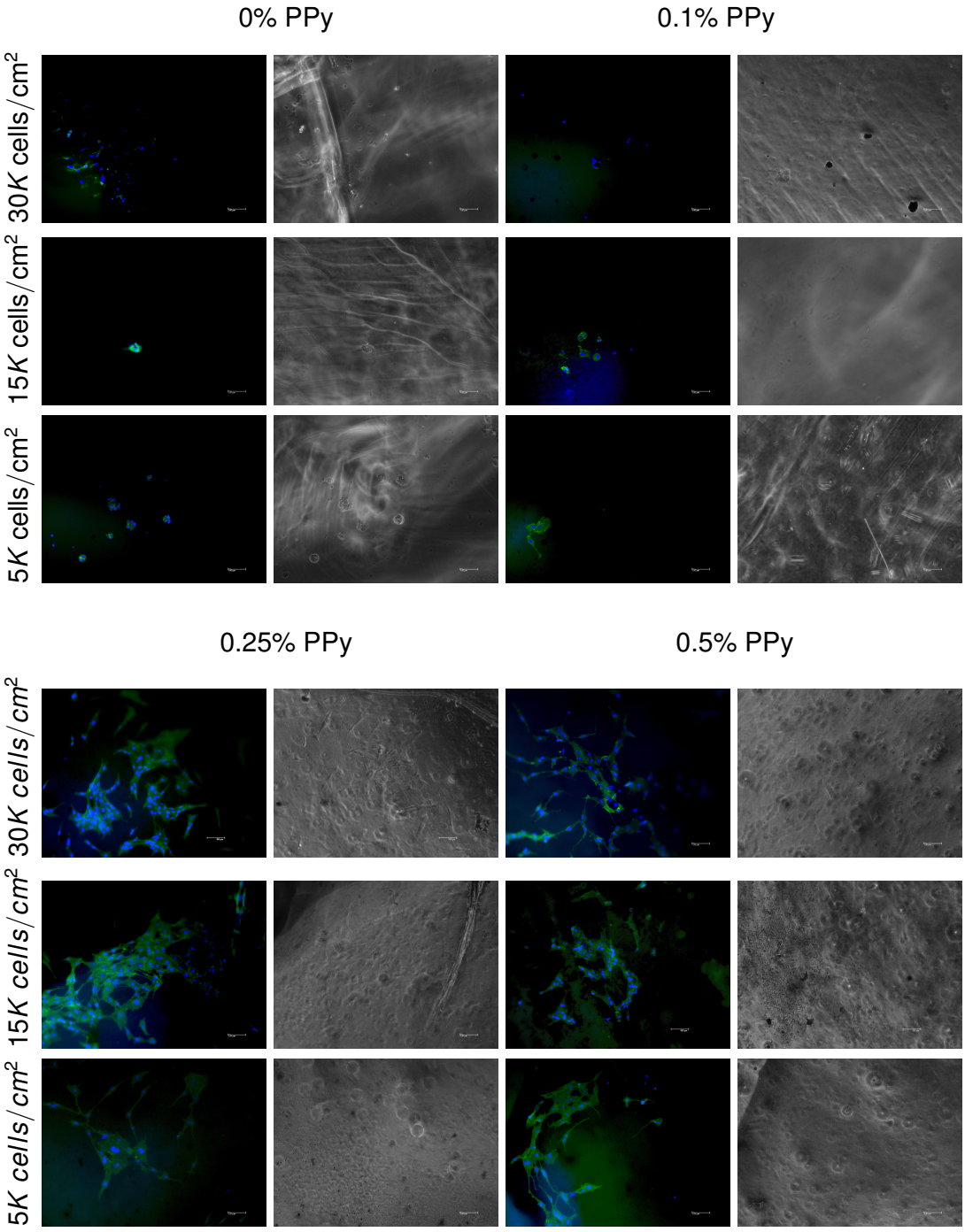

Figure A.1: Hoechst and phalloidin stained cells images for 0, 0.1, 0.25 & 0.5 % PPy polymers, plated at three cell densities: 5,000, 15,000 & 30,000 cells/cm^2 along with the phase contrast images to allow insight into the polymer surface that facilitates cell adhesion.

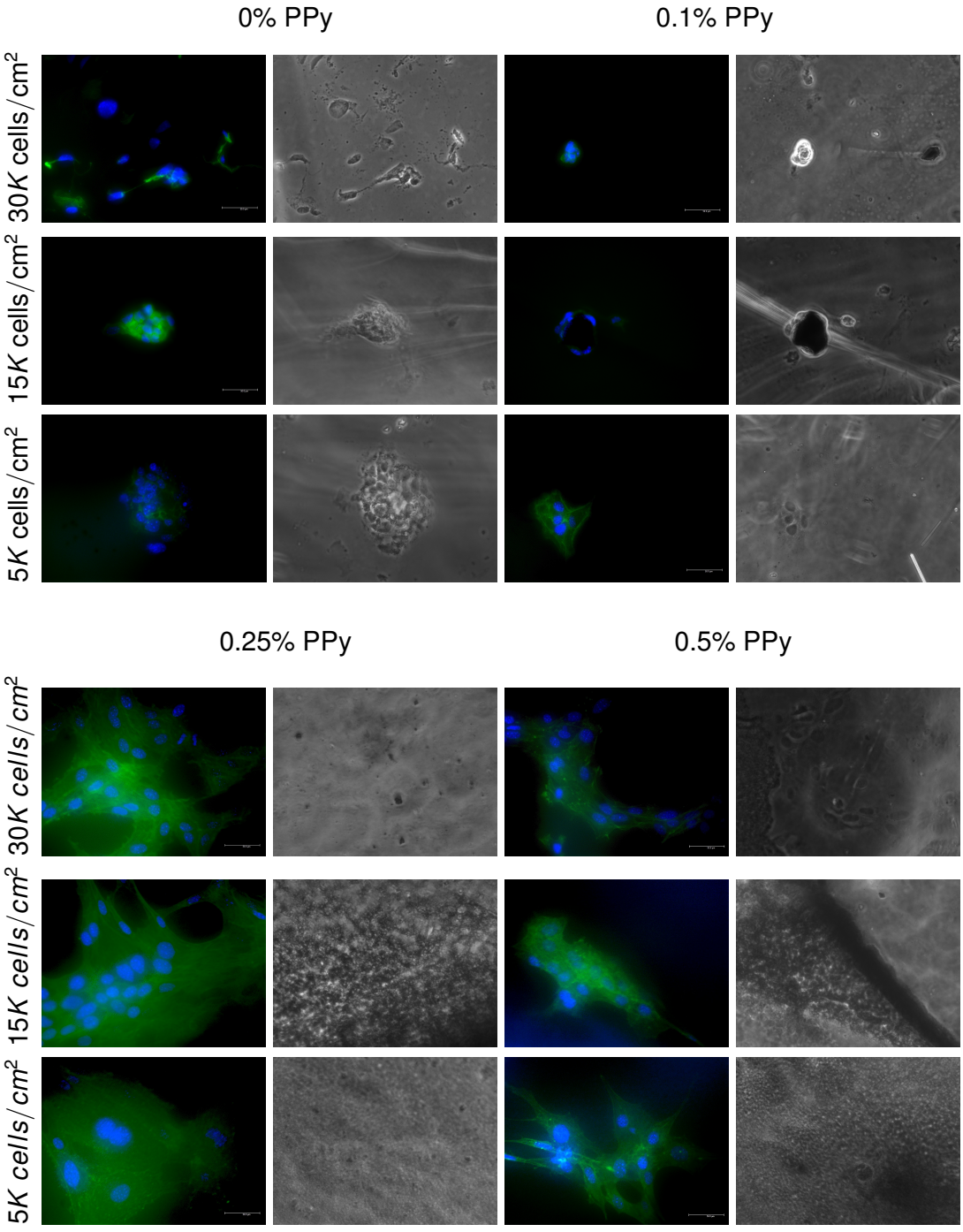

Figure A.2: Hoechst and phalloidin stained cells for 0.1, 0.25 & 0.5 % PPy polymers, plated at three cell densities: 5,000, 15,000 & 30,000 cells/cm^2. The cell spreading was qualitatively increased with the addition of PPy NPs, visualized by the actin fibre extension between nuclei.

Appendix B

Copyright Permissions

The following pages provide confirmation of acquired copyright permissions for the appropriate referenced figures in this thesis. Table B.1 summarizes the copyright information, followed by excerpts of the relevant documentation. Permissions are presented in the order they appear in the thesis. *Note that copyright permission marked with N/A were either given without a License Number or covered under a Creative Commons license (CCBY)*.

Table B.1: Summary of copyright permission information

Thesis Figure	Reference Title	Reference Figure	First Author	Publication	Publisher	License Number
2.1	Molecular Mechanics of Mineralized Collagen Fibrils in Bone	Figure 1	Arun K. Nair et al.	Nature Communications	Springer Nature	N/A
2.2	Mineralization and pH relationships in healing skeletal defects grafted with demineralized bone matrix	Figure 2	M. H. McGuire, B. S. Strates, J. Novak, et al.	Journal of Biomedical Materials Research Part A	John Wiley and Sons	5055891148182
2.3	Conductive Polymers: Opportunities and Challenges in Biomedical Applications	Figure 1	Toktam Nezakati, Amelia Seifalian, Aaron Tan, et al.	Chemical Reviews	American Chemical Society	N/A
2.4	Fabrication of 3D conjugated polymer structures via vat polymerization additive manufacturing	Figure 4	A. T. Cullen	Smart Materials and Structures	IOP Science	N/A
3.8	Emerging Multifunctional NIR Photothermal Therapy Systems Based on Polypyrrole Nanoparticles	Figure 1	M. Wang	Polymers	MDPI	N/A

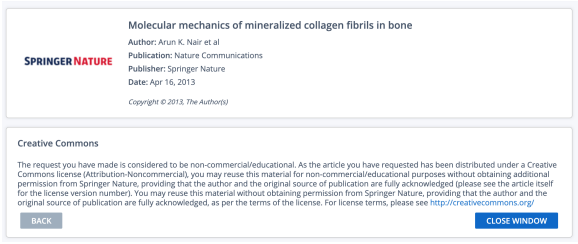

Figure B.1: Copyright permission for Figure 2.1

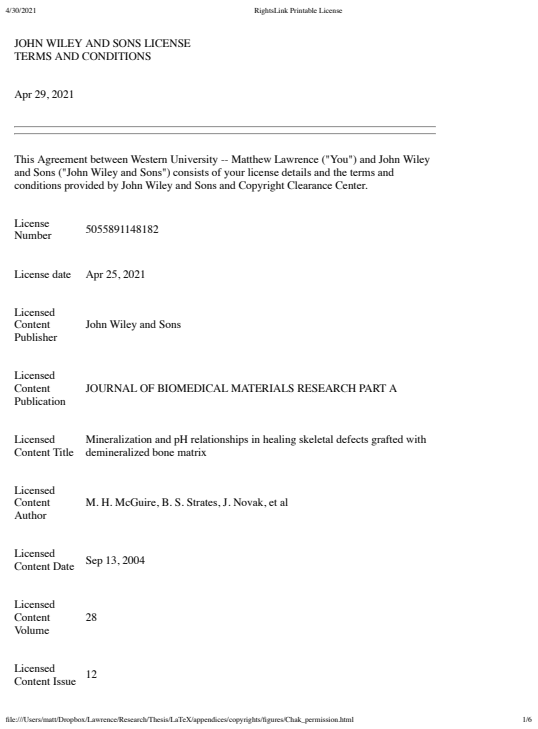

Figure B.2: Copyright permission for Figure 2.2

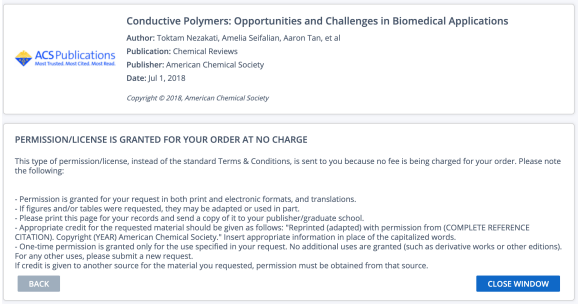

Figure B.3: Copyright permission for Figure 2.3

4/30/2021 https://marketplace.copyright.com/rs-ui-web/mp/license/7b5685b9-811a-4af1-ac81-e40c3d2cd92a/794049bf-01c5-450f-97ed-c179e8774146

Copyright Clearance Center Marketplace™

IOP Publishing, Ltd - License Terms and Conditions

This is a License Agreement between Matthew Lawrence/Western University ("You") and IOP Publishing, Ltd ("Publisher") provided by Copyright Clearance Center ("CCC"). The license consists of your order details, the terms and conditions provided by IOP Publishing, Ltd, and the CCC terms and conditions.

All payments must be made in full to CCC.

Order Date	29-Apr-2021	**Type of Use**	Republish in a thesis/dissertation
Order license ID	1115630-1		
ISSN	0964-1726	**Publisher**	IOP Publishing
		Portion	Image/photo/illustration

LICENSED CONTENT

Publication Title	Smart Materials and Structures	**Country**	United Kingdom of Great Britain and Northern Ireland
Author/Editor	Institute of Physics (Great Britain), Society of Photo-optical Instrumentation Engineers.	**Rightsholder**	IOP Publishing, Ltd
		Publication Type	Journal
Date	01/01/1992		
Language	English		

REQUEST DETAILS

Portion Type	Image/photo/illustration	**Distribution**	Worldwide
Number of images / photos / illustrations	1	**Translation**	Original language of publication
Format (select all that apply)	Electronic	**Copies for the disabled?**	No
		Minor editing privileges?	No
Who will republish the content?	Academic institution	**Incidental promotional use?**	No
Duration of Use	Life of current edition	**Currency**	CAD
Lifetime Unit Quantity	Up to 499		
Rights Requested	Main product		

NEW WORK DETAILS

Title	3D Printed Polypyrrole Scaffolds for pH Dependent Drug Delivery with Applications in Bone Regeneration	**Institution name**	Western University
		Expected presentation date	2021-05-03
Instructor name	Matthew Lawrence		

ADDITIONAL DETAILS

https://marketplace.copyright.com/rs-ui-web/mp/license/7b5685b9-811a-4af1-ac81-e40c3d2cd92a/794049bf-01c5-450f-97ed-c179e8774146 1/5

Figure B.4: Copyright permission for Figure 2.4

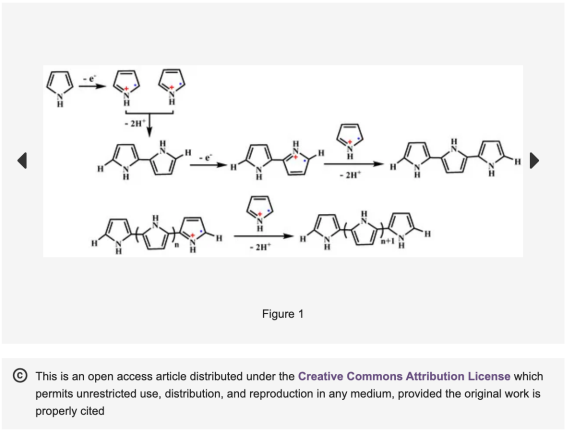

Figure 1

Figure B.5: Copyright permission for Figure 3.8

Curriculum Vitæ

Name:	Matthew T Lawrence
Post-Secondary Education and Degrees:	The University of Western Ontario London, Ontario, Canada 2014 – 2019 B.E.Sc.
Honours and Awards:	Ontario Graduate Scholarship 2019 – 2020 2020 – 2021 (declined) NSERC Canadian Graduate Scholarship - Masters Program 2020 – 2021 Western's Collaborative Training Program in MSK Health Research Transdisciplinary Training Award 2019 – 2021 Canadian Bone and Joint Conference Top Poster Presenter in Basic Biological and Biomedical Science Award 2020
Related Work Experience:	Teaching Assistant The University of Western Ontario MME 9624: Actuator Principles, Integration and Control 2019 MSE 3302: Sensors and Actuators 2020 MSE 3301: Materials Selection 2020 MSE 2202: Introduction to Mechatronic Design 2021 MSE 3380: Mechanical Components Design for Mechatronic Systems 2021

Publications:

Liubchak, I., Lawrence, M. T., Holness, F. B. and Price, A. D. (2020), 'Soft template electropolymerization of polypyrrole for improved ph-induced drug delivery', *International Journal of Molecular Sciences* **21**(21).